FINAL REPORT

07122-43.FINAL

Optimization of Infill Well Locations in Wamsutter Field

#07122-43

August 24, 2011

Mohan Kelkar, Ph.D.
Principal Investigator
The University of Tulsa
800 South Tucker Drive
Tulsa, OK 74104

LEGAL NOTICE

This report was prepared by The University of Tulsa as an account of work sponsored by the Research Partnership to Secure Energy for America, RPSEA. Neither RPSEA members of RPSEA, the National Energy Technology Laboratory, the U.S. Department of Energy, nor any person acting on behalf of any of the entities:

a. MAKES ANY WARRANTY OR REPRESENTATION, EXPRESS OR IMPLIED WITH RESPECT TO ACCURACY, COMPLETENESS, OR USEFULNESS OF THE INFORMATION CONTAINED IN THIS DOCUMENT, OR THAT THE USE OF ANY INFORMATION, APPARATUS, METHOD, OR PROCESS DISCLOSED IN THIS DOCUMENT MAY NOT INFRINGE PRIVATELY OWNED RIGHTS, OR

b. ASSUMES ANY LIABILITY WITH RESPECT TO THE USE OF, OR FOR ANY AND ALL DAMAGES RESULTING FROM THE USE OF, ANY INFORMATION, APPARATUS, METHOD, OR PROCESS DISCLOSED IN THIS DOCUMENT.

THIS IS A FINAL REPORT. THE DATA, CALCULATIONS, INFORMATION, CONCLUSIONS, AND/OR RECOMMENDATIONS REPORTED HEREIN ARE THE PROPERTY OF THE U.S. DEPARTMENT OF ENERGY.

ABSTRACT

One of the most important challenges operators of tight gas reservoirs face is optimizing infill well locations. Unlike conventional reservoirs, optimization of infill well locations in tight gas reservoirs is significantly difficult for the following reasons:

- The tight gas reservoirs show significant variation in reservoir properties and lack of spatial continuity. It is difficult to determine the contributions from a new well due to acceleration of production and incremental addition due to connection of new drainage volumes.
- The sands present in the reservoir, on a gross basis, tend to be quite thick. During the upscaling of fine-scale models for simulation purposes, the sands will create an appearance of connectivity which does not exist in the fine-scale model.
- The distinction between static and dynamic connectivities needs to be recognized. Sands which appear continuous may not help production due to very low permeability and convoluted flow patterns resulting in lack of dynamic continuity.
- The orientation of hydraulic fractures can make a difference in optimizing well spacing.

This project addressed specific issues in the Wamsutter gas field, one of the largest gas fields in the Rocky Mountain region. Although we concentrated on this particular field, the results can be applied to other tight sand gas fields.

We have used a three-prong approach to address the issues noted above:

- Knowing that reservoir simulation studies are not always possible, we devised a methodology for predicting the future performance of the wells using production data only. Our newly developed methodology can predict both incremental and acceleration potentials from a newly drilled well.
- We used conventional simulation results to predict the infill well potential after generating a geologically consistent reservoir description followed by history matching of prior performance.
- We used streamline simulation to determine dynamically connected volume so that infill wells can be located based on un-depleted reservoir volume.

The project involved The University of Tulsa (Offeror), Texas A & M University, and Devon Energy Corporation. The principal investigator was Dr. Mohan Kelkar of The University of Tulsa. Dr. Akhil Datta-Gupta led the effort at Texas A & M University. Devon Energy was involved in all phases of the project, including the drilling of seven new wells, based on the recommendations of this study.

This report is divided into multiple sections. In the first section, we provide the background of the Wamsutter field, the area of concentration, and the data collected. Next, we provide the methodology used in determining the acceleration versus incremental EUR based on the production data only. Then we discuss the approach used in developing a geological model, conducting history match, and prediction of future performance of the wells. Next, we cover streamline simulation and its use in locating the un-drained portion of the reservoir. Lastly, we provide some conclusions and additional recommendations.

SIGNATURE PAGE

Dated this _____ day of _____, 2011

Submitted by: Mohan Kelkar, Ph.D.
Principal Investigator
The University of Tulsa
800 South Tucker Drive
Keplinger Hall #L117
Tulsa, OK 74104 USA
(918) 631-3036 – Phone
(918) 631-3250 – Fax

Signature: Mohan Kelkar

THIS PAGE INTENTIONALLY LEFT BLANK

TABLE OF CONTENTS

Page

BACKGROUND **1**
PRODUCTION DATA ANALYSIS **8**
Literature Review **10**
Approach **11**
Results and Discussion **15**
SIMULATION PERFORMANCE PREDICTION 23
Geological Model **23**
Structural Modeling *23*
Property Modeling *31*
Scaled-Up Well Logs 31
Spatial Continuity 32
Facies Modeling 36
Petrophysical Modeling 36
Simulation Model **38**
Upgridding and Upscaling *38*
Local Grid Refinement *40*
Evaluation of Production Data to Determine Fracture Properties *41*
Dynamic Properties *42*
History Matching *47*
POST MATCHING ANALYSIS AND PREDICTIONS **58**
Post-Script 67
STREAMLINE SIMULATION **69**
Introduction 70
Approach 71
Application 78
Field Section Example *78*
Wamsutter Application *82*
Quality Map for Well Placement *84*
CONCLUSIONS **86**
REFERENCES **88**

APPENDIX A – PROGRAM MANUAL **90**
Purpose of Program 90
Collection of Data 90
Program Structure 90
Overview *90*
"Basic_Data" Sheet *90*
"Production_Data" Sheet *91*
"Section" Sheet *93*
"Group" Sheet *95*
"Calculation" Sheet *99*

Optimization of Infill Well Locations in Wamsutter Field

BACKGROUND

Wamsutter field is located in southwest Wyoming. It is a part of the Great Green River Basin and has been developed since the 1950's. The reservoir is the Almond formation in upper Cretaceous interval with permeabilities less than 0.1 md. It is bounded by Lewis shale at the top and Ericson sand at the bottom. All wells are stimulated with hydraulic fractures. Figure 1 shows the relative location of the Wamsutter field.

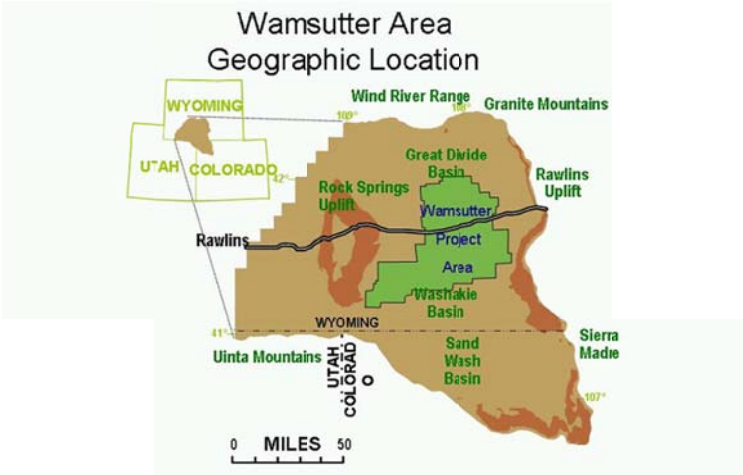

Figure 1: Wamsutter Area Geographic Location

Figure 2 represents the depositional environment of the Mesa Verde Group, of which the Almond formation is a part. There are mountains to the west on the left and a shallow Cretaceous seaway to the east on the right of the block model. Channel sands prograded in from the west and shoreface bar sands were deposited from the north by longshore currents. The area was an embayment on the western edge of the shallow Late Cretaceous seaway about 74 million years ago.

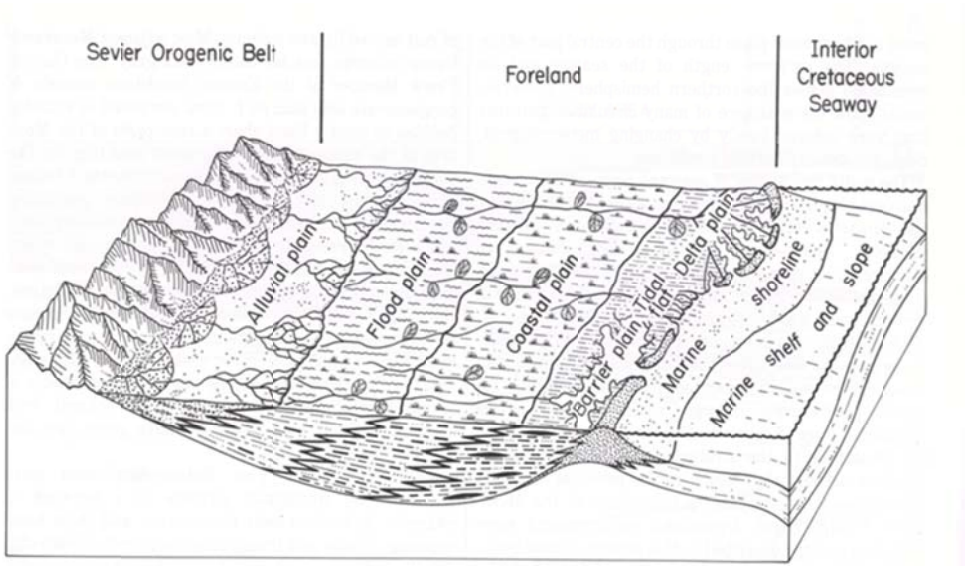

Figure 2: Mesa Verde Depositional Model

The Almond formation is divided into three zones: Upper Almond, Middle Almond and Lower Almond. There is also a sand bar at the top of the Upper Almond zone, which is called the Almond Bar. In this work, the Almond Bar was isolated as a distinctive zone in the model. Figure 2 is a picture of the depositional environment and can be related to the Almond formation with the flood plain to be the Lower Almond, coastal plain to be the Middle Almond and delta plain with barrier plain to be the Upper Almond and the Almond Bar.

Figure 3 is a cross-section of the Almond formation with Effective Porosity (PHIE) and Shale Volume (VSHGR) logs. All four zones are displayed and separated by lines. The Upper Almond zone has the highest thickness, and the thinner zones are the Lower Almond, Middle Almond and the Almond Bar.

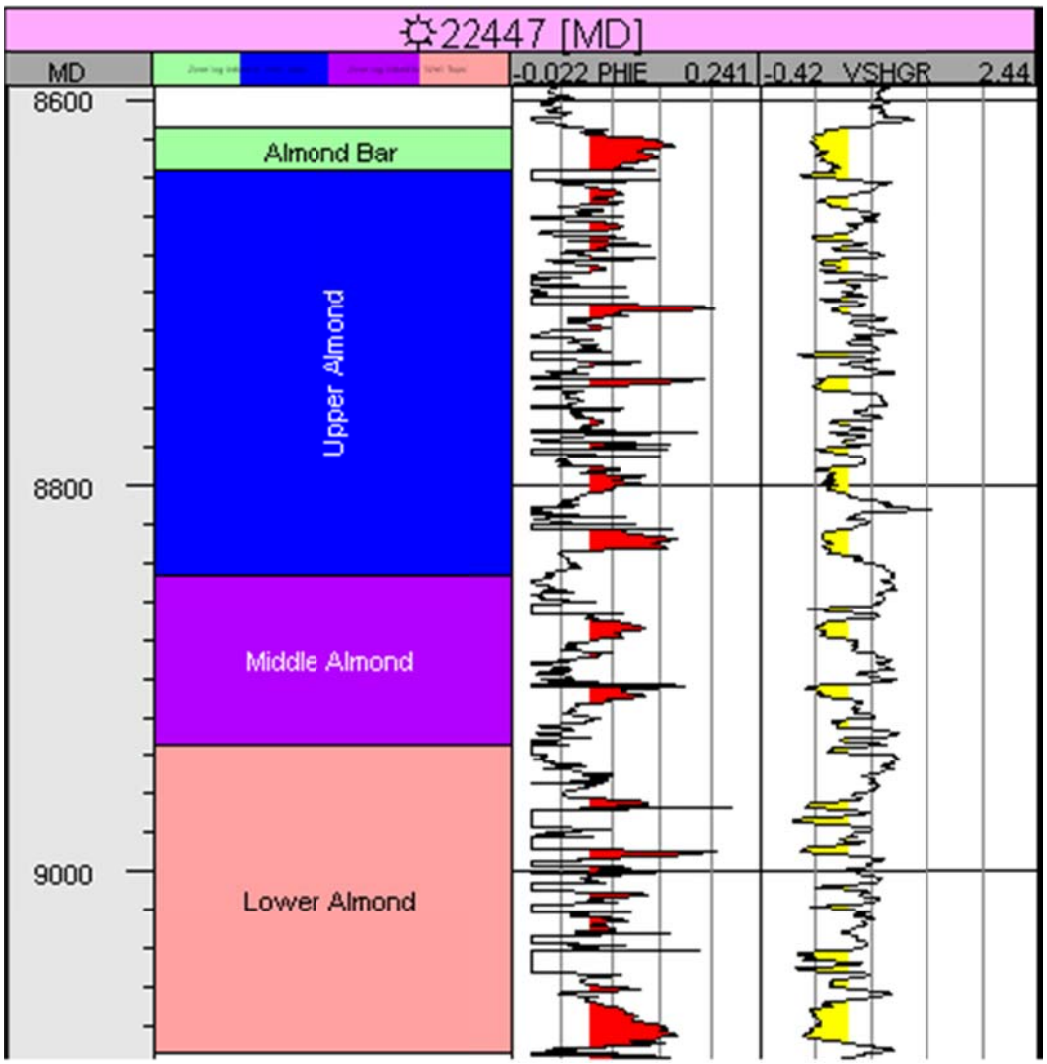

Figure 3: Almond Cross Section with Porosity and V_{sh} Logs

Devon geologists suggest that the Almond Bar is the most continuous formation.[1] Production history indicates that wells where the Almond Bar is present usually have a higher expected ultimate recovery (EUR), than those without it. There is also a theory that the Almond Bar acts as a transit route for the gas that escapes from lower sands, because its permeability goes up to 2 md.

Currently the field is being developed on an 80-acre spacing. The development is not yet finished. In the future, the operators are considering development of the field on a 40-acre spacing.

Other gas bearing formations in the study region are Lewis shale and Lance shale. Only a handful of wells are producing from these zones. Therefore, neither of these formations was used in the model we built.

We began the work by identifying an area within Wamsutter field. The following information was provided by Devon Energy: Almond structure map, well header (well API number, wellhead coordinates, kelly bushing level, total depth, directional survey), well top markers, well logs, gas properties, well completions, tubing head pressure from 2001 to 2009 and monthly production rates from 1980 to 2010. Table 1 provides the summary of available data.

Table 1: Field Data Availability

Field Data	Number of Wells
Study Area	81
Almond Producers	80
Vertical Wells	75
Directional Wells	6
Directional Survey	4
Porosity Log	77
Permeability Log	77
Pay Flag Log	78
Reservoir Flag Log	77
Water Saturation Log	77
Well Tops	75
Wellhead Pressure	47
Production Data	75

The study area was defined as 3 by 3 sections of the 16N 93W Barrel Springs Unit and an additional section in each of the four directions. Therefore, the area consisted of 5 by 5 sections: 16N 93W sections 1- 4, 9 - 16, 21 - 24, 17N 93W sections 34-36, 16N 92W sections 6, 7, 18 and 19, 17N 92W section 31. The total distance in East-West and North-South directions is 28,000 feet. Figure 4 shows the area of interest.

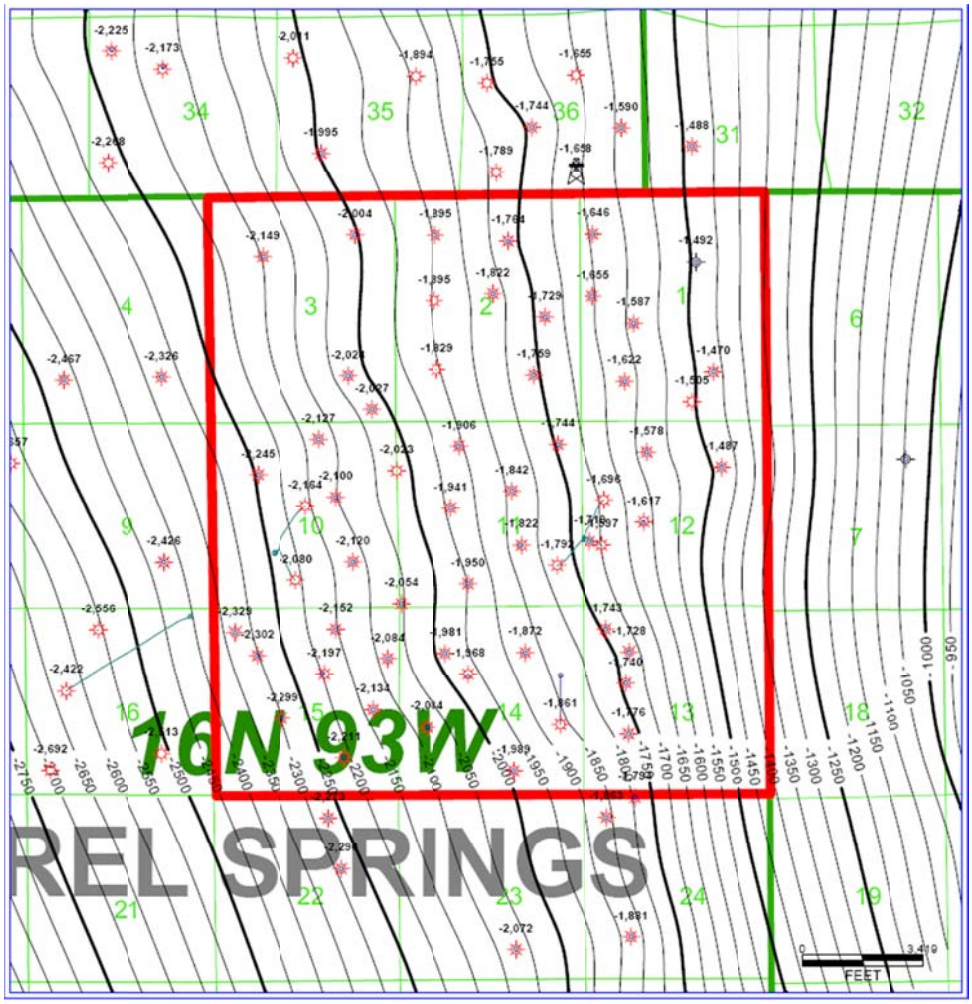

Figure 4: Almond Structure Map of 5-by-5 Sections Study Area

The boundary encloses 81 wells; 75 vertical and 6 deviated. Production data showed that four wells started producing from the Lance formation later in their lives. One well was producing from the Lance formation since the completion; this well was not used in our analysis.

Different operators in the field used different names for their wells. For convenience we truncated the well number based on the API number. It was done by truncating the first 5 and the last 2 numbers, and the well name became a 5 digit number. For example, well 490072032500 became 20325. The second number in the new name indicated the decade the well was drilled with number 0 standing for the 1980s and before, 1 for the 1990s and 2 for 2000s. The exception is well 21738, which was drilled in 1982.

Nineteen well tops were provided as shale markers of the flooding surfaces. A flooding surface is a surface separating young strata (above) from the older strata (below), across which there is evidence of an abrupt increase in water depth across the surface. Almond MFS is the same as Almond Middle, where MFS stands for maximum flooding surface. LMA Coal 3 is the same as LMA Coal 1 and Almond Lower, where LMA stands for lower marine Almond. The data available describing the tops is summarized in Table 2.

Table 2: Number of Wells for Each Well Top

Horizon	# Tops
Almond	80
Almond_Bar_Baldy_Butte_Top	63
Almond_Bar_Baldy_Butte_Base	62
Almond_FS_90	67
Almond_FS_85	65
Almond_FS_80	81
Almond_FS_70	81
Almond_FS_65	25
Almond_FS_60	81
Almond_Middle	69
Almond_MFS	82
Almond_FS_50	81
Almond_FS_40	80
Almond_FS_35	6
Almond_FS_30	2
Almond_Lower	26
LMA_Coal_1	51
LMA_Coal_3	50
Ericson	33

The following logs were provided: reservoir flag, pay flag, effective porosity, permeability, coal flag and water saturation. These logs were already processed by Devon Energy petrophysicists,[2] so we did not perform any additional calculations. The reservoir flag log was a flag curve indicating reservoir rock. Required cutoffs were an effective porosity greater than 6% and a shale volume percentage (V_{sh}) less than 50%. The pay flag log was a flag curve indicating zones of pay with a cutoff of water saturation less than 50% when the reservoir flag was present. Both flag logs had discrete values of 1 and 0. The effective porosity was the density porosity corrected for shale presence. Permeability was in-situ gas permeability. Figures 5 through 8 show the distribution of well log values.

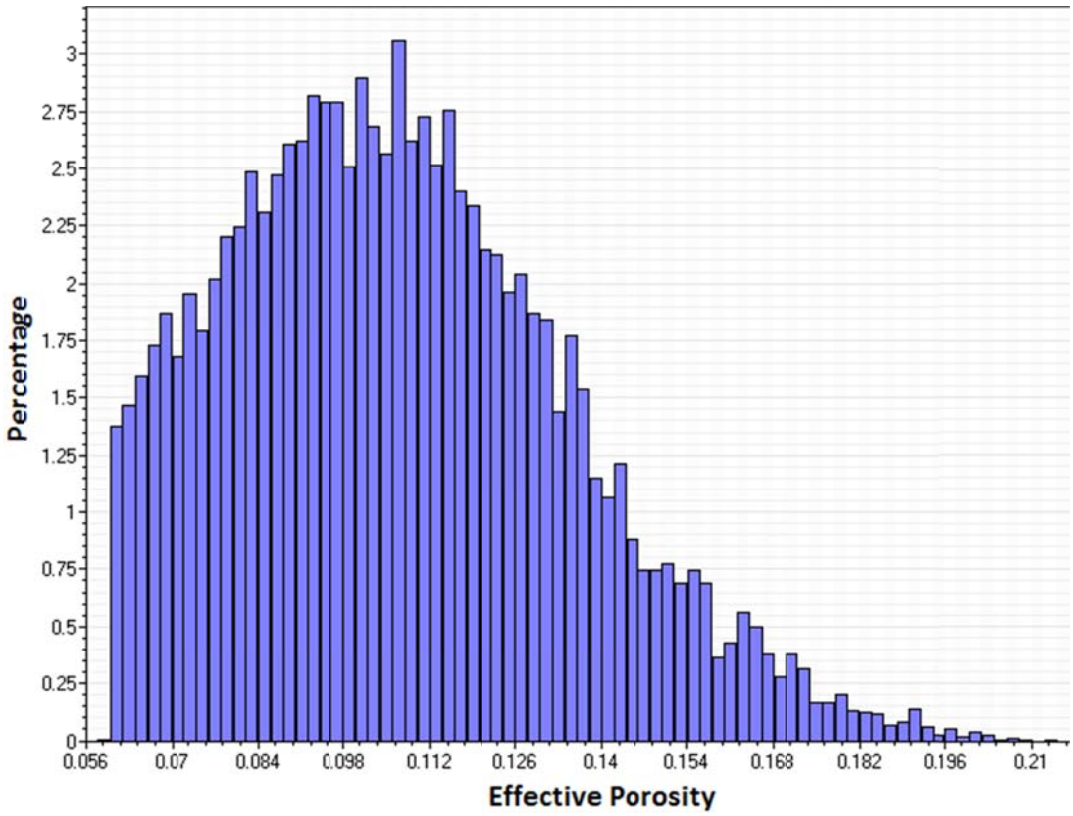

Figure 5: Effective Porosity Log Distribution in Almond Pay Sand

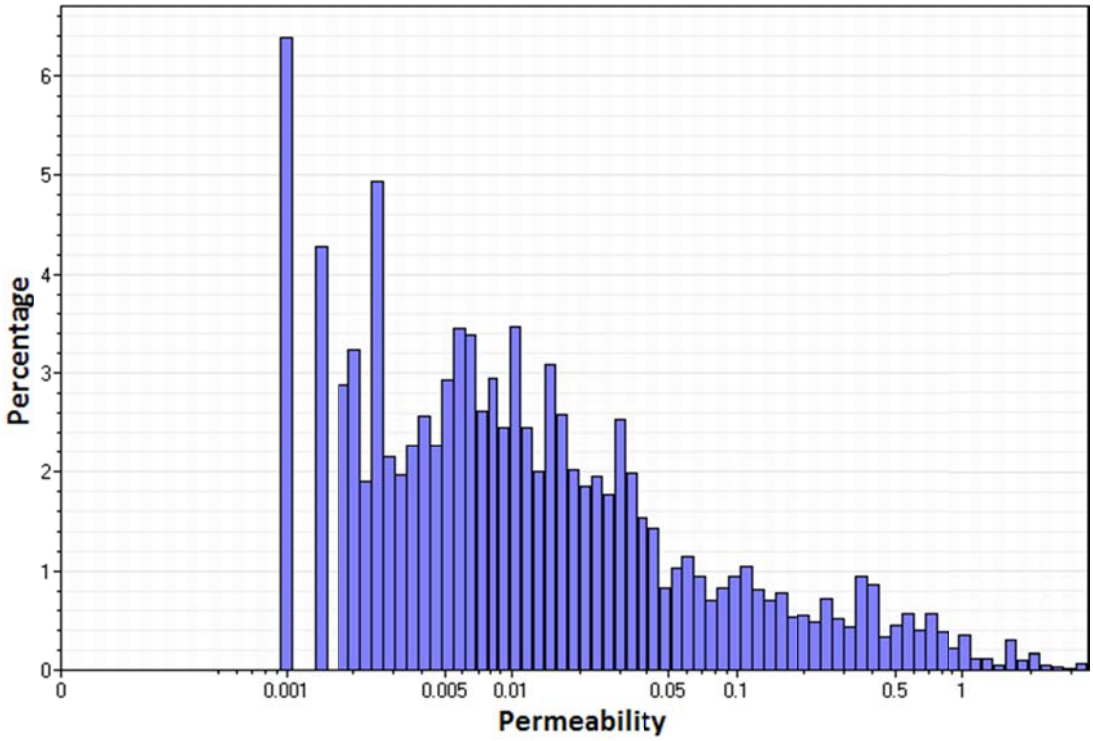

Figure 6: Permeability Log Distribution in Almond Pay Sand

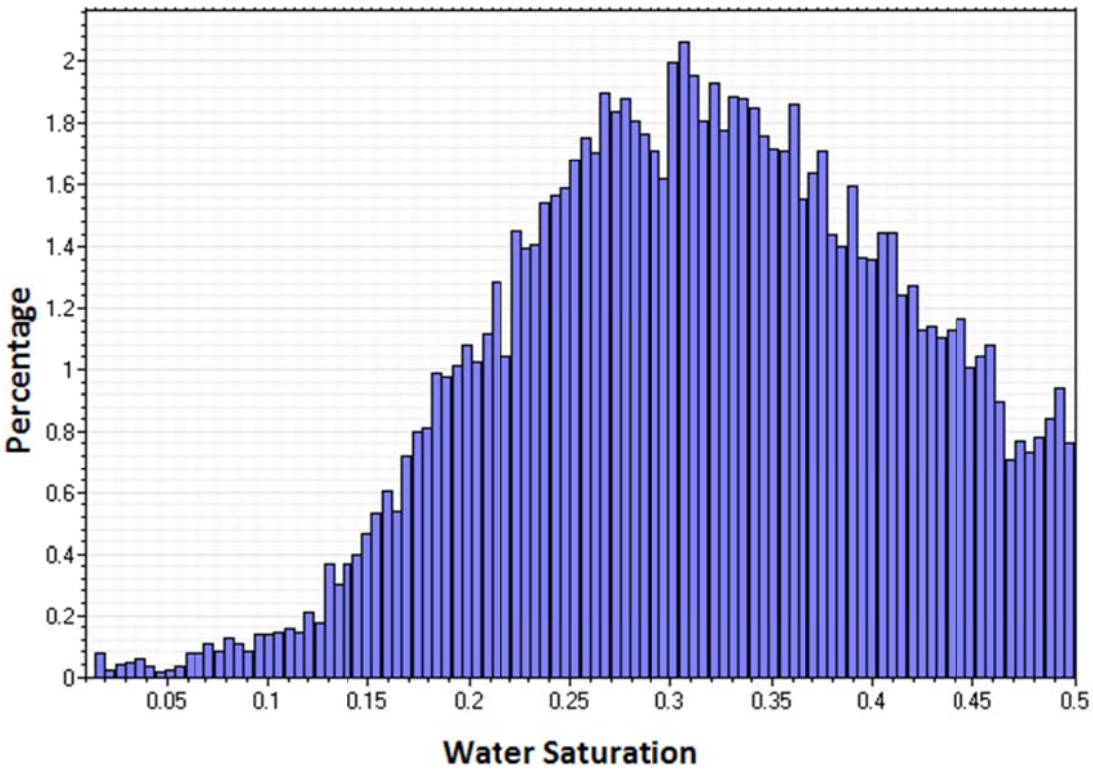

Figure 7: Water Saturation Log Distribution in Almond Pay Sand

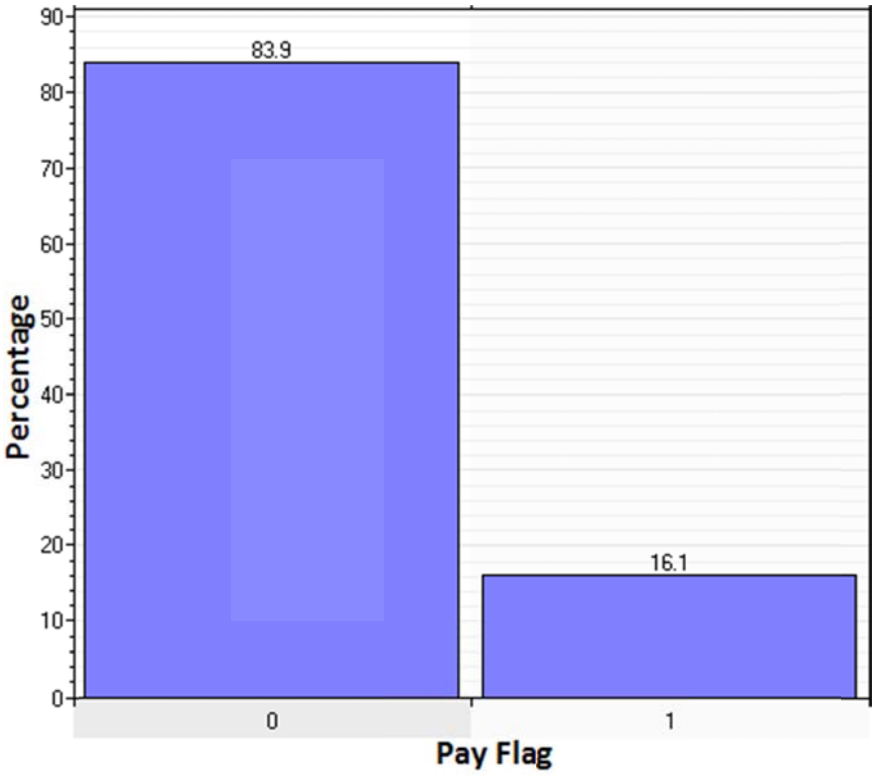

Figure 8: Pay Flag Log Distribution in Almond Pay Sand

It was assumed that the surface temperature is 60°F, geothermal gradient is 18°F per 1,000 feet, pressure gradient is 0.54 psi per foot, and gas specific gravity is 0.68. The viscosity and formation volume factor for the gas was calculated as shown in Table 3.

Table 3: Gas PVT Properties

Depth, ft	T, F	P, psi	FVF, bbl/mcf	Viscosity, cp
0	60	14.7	177.000	0.01053
500	69	270	9.379	0.01100
1000	78	540	4.554	0.01164
2000	96	1080	2.191	0.01325
3000	114	1620	1.456	0.01520
4000	132	2160	1.127	0.01726
5000	150	2700	0.954	0.01922
6000	168	3240	0.852	0.02099
7000	186	3780	0.787	0.02255
8000	204	4320	0.741	0.02394
9000	222	4860	0.708	0.02519
10000	240	5400	0.682	0.02637

Wellhead daily pressure readings at tubing and casing along with gas and water production rates were provided for forty-seven wells for the period after 2001.

Production history was given from January 1980 to April 2010 on a monthly basis. For one well, production was reported from November 1976. Only seventy-five wells from the study area were available in the database; seventy-one vertical and four deviated. Therefore, only these seventy-five wells were used in our analysis.

PRODUCTION DATA ANALYSIS

This section discusses a new methodology proposed to determine the potential from a new infill well. The main advantage of this methodology is its speed and the ability to use only production data.

Part of the reason that smaller spacing in tight gas reservoirs is justified is because of the belief that the permeability of these reservoirs is very low and the connectivity is limited. As a result, the newly drilled wells will encounter both depleted and virgin areas. The production from the depleted areas will represent the acceleration component of the well (since these reserves will be depleted by existing wells); whereas, the production from virgin areas represents the incremental component of the well (since these resources will not have been depleted except in a new well). It is reasonable to assume that as the spacing gets smaller, a higher and higher percentage of the production will come from acceleration. Geologically, thicker sands tend to be more continuous and thinner sands tend to be less continuous. As wells are drilled on a smaller spacing, it is likely that thicker sands intersected by the well will be depleted and thinner sands will be in a virgin state. As the spacing gets smaller, a smaller percentage of virgin sands will be intersected by a new well – this will result in a smaller contribution from incremental gas.

To understand the importance of acceleration versus incremental production from a new well, it is important to understand the limiting cases first. In a homogeneous reservoir, as shown in Figure 9, the

first well is drilled in the center of the reservoir and four infill wells are drilled surrounding the original well. If there are no infill wells, the production rate of the first well is shown with bold dashed curve. But we can see that after infill wells are drilled, the decline rate of the first well is much higher (solid bold line) because the other wells are taking away the gas from the original well. The amount of the declined production is diverted by those infill wells (dotted lines). Also, notice that the new wells drilled have an initial production rate similar to the current rate of the existing well. So in this case, the production of the infill wells is acceleration production. Figure 10 represents a heterogeneous reservoir. All of the wells are drilled in isolated compartments, so there is no communication between the wells. Thus, the production rate of the first well is not influenced by the infill wells. Furthermore, the similarity of the initial rate of the infill wells and the original well indicates that the infill wells have access to the new reserves and the production of the infill wells represents only incremental production. Obviously, the infill wells are most beneficial when the production from them is mostly incremental. In reality, when new wells are drilled, their actual production falls between these two extremes.

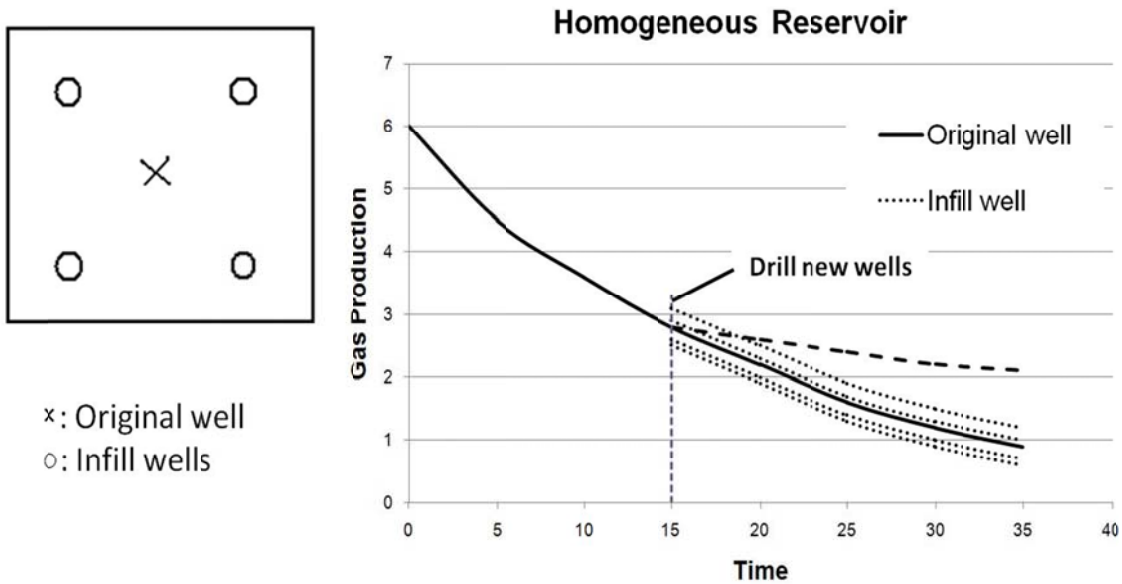

Figure 9: Homogeneous Reservoir and Production of 5 Wells

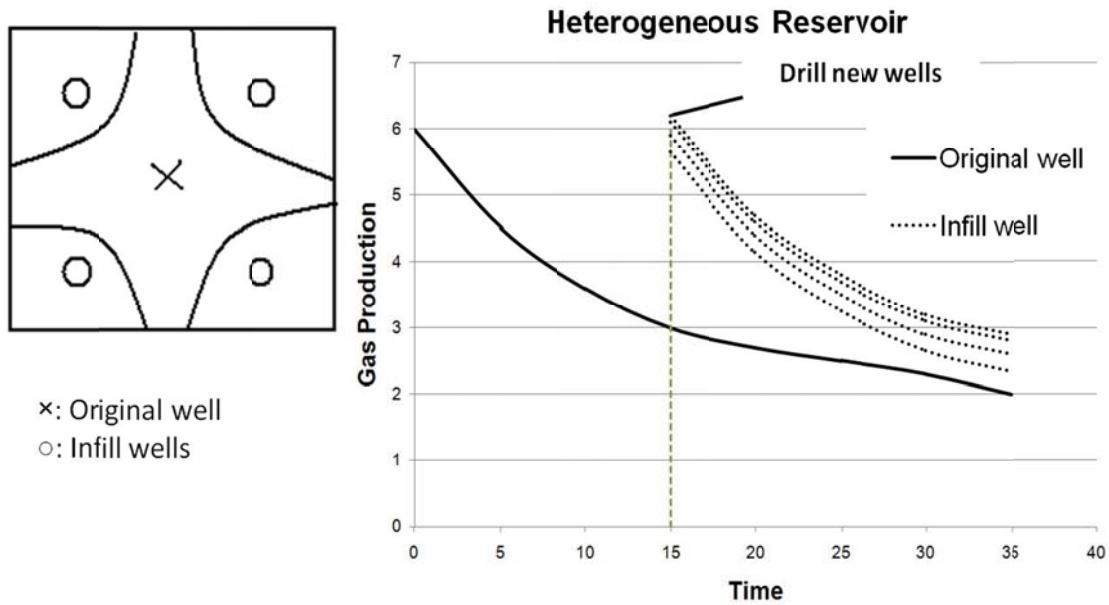

Figure 10: Heterogeneous Reservoir and Production of 5 Wells

Our goal in this section is to develop a methodology which we can determine incremental versus acceleration contributions of an infill well by using limited production data and without relying on geological or simulation modeling.

Literature Review

Several statistical techniques have been developed to evaluate the potential of infill wells.

Cipolla and Wood[3] showed the application of limited single-well reservoir modeling to predict infill-drilling potential in a tight gas reservoir. Based on a small sample set, they developed a distribution of ultimate recovery and drainage area to estimate incremental reserves. This technique was illustrated by a case history from the Ozona gas field, Crockett County, TX. The statistical drainage area and estimated ultimate recovery data were combined to estimate the potential reserve growth on 40-acre development. They identified around 1,125 infill drilling locations, adding approximately 400 Bcf of incremental reserves.

McCain, *et al.*[4] used a statistical method to evaluate the need for infill drilling in a complex, low-permeability gas reservoir. They developed a statistical production analysis method that allows the use of a small number of localized advanced evaluations, and provided areal locations where conclusions from the localized studies can be applied. This method gives accurate conclusions across the entire field without evaluating all the wells in the field. The technique evaluates the performance of each well with surrounding wells to determine if infill wells are performing similarly to or differently from old offsets. This method was used to evaluate the infill drilling potential of the Carthage (Cotton Valley) field in east Texas.

Guan, *et al.*[5] used the statistical moving window technique to evaluate the infill candidates. The research evaluated the accuracy of the moving window method which has been used in tight gas reservoirs to assess the infill well potential. This method was used to predict the infill well potential by

using simulated production data and the result was compared with reservoir simulation. For an individual well, the result of moving window infill prediction can be off more than 50%, but it can accurately predict the combined production from a group of infill candidates. Also, the accuracy of this technique increases with the number of wells in the analysis and decreases as the reservoir becomes more heterogeneous.

Gao, *et al.*[6] presented a new simulation-based inversion approach for rapid assessment of infill well potential. Instead of focusing on small-scale high-resolution problems, they worked on large-scale coarse-resolution studies. This method uses well locations, production data and approximate reservoir description to evaluate the infill potential. The accuracy of this method increases with reservoir characterization effort. This approach is demonstrated to be more accurate than the moving window statistical method.

Al-Hadrami and Teufel's[7] work took into account permeability anisotropy and reservoir heterogeneity on optimization of infill drilling in a tight gas reservoir. They conducted reservoir characterization and reservoir simulation in two pilot areas to estimate reservoir quality, permeability anisotropy, and well productivity for infill wells drilled on 80-acre spacing. They compared infill well performance with simulation results and demonstrated the value of reservoir simulation in determining effective drainage areas, optimum location, and additional recovery of infill wells.

Voneiff, *et al.*[8] used the moving domain method, which focused on the age of wells and their location and production profiles, to determine infill potential in Ozona field. The core of this approach is a moving window of local regions that draws statistical conclusions about well performance, depletion and undrained acreage. Using their method, preliminary infill estimates can be obtained, possibly in one to two weeks.

Many of the methods mentioned above use simulation as a basis and do not rely only on production data; they may be more accurate but not very practical because most operators rarely use flow simulation to determine infill potential. Further, these methods are unable to predict incremental versus acceleration potentials from infill wells as spacing is reduced. Our approach is able to predict these two contributions using only production data.

Approach

In general, our methodology is based on a simple premise: it is easier to extrapolate a linear relationship. If we use conventional decline curve analysis, it is very difficult to predict the future performance by extrapolating a curved line. On the other hand, if we develop a relationship which is linear, it is not only easier to extrapolate, but also easier to observe deviation from a straight line.

For a tight gas reservoir, production from tight sands and shale is dependent on fracturing, so understanding the performance of fractured gas wells is very important. We know that the flow across the fracture is controlled by the fracture conductivity and this determines the different flow behaviors.[9] The two most important flow patterns in tight gas reservoirs are linear flow and bilinear flow. For low conductivity fracture or early flow period, we can see bilinear flow in the fracture and the flow behavior is not affected by the tip of the fracture. As seen in Figure 11, the linear flow is observed in both fracture direction and perpendicular to fracture direction.

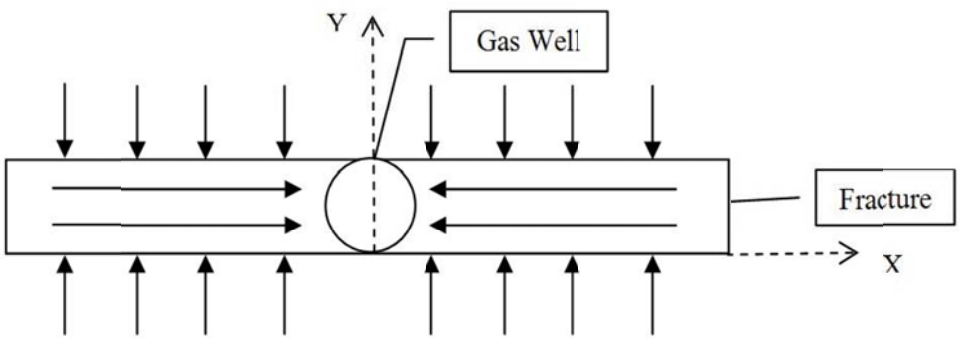

Figure 11: Bilinear Flow

For a constant pressure case, the rate in dimensionless form is[10]

$$q_D(t_D) = 0.36735\sqrt{k_{fD}b_{fD}}\,. \tag{1}$$

In field units[10]

$$q_{sc,bl} = \frac{m(p_i)-m(p_{wf})}{493.83}\frac{h}{T}\sqrt{k_f b_f}(k\varphi(\mu c_t)_i)^{0.25}t^{-0.25}\,. \tag{2}$$

Equation 2 can be simplified as

$$\frac{q_{sc,bl}}{m(p_i)-m(p_{wf})} = K_1 t^{-0.25}, \tag{3}$$

where

$$K_1 = \frac{h\sqrt{k_f b_f}(k\varphi(\mu c_t)_i)^{0.25}}{493.83T}\,. \tag{4}$$

From Equation 3, by plotting $\frac{q_{sc,bl}}{m(p_i)-m(p_{wf})}$ as function of $t^{-0.25}$, we get a straight line. It is more convenient to plot cumulative production rather than rate to minimize the rate fluctuations. Note that K_1 is constant. For Equation 2, we will integrate q to obtain the relationship between Gp and t. So we need to integrate $\frac{m(P_i)-m(p_{wf,last})}{m(p_i)-m(p_{wf})}q_{sc,bl}$ in order to get $Gp_{bl,pseudo}$ and we obtain Equation 5.

$$Gp_{bl,pseudo} = K_2 t^{0.75}, \tag{5}$$

where

$$K_2 = \frac{h\sqrt{k_f b_f}(k\varphi(\mu c_t)_i)^{0.25}(m(P_i)-m(p_{wf,last}))}{493.83T}\,. \tag{6}$$

Equation 5 indicates that plotting $Gp_{bl,pseudo}$ versus $t^{0.75}$ will yield a straight line. By extrapolating this line, we can determine the EUR as well as the remaining reserves. Also notice that $Gp_{bl,pseudo}$ is in BSCF and $p_{wf,last}$ is the last bottom hole pressure.

For higher fracture conductivity, linear flow can be observed. In Figure 12, the flow is only in the direction perpendicular to the fracture.

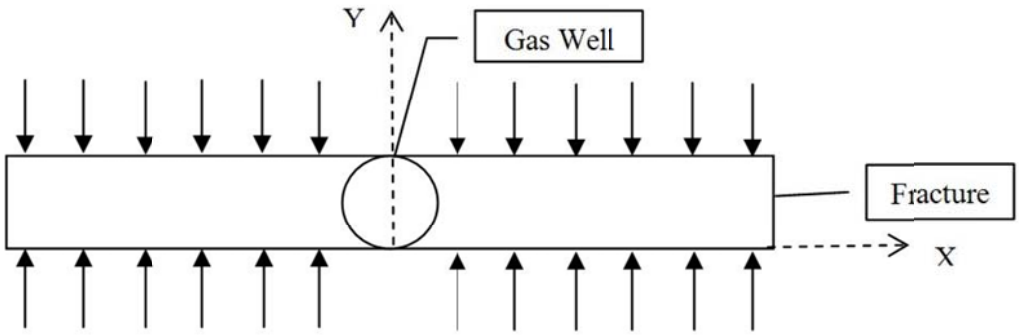

Figure 12: Linear Flow

Similarly to bilinear flow, we can get a dimensionless rate for linear flow[9],

$$q_D(t_D) = \frac{2}{\sqrt{\pi^3}}\, t_D^{-\frac{1}{2}}. \tag{7}$$

In field units,[10]

$$q_{sc,l} = \frac{m(p_i)-m(p_{wf})}{64.345}\frac{h}{T}x_f\sqrt{k_f b_f}(k\varphi(\mu c_t)_i)^{0.5}t^{-0.5}. \tag{8}$$

Multiplying both sides by $m(P_i) - m(p_{wf,last})$ and integrating, we obtain

$$Gp_{l,pseudo} = K_3 t^{0.5}, \tag{9}$$

where

$$K_3 = \frac{hx_f\sqrt{k_f b_f}(k\varphi(\mu c_t)_i)^{0.5}(m(P_i)-m(p_{wf,last}))}{64.345T}. \tag{10}$$

In Equation 9, we assume that along with rate, the bottom hole pressure varies as well. And by plotting $Gp_{l,pseudo}$ versus the square root of t, we get a straight line for linear flow.

In tight gas reservoirs, like Wamsutter, we can always observe linear or bilinear flow. So, in the analysis, it is important to observe the plot of cumulative production versus $t^{0.5}$ or $t^{0.75}$. By extrapolating the graph, we can calculate the EUR of a well and choose the plot which shows a linear relationship. It is important to explain how to determine the time until which we can extrapolate the graph. For conventional decline curve analysis, the rates are extrapolated until we reach an economic limit. If the economic limit is known, knowing the relationship between the rate and time, we can determine the corresponding time and extrapolate until we reach that time. If the economic limit is not known, we can use 30 years as a limit up to which we can extrapolate the line. It is true that 30 years is an arbitrary limit, but this limit can be justified because (i) very limited production can be collected at later times, so even if we use later times, the overall EUR will not change significantly; and (ii) the net present value of production after 30 years is practically zero, so discounting it is not going to make a significant difference in the economic analysis.

To validate our approach, we evaluated production from several tight formations. The data were collected from various websites and present typical production profile. Figures 13 and 14[11,12] present the results from various shale formations. Figures 15 and 16 present the data transformed and plotted as a

function of $t^{0.5}$. As can be seen, most data can be reasonably represented using a linear flow. Further, EURs calculated using our method match reasonably well with EURs projected by the producers.

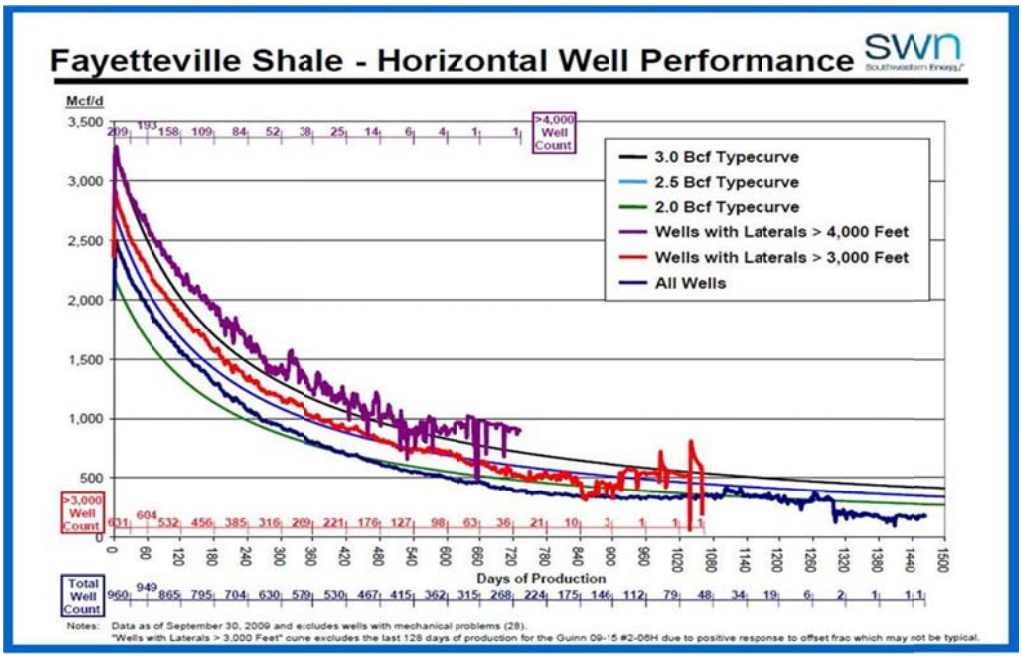

Figure 13: SWN Gas Type Curve

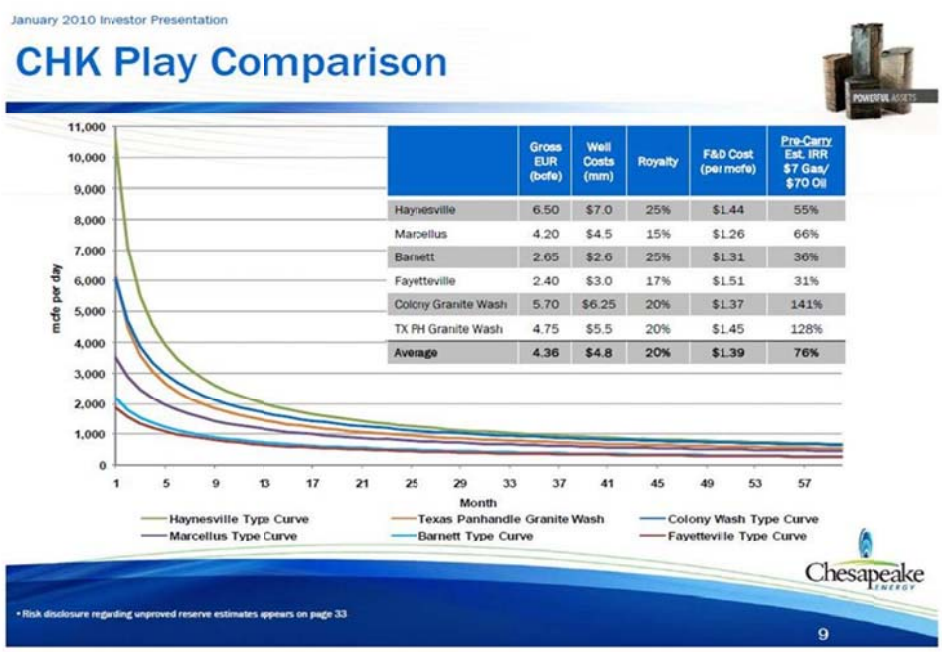

	Gross EUR (bcfe)	Well Costs (mm)	Royalty	F&D Cost (per mcfe)	Pre-Carry Est. IRR $7 Gas/ $70 Oil
Haynesville	6.50	$7.0	25%	$1.44	55%
Marcellus	4.20	$4.5	15%	$1.26	66%
Barnett	2.65	$2.6	25%	$1.31	36%
Fayetteville	2.40	$3.0	17%	$1.51	31%
Colony Granite Wash	5.70	$6.25	20%	$1.37	141%
TX PH Granite Wash	4.75	$5.5	20%	$1.45	128%
Average	**4.36**	**$4.8**	**20%**	**$1.39**	**76%**

Figure 14: CHK Gas Type Curve

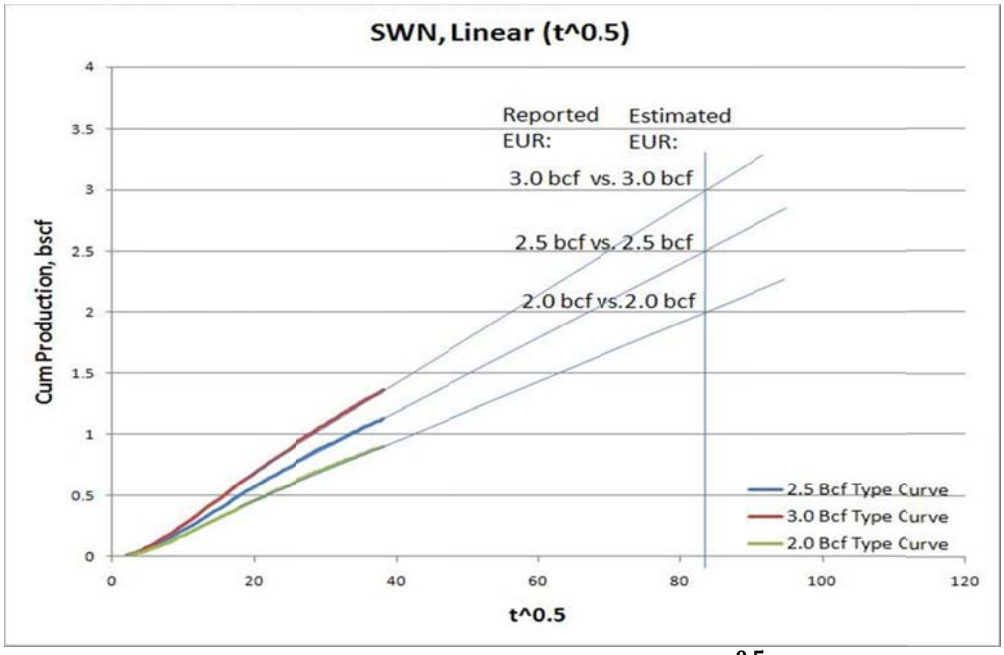

Figure 15: SWN Gas Type Curve Plot vs. $t^{0.5}$

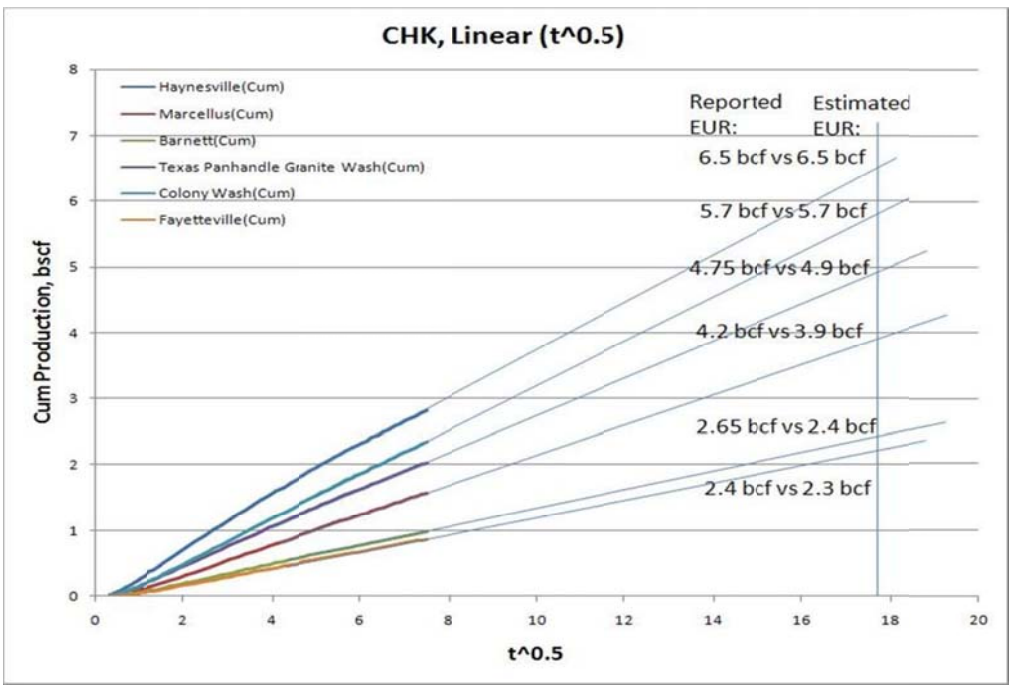

Figure 16: CHK Gas Type Curve Plot vs. $t^{0.5}$

Results and Discussion

We demonstrate the application of our methodology for a Wamsutter field. The details of the computer program to apply the procedure are provided in Appendix A. The permeability of this reservoir is very low. Currently, the study area in Wamsutter has 80-acre spacing and plans are to develop the field on 40-acre spacing. Average performance of 80-acre spacing wells is 50-70% of the performance of 160-acre spacing wells.[13] Our task is to determine the optimal location of infill wells and quantify the

potential recovery as well as acceleration and incremental production for 40-acre spacing wells. In Figure 17, we show the study area of 25 sections. The bubble map shows the EUR reported by the operator. Notice that in the field map, most of the wells are concentrated in the middle 3x3 section, so we focus our analysis on these nine sections. Further, we can see several big bubbles in the middle nine sections. We will evaluate the infill potential not only by single section, but also by multiple sections.

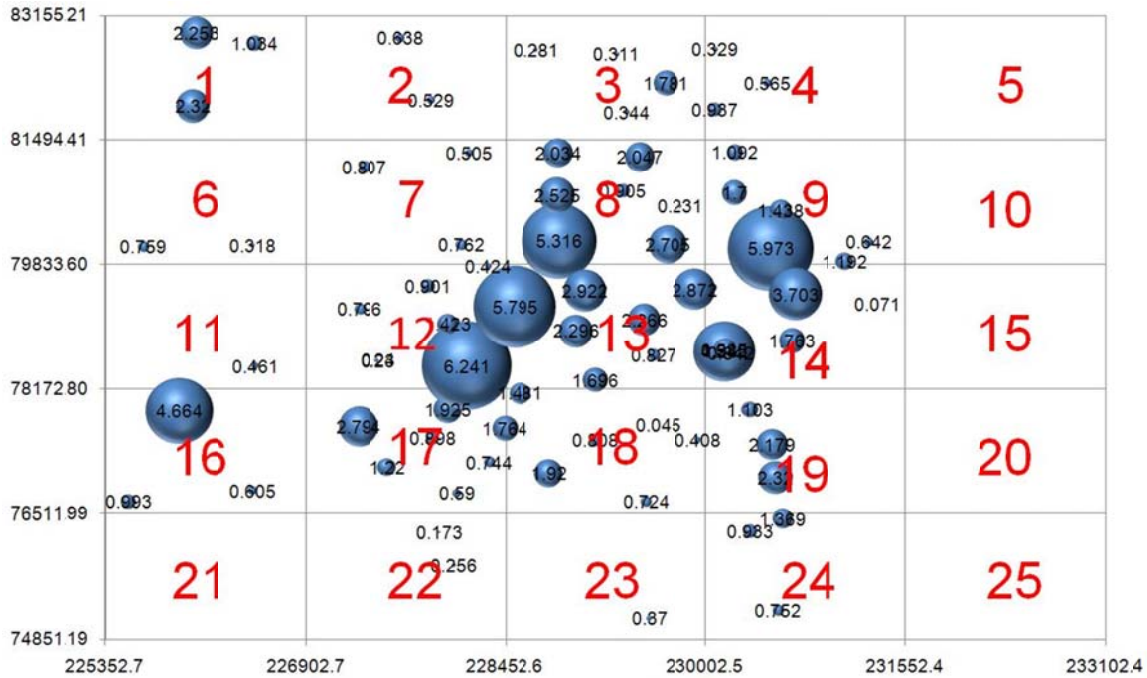

Figure 17: Area Map of Well Locations in Study Area

The first step of our method is to determine an appropriate time function to get a linear relationship with cumulative production. The linear relationship is very important. In Wamsutter field, we often observe linear or bilinear production. So, according to Equation 5 and Equation 9, we should get a straight line by plotting cumulative production versus a certain function of time.

In the study area, we need to select the analysis area. This area can be any shape but should at least contain 10 wells in order to get a reasonable statistical result. Our selected area can be a single section, multiple sections, or a smaller part of the section. When we predict our infill potential, it is applicable to that analysis area and not a specific location. The smaller the analysis area, the more precise the prediction, provided a sufficient number of wells are available in the analysis area. In Figure 17, we have used our analysis area as multiple sections. The sections are selected either in the north-south direction or the east-west direction. For example, we have analyzed the data by combining sections 7-8-9 as well as 7-12-17.

Once the wells are selected within the analysis area, they are sorted in chronological order. Then those wells are divided into 3 to 5 groups. The selection of the grouping is arbitrary and it is important that we have enough wells within each group to get statistically representative information. Figure 18 is an example of the grouping result. In this example, it is also possible to divide wells into more groups; however, all of these wells are drilled close to each other and it is not necessary to add more groups for this area. Further, we have found that the fewer groups provided, the more robust the results. Typically, 3 to 5 groups are sufficient for the analysis.

	API	Start Date
Group 1:	49007217380000	9/1/1982
	49007209470000	10/1/1984
	49007209460000	10/1/1984
Group 2:	49007211620000	10/1/1990
	49007212240000	1/1/1991
	49007213380000	9/1/1994
	49007213560000	10/1/1994
	49007213910000	2/1/1995
	49007213900000	2/1/1995
Group 3:	49007214350000	11/1/1997
	49007216850000	8/1/1998
Group 4:	49007220870000	9/1/2002
	49007223920000	8/1/2003
	49007224500000	1/1/2004
	49007224510000	9/1/2004
	49007229360000	7/1/2006

Figure 18: Grouping Example

For every individual well, acceleration and incremental production will be calculated by observing the plot of cumulative production versus time function. So we should plot cumulative production versus $t^{0.75}$ for bilinear flow and $t^{0.5}$ for linear flow. Using the most appropriate function, which provides a linear relationship, and extrapolating this straight line, we can calculate the total EUR for this well. In order to inspect the reliability of estimated EUR, we compare the extrapolated EUR with the reported EUR provided by the operator. If the EUR values are similar, we have more confidence in our analysis. We plot our data so that the linear relationship is observed, and then monitor the behavior after the next group of wells is drilled. If we observe inflection, we can extrapolate the performance before and after and, using the difference of the EUR at a certain time, we can quantify the amount of gas taken away by the new wells. Figure 19 shows an example of this procedure. First, we plot cumulative production until a second group of wells is drilled, which is the blue straight line. Then we extrapolate this straight line to get 3.9 BSCF for Group 1's EUR. We plot the data as red straight line until the third group is drilled, and then extrapolate to get 3.1 BSCF for Group 2. So the acceleration EUR of Group 2 is the difference of the two EURs, which is 0.8 BSCF.

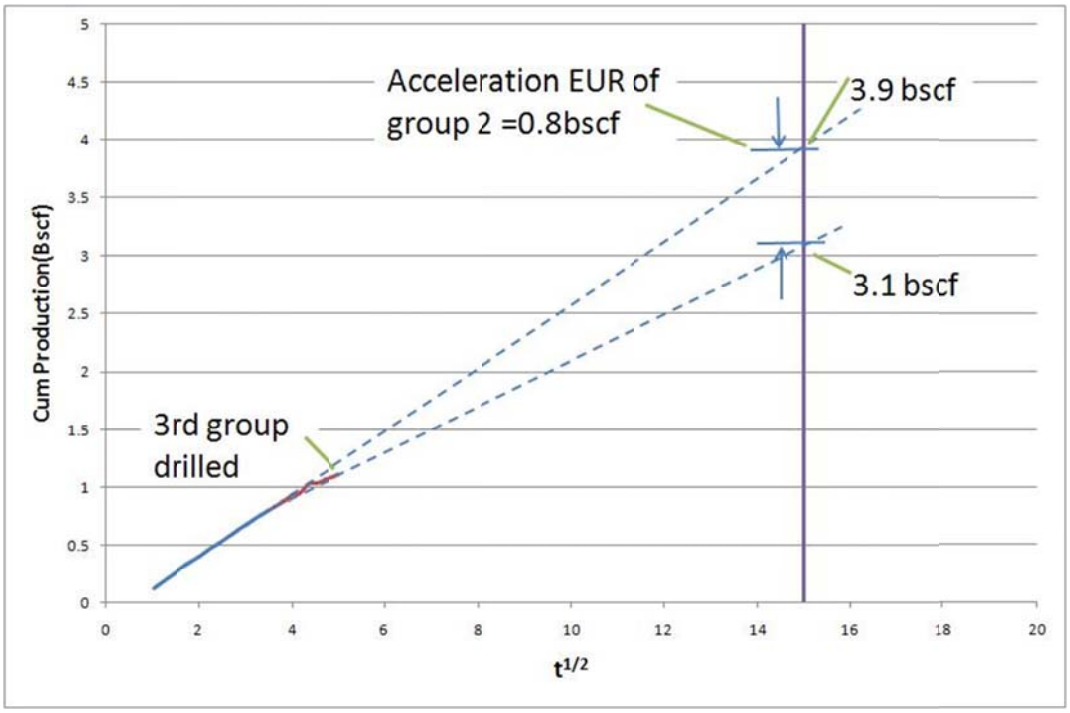

Figure 19: Acceleration Production

Similar calculations are carried out for all of the wells to determine the acceleration loss by the previous group of wells. The acceleration loss from all of the wells in the previous group, as a result of drilling wells in the next group, are added and equally divided among all of the wells in the next group. Therefore, if we know the EUR for the new group of wells, then by subtracting the acceleration component, we can estimate the incremental component for each well.

Using the multi-section area (either 3 sections in the north-south direction or in the east-west direction), we do the analysis for this field. We have a total of six analysis areas within the 3x3 core sections in the middle; three areas in the east-west direction and three in the north-south direction. To ensure that our results are reasonable, we compared our EUR values for all of the wells (based on a straight line approximation) with EURs reported by Devon, the operator of the area. Figure 20 shows the comparison of our calculation and Devon's calculation. The match is quite good indicating that our method is reasonable.

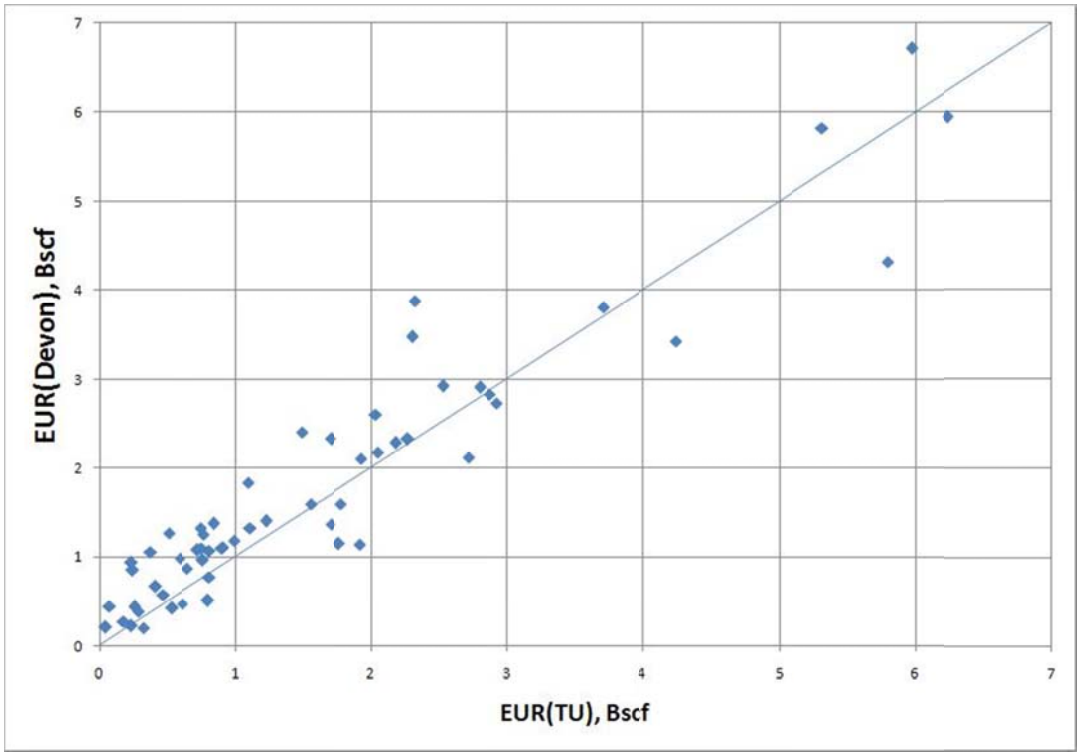

Figure 20: EUR Comparison

Once we determine the acceleration and incremental components for each group, we divide the total analysis area by the number of existing wells and determine the spacing. Using the spacing, we can generate the graph shown in Figure 21. This graph shows that, as the spacing declines, the acceleration percentage increases and the incremental percentage declines. The change may not always be smooth and monotonous, but is clear. We also show that the average EUR declines as the spacing increases. Using Figure 21 (or Figures 23 or 25) we can extrapolate to a lower spacing as shown in Figure 22 (or Figures 24 or 26). The method of extrapolation can be arbitrary. However, by using similar procedures, we can compare the results of various analysis areas objectively. From Table 4, one can evaluate which area has the best potential for the infill well. The criterion for determining a better section is by examining the higher incremental percentage as well as the higher total EUR of the section. According to the extrapolation results, EW-12, 13, 14 and NS-9, 14, 19 are the two areas that have better potential for infill drilling. These are the two areas we recommended to Devon for drilling additional wells.

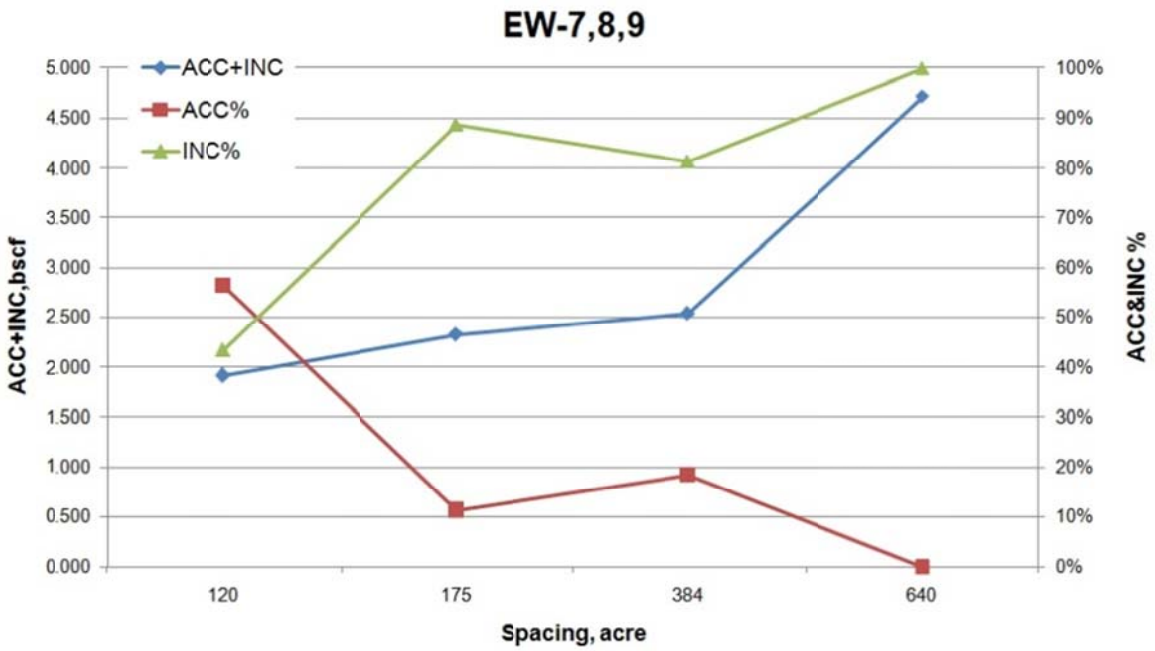

Figure 21: Acceleration vs. Incremental Plot of EW-7, 8, 9

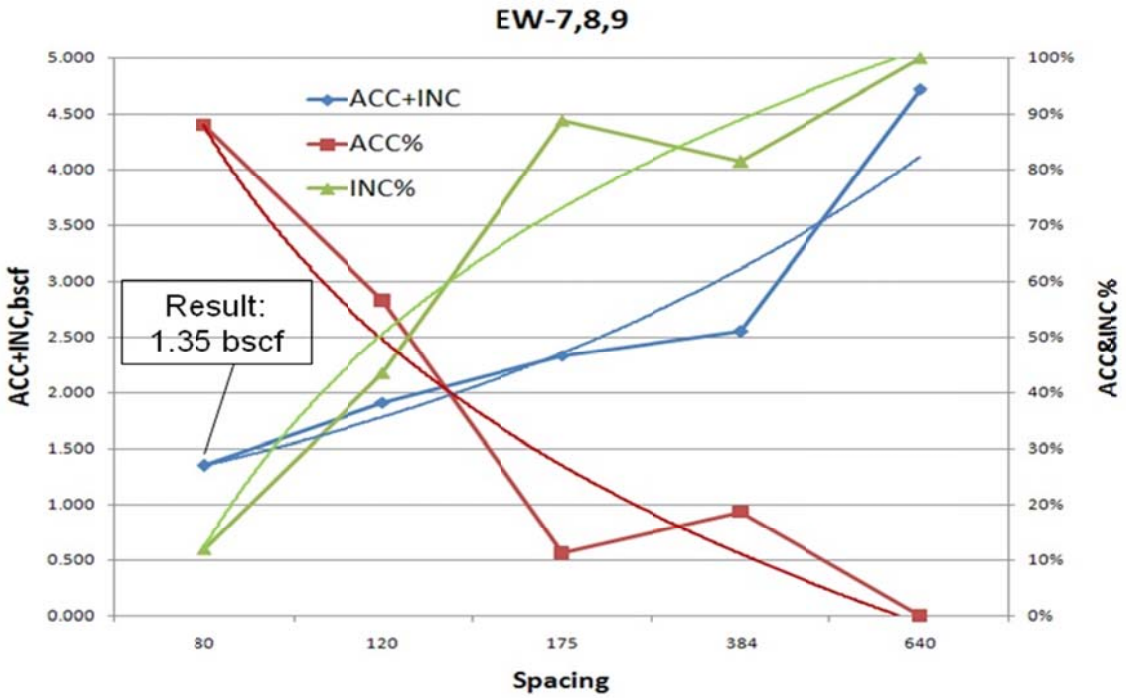

Figure 22: Extrapolation to Lower Spacing of EW-7, 8, 9

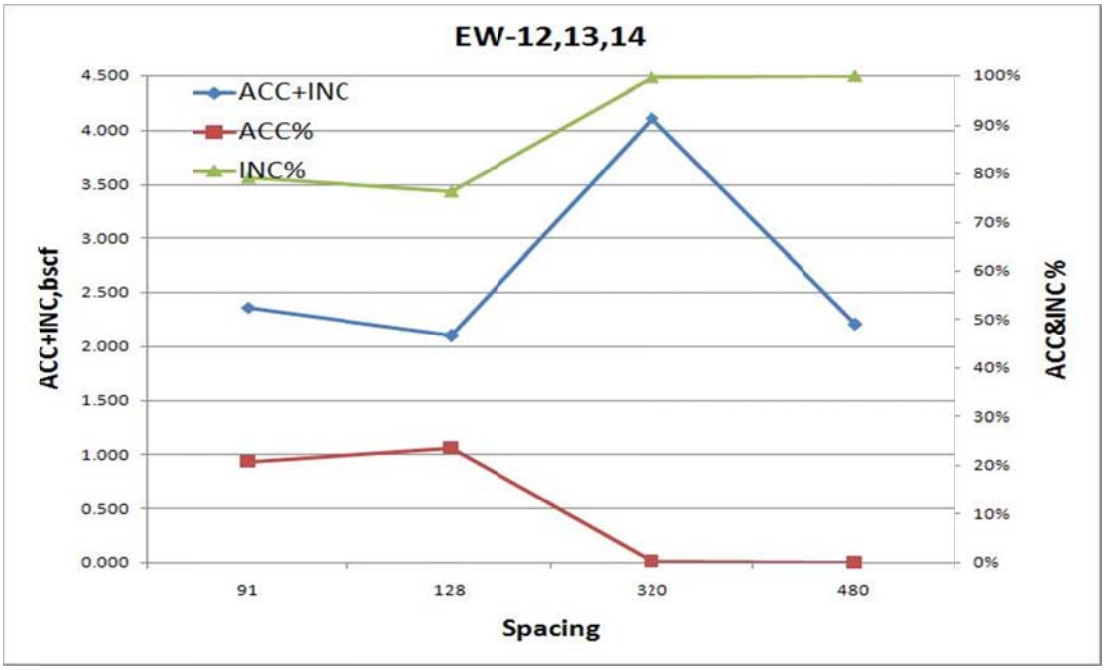

Figure 23: Acceleration vs. Incremental Plot of EW-12, 13, 14

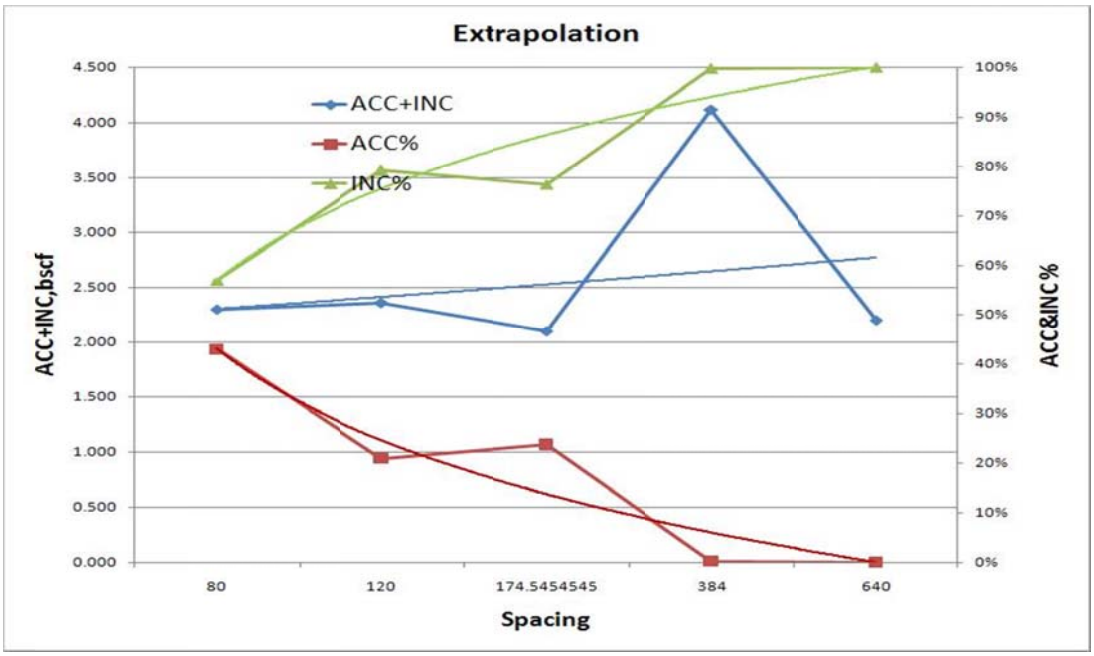

Figure 24: Extrapolation to Lower Spacing of EW-12, 13, 14

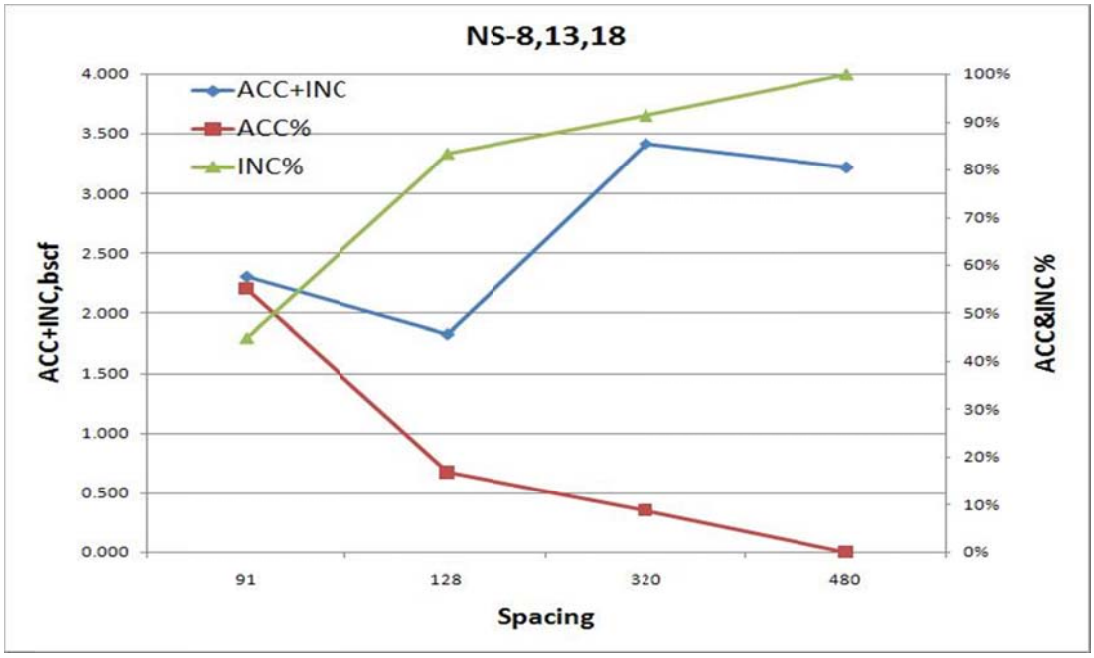

Figure 25: Acceleration vs. Incremental Plot of NS-8, 13, 18

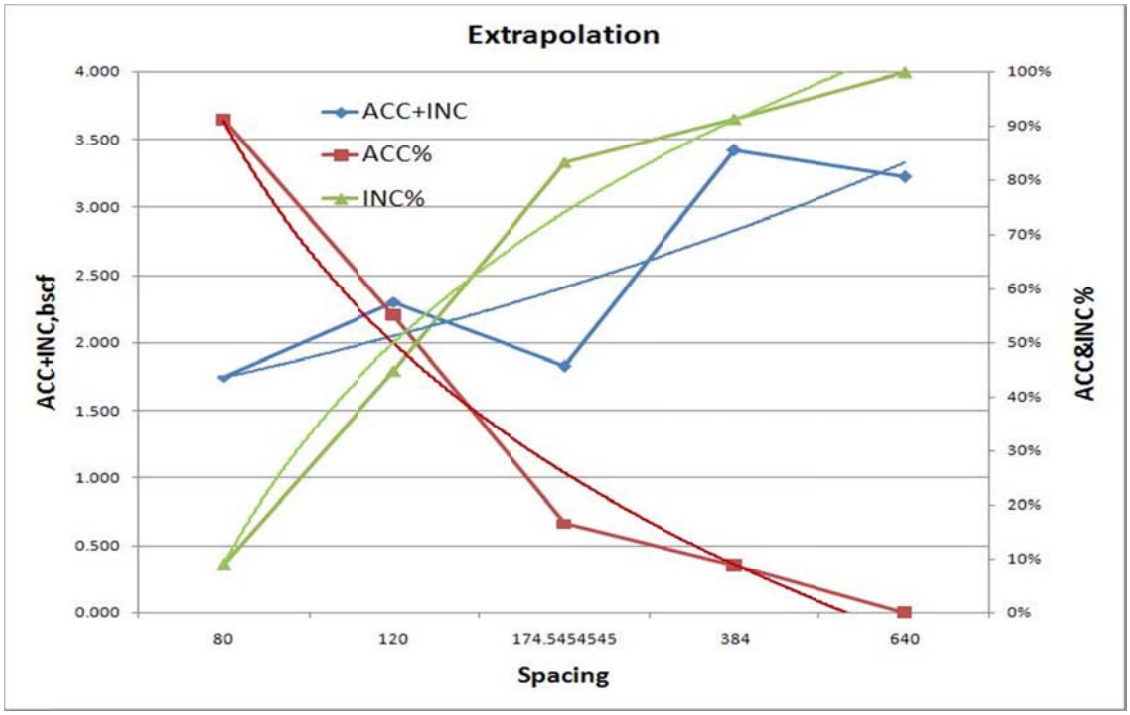

Figure 26: Extrapolation to Lower Spacing of NS-8, 13, 18

Table 4: Infill Potential Comparison

	Total (bscf)	%(ACC)	%(INC)
EW-7,8,9	1.350	88%	12%
EW-12,13,14	2.300	43%	57%
EW-17,18,19	2.140	84%	16%
NS-7,12,17	0.900	70%	30%
NS-8,13,18	1.750	91%	9%
NS-9,14,19	2.150	64%	36%

SIMULATION PERFORMANCE PREDICTION

In addition to developing a method to determine the infill well locations based on production data, we also examined the performance based on a detailed simulation study. This involved building a detailed geocellular model, upscaling the model to a simulation model, history matching the production performance and predicting the future performance for the proposed wells.

Geological Model

The first step was the construction of a structural model defining various geological zones. The next step was to define the spatial continuity of various reservoir properties. After that, the reservoir's petrophysical properties model was built. Each of these steps is described below.

Structural Modeling

Based on the geological input, the reservoir was divided into four zones: Bar (Almond Bar), Upper Almond, Middle Almond and Lower Almond. This required defining five markers for surface mapping. Using the data for 77 wells, the following surfaces were built: Bar Top, Upper Top, Middle Top and Lower Top and Erickson (lower bottom). Each of the surfaces is shown in Figures 27-31.

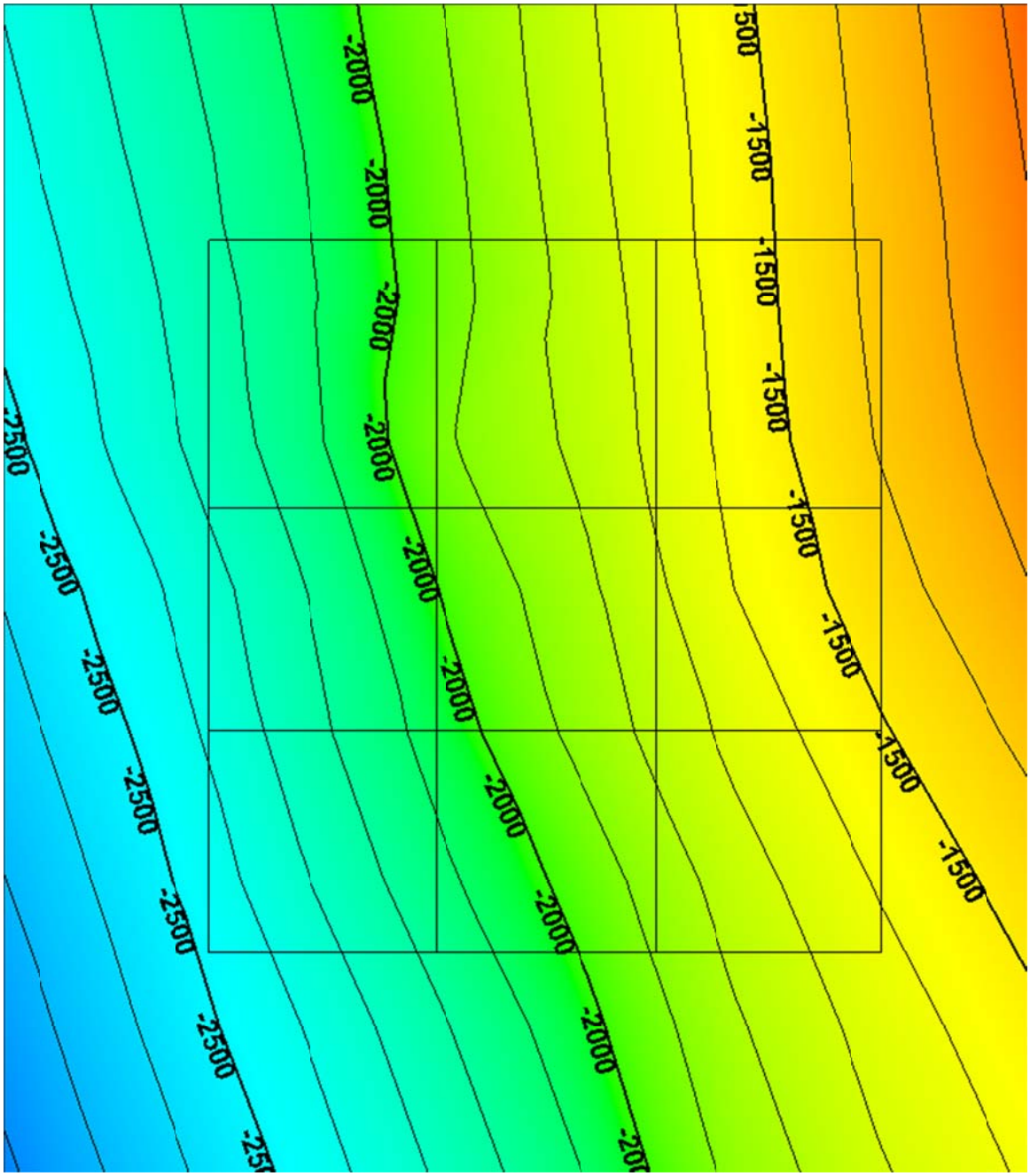

Figure 27: Almond Bar Top Surface

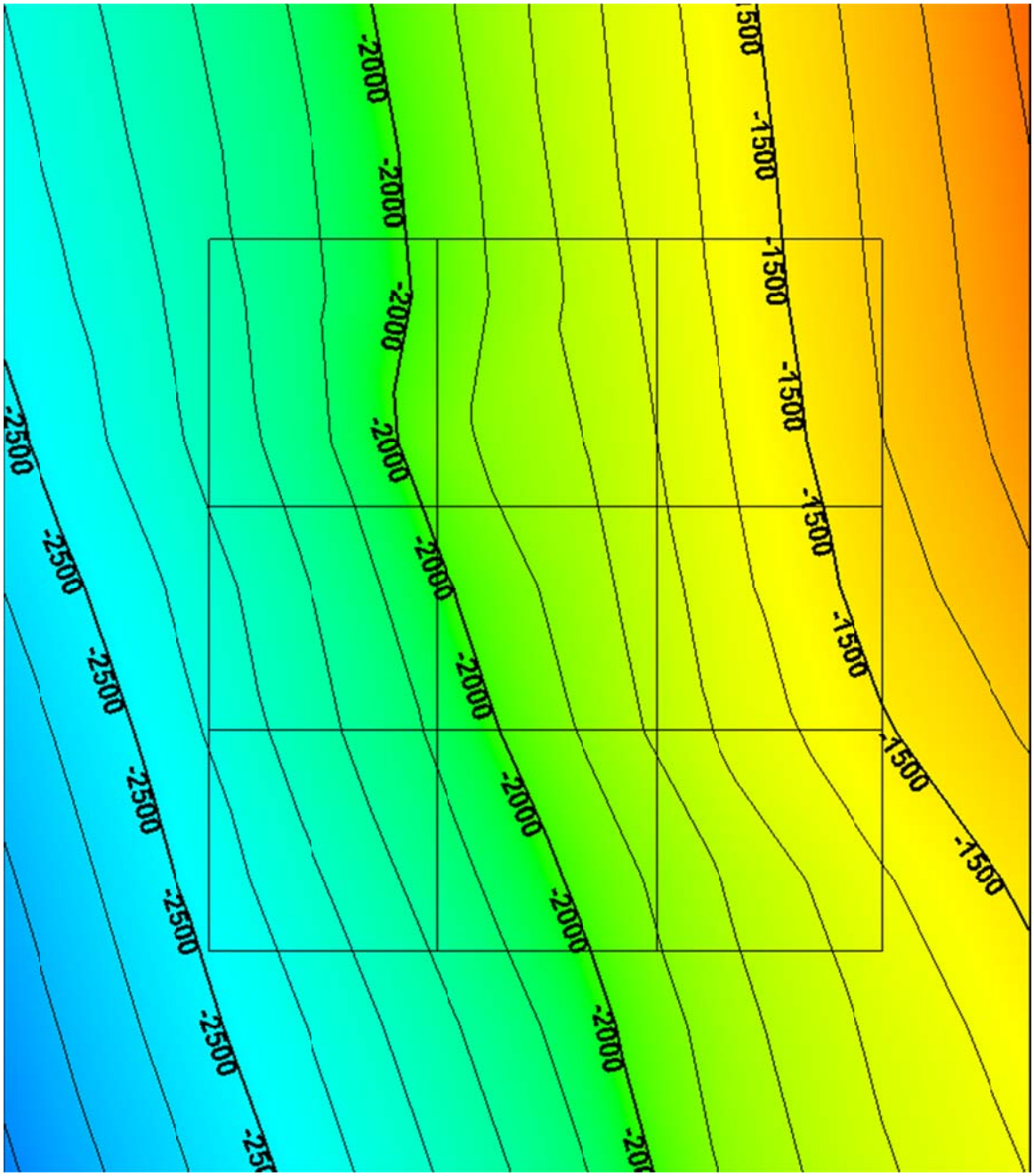

Figure 28: Upper Almond Top Surface

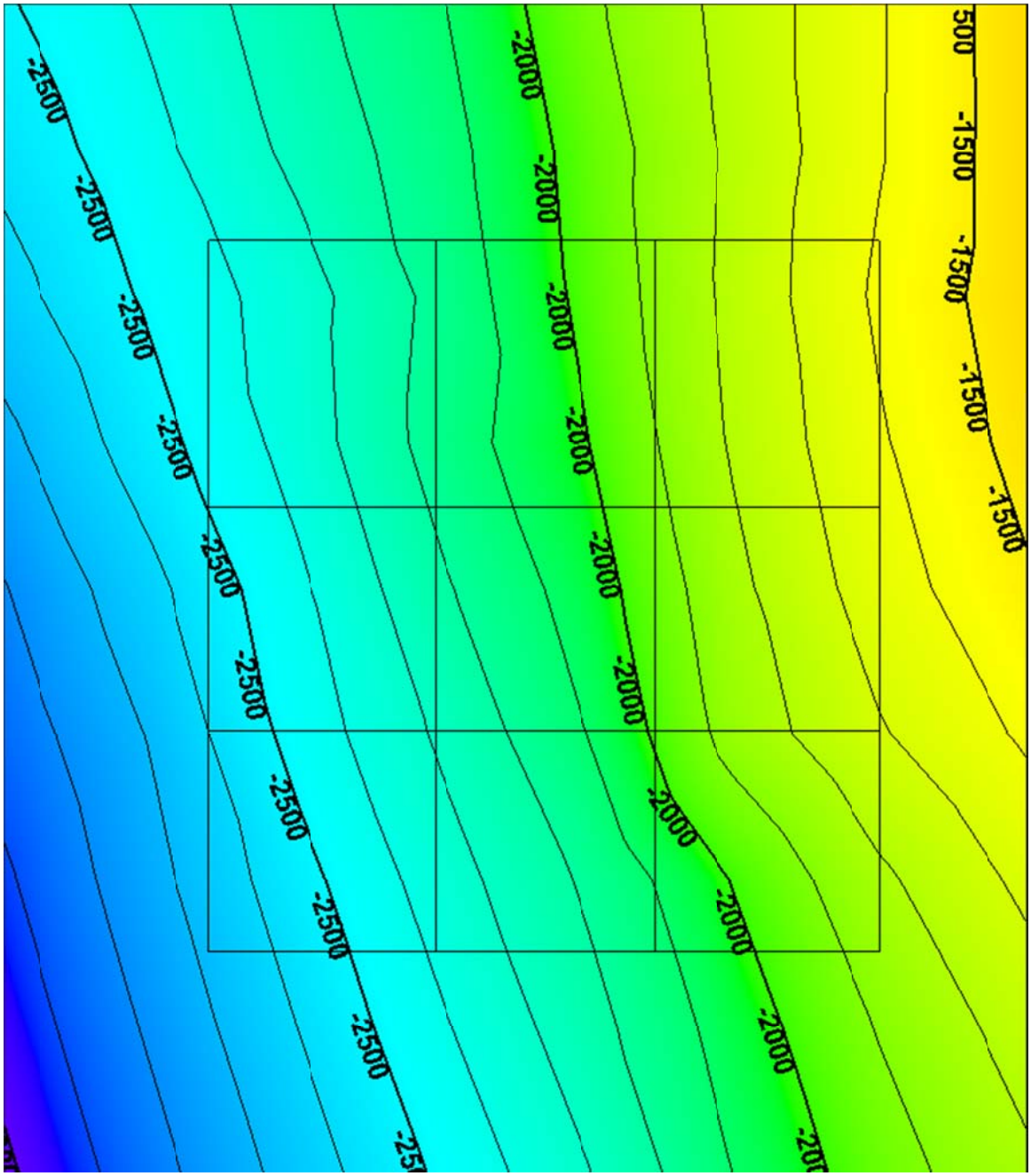

Figure 29: Middle Almond Top Surface

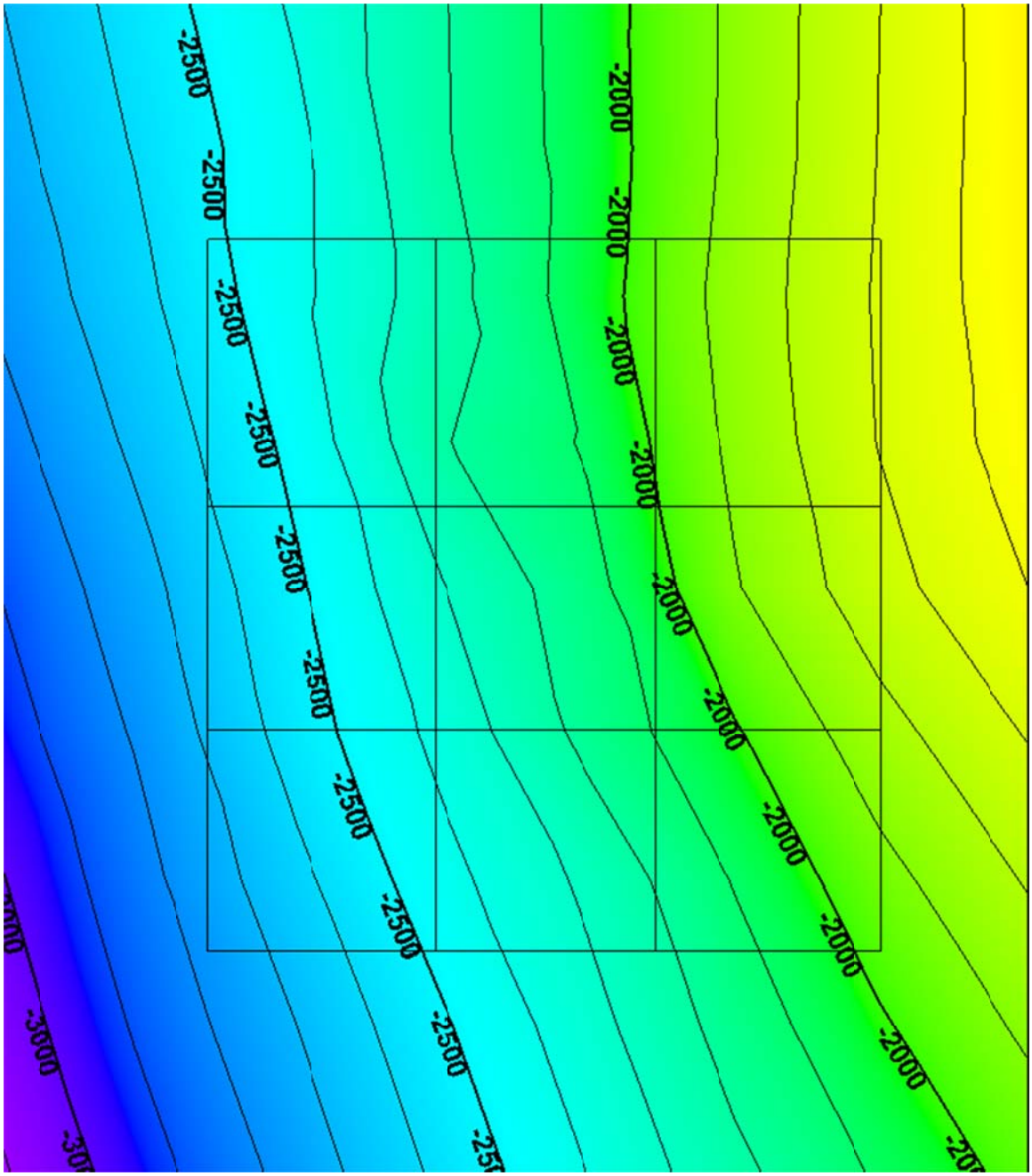

Figure 30: Lower Almond Top Surface

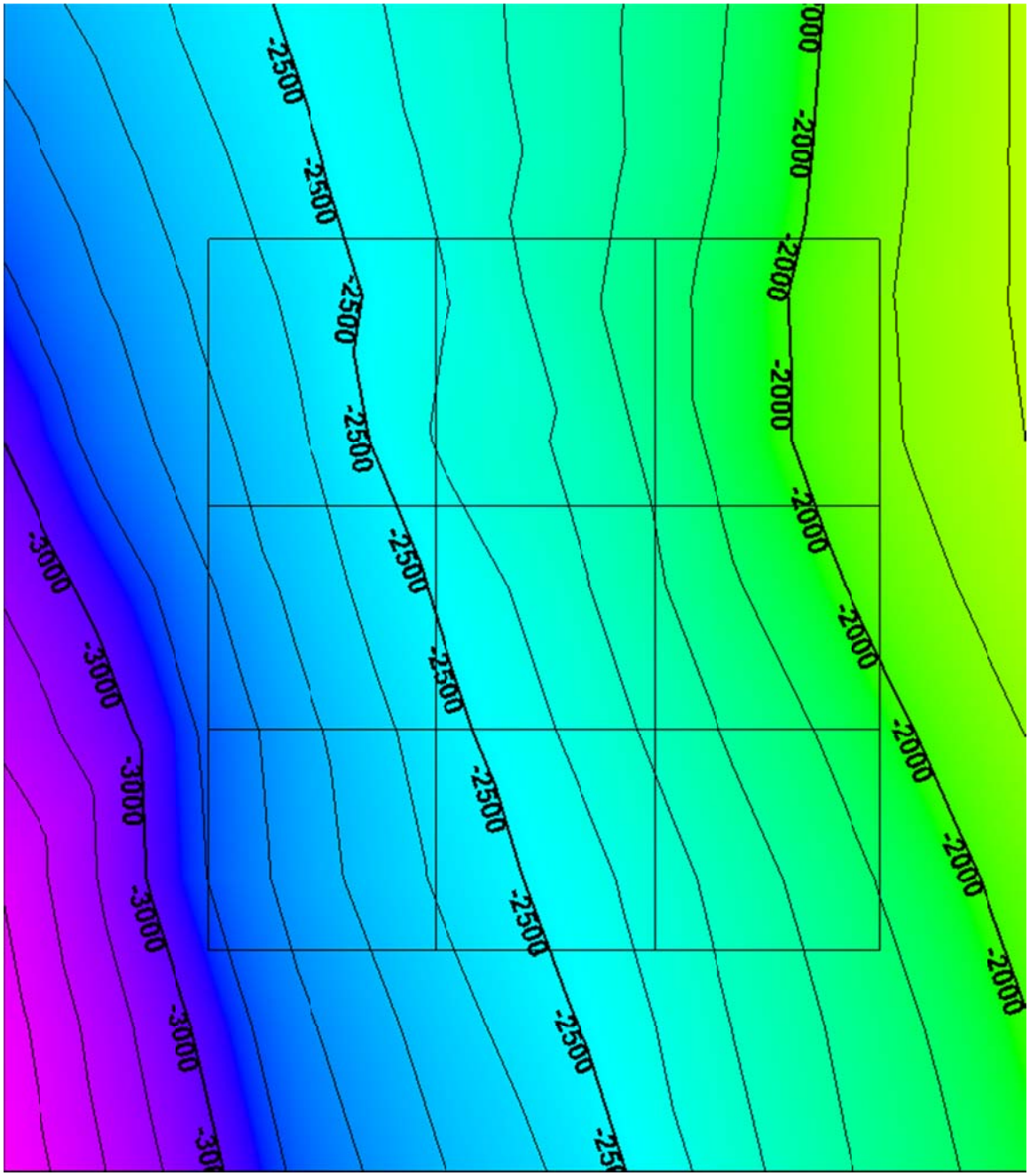

Figure 31: Ericson Top Surface

As shown, the surfaces are smooth with gentle changes and no visible faults. Typical cross-sections with effective porosity logs are shown in Figures 32 and 33 with their areal location shown in Figure 34. Figure 32 represents an east-west cross section, whereas Figure 33 represents a north-south cross section.

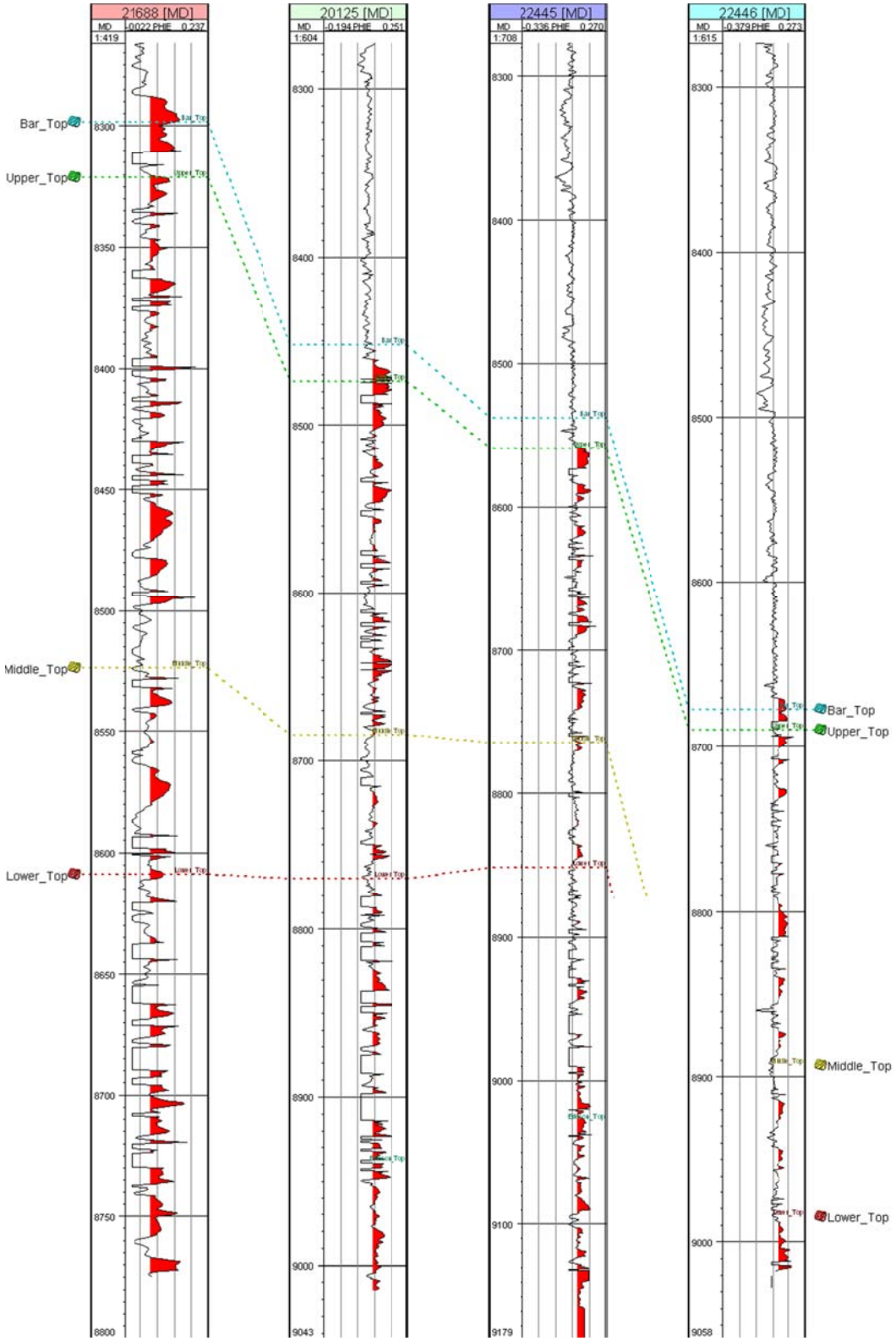

Figure 32: East-West Almond Cross Section

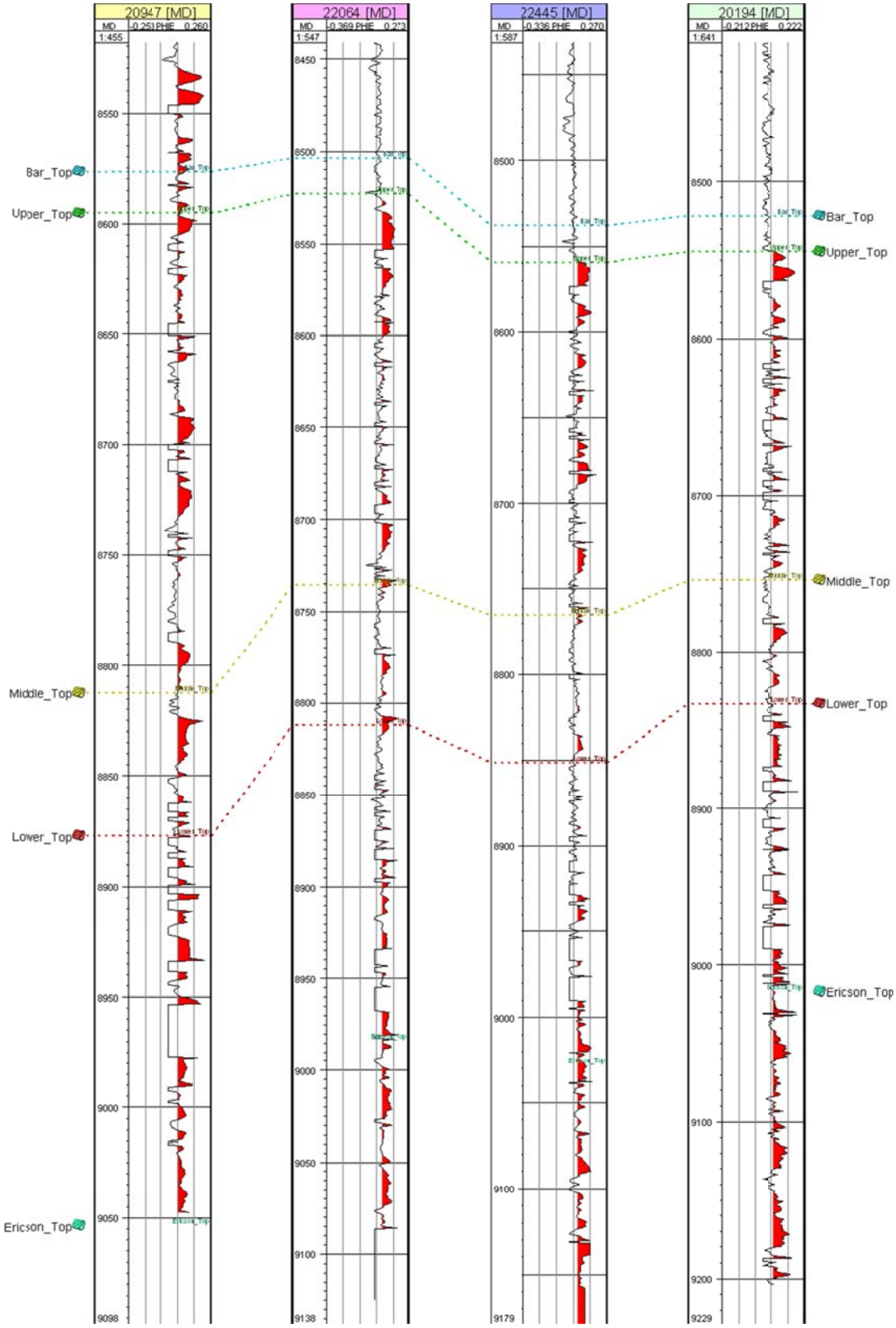

Figure 33: North-South Almond Cross Section

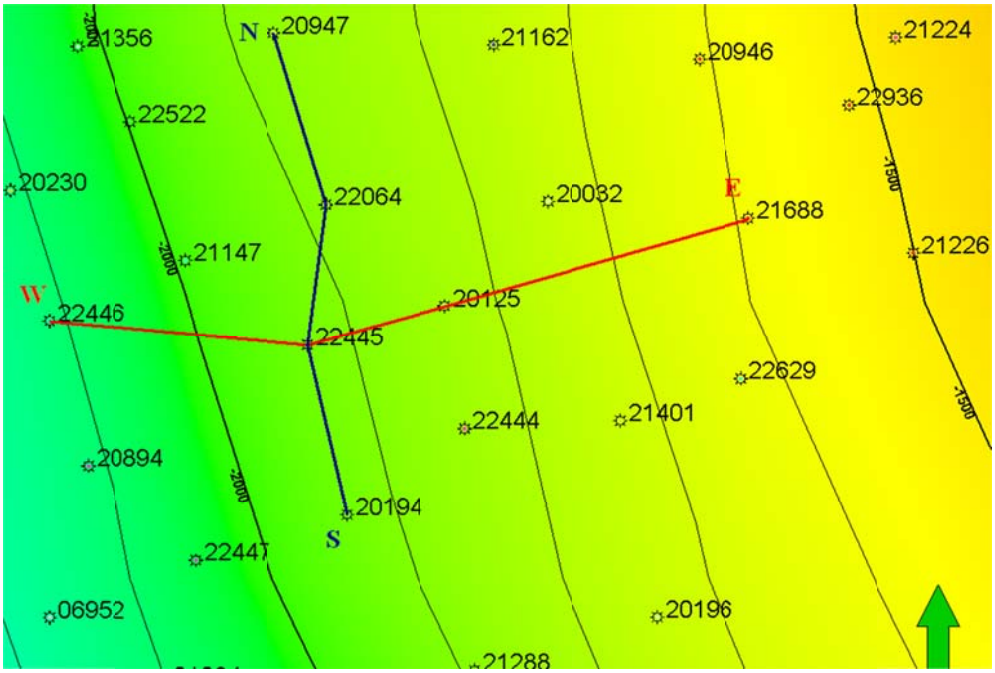

Figure 34: Cross Section Top View

The next step was to define the layers within each zone. Well log files suggest that the data were sampled every 0.5 ft. Therefore, the decision was made to split the zone into certain layers in order for the minimum layer thickness to be 1 ft. Therefore, layering was based on the smallest thickness between the surfaces. Each zone was divided using the proportional method. That is, there was no truncation of layers due to erosion. This assumption was consistent with geological input.[14]

The areal grid size was defined as 250 ft. by 250 ft. The final result was the fine-scale model having 4 zones, 5 horizons, 361 layers and 3,962,336 cells.

Property Modeling

In general, there were three facies from two logs: pay sand, shale and coal from the pay flag and coal flag curves. A pay flag curve value of zero stands for shale and coal. After not seeing a decent correlation between coals, we were informed that we should not force a correlation among the coals.[14]

Consequently, the pay flag log was chosen as the facies log. Therefore, the model had only two facies: pay sand and everything else which includes shale, non-pay sand and coal. For simplicity names in the model were "sand" for pay sand and "shale" for everything else. The values were assigned "1" for sand and "0" for shale.

Scaled-Up Well Logs

The porosity, permeability and facies logs were scaled-up for further analysis to ensure that there was only one value for each grid in the vertical direction. A volume weighted averaging algorithm was used in all properties. Averaging methods were "most of" for facies and "arithmetic" for porosity and permeability. The upscaled value using the "most of" method

corresponded to the value that was most represented in the log for that particular cell. The first log to be upscaled was the facies log because porosity and permeability averaging had to be biased by the facies type.

Spatial Continuity

Spatial relationships define the continuity of various petrophysical attributes. The most important spatial relationship is that of facies, since it provides the underpinning of spatial relationships for both porosity and permeability. Conventional variogram analysis was used for describing the spatial relationship; however, before doing that analysis, spatial continuity was examined by evaluating our production data against each of the geological zones.

Intuitively, if a particular geological facies was more continuous, they would be drained more efficiently by prior wells; hence, the infill wells would not be able to recover much gas from the drained reservoir. In order to test the hypothesis, all of the wells were divided into the chronological groups 1980–2000 and after 2000. The EUR values for each well were plotted against net thickness for each geological zone. Figure 35 shows an example of EUR versus net thickness of the Almond Bar sand.

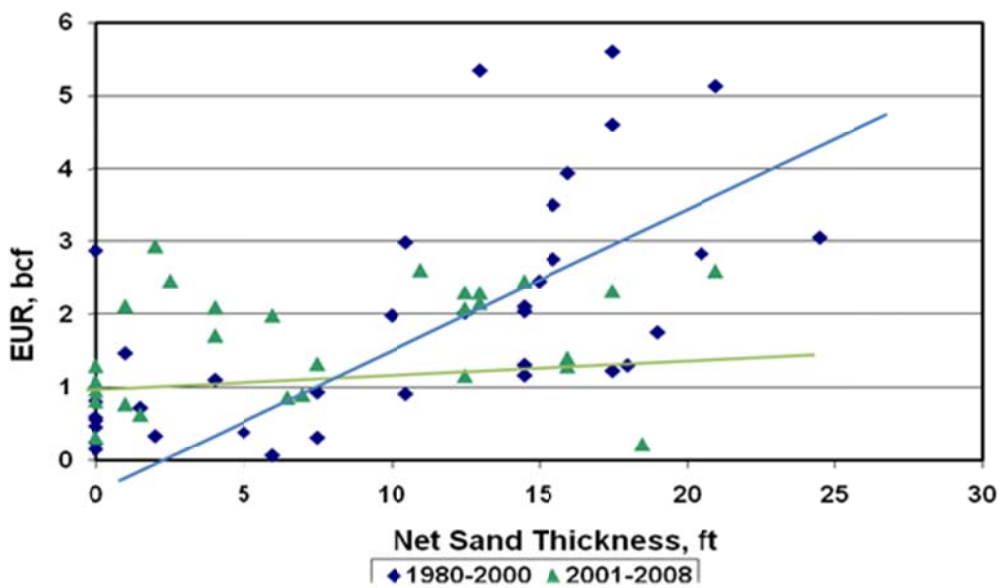

Figure 35: EUR versus Almond Bar Net Thickness

As shown, the earlier wells have a good relationship with net sand of the Almond Bar. This indicates that the early production from the wells was influenced by the presence of the Almond Bar. However, as the Almond Bar was drained, the new wells did not benefit as much from it. This graph also indicates the importance of the Almond Bar in determining the EUR of earlier wells. Figures 36-38 show similar graphs for other zones.

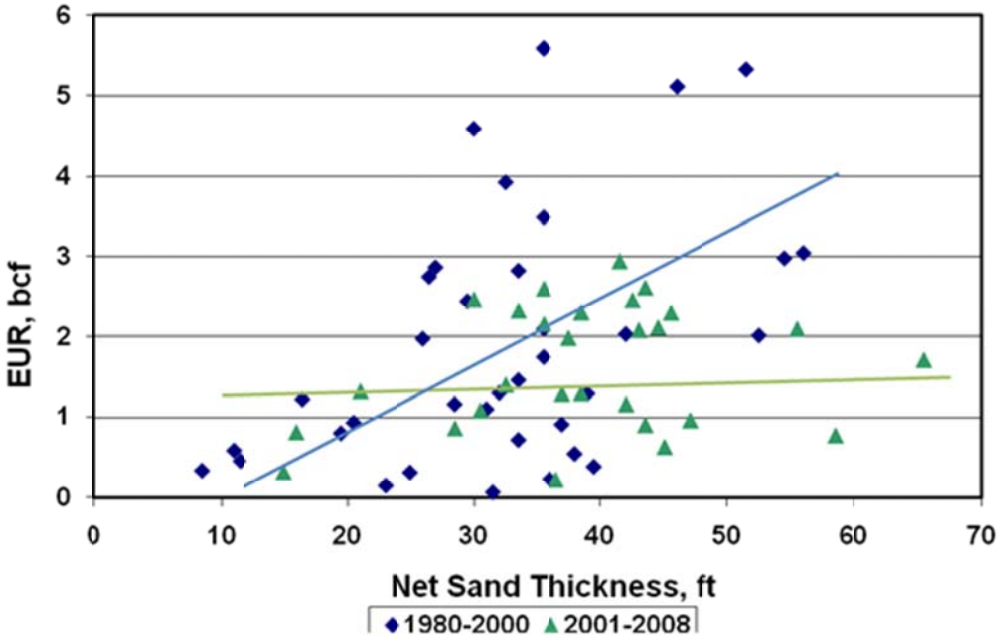

Figure 36: EUR versus Upper Almond Net Thickness

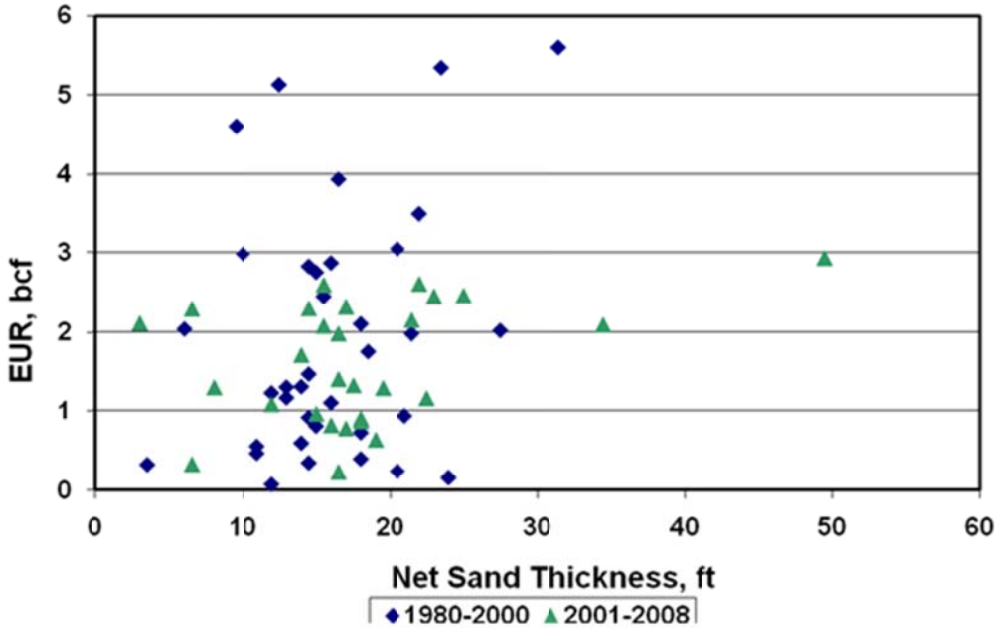

Figure 37: EUR versus Middle Almond Net Thickness

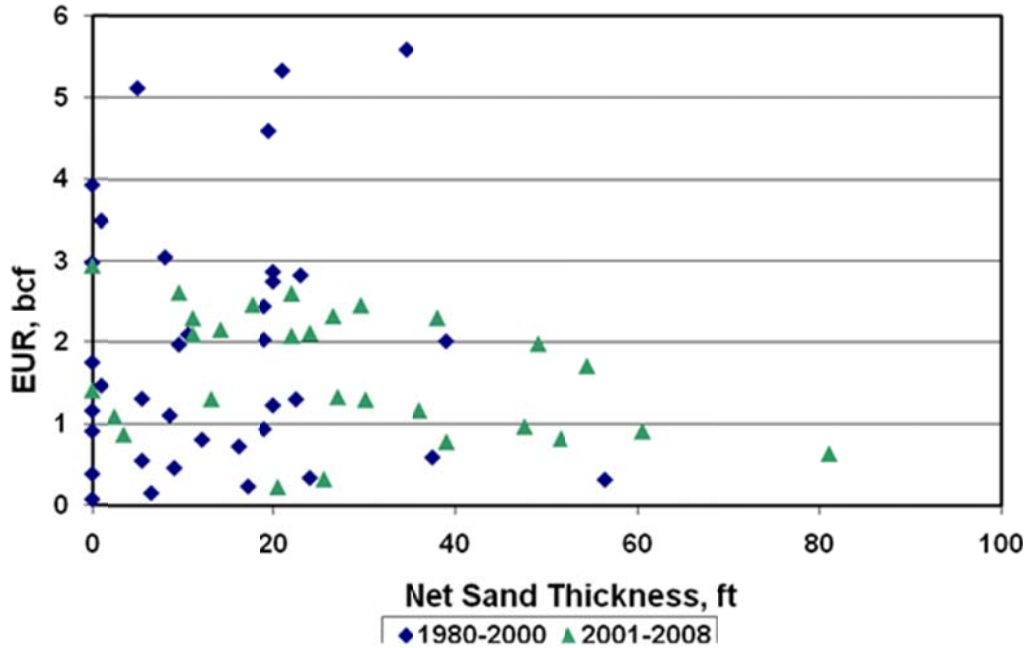

Figure 38: EUR versus Lower Almond Net Thickness

Based on this information, it was understood that the Almond Bar exhibited the most continuity followed by the Middle Almond, the Upper Almond and the Lower Almond. Further discussion with Andrew Stirling, Geologist from Devon Energy, also indicated that sands were more continous in the north-south direction than in the east-west direction.[14] Using this information, variograms were constructed for each sand using the well data. Figure 39 shows an example variogram for the Almond Bar.

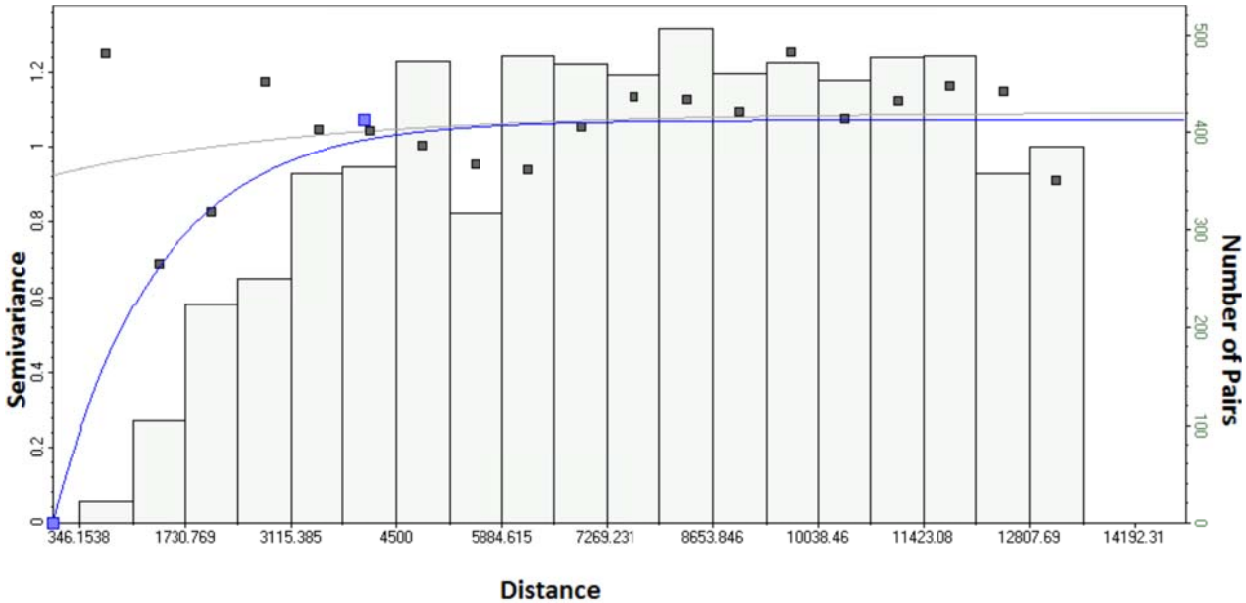

Figure 39: Bar Facies Major Variogram

Similar variograms were constructed in other zones as well. Table 5 summarizes the variogram parameters used in constructing the variogram models. All variograms used were exponential.

Table 5: Facies Variogram

Facies Variogram				
	Major Range,ft	Minor Range,ft	Vertical Range, ft	Azimuth
Bar	4100	2000	8	35
Upper	1740	1660	8	35
Middle	2400	1700	12	110
Lower	2800	1800	10	35

Porosity and permeability analyses were biased by the facies type. In other words, each facies had its own distribution of those properties. Properties in shale were not analyzed, because its values would be modeled as zeros. Thus, if the facies simulation assigned shale in a particular cell, then petrophysical simulation would assign zero porosity and zero permeability in that cell.

Transformations were applied to the porosity input data including input and output truncations and the normal-score. Truncations ensured that the porosity modeling in sand facies would not assign value less than 6% in order to meet porosity cutoff. And the normal-score transformation was the transformation of sample data into equivalent data that follow a normal (Gaussian) distribution for further use of the Sequential Gaussian Simulation for property distribution. The probability curve was fitted to the histogram of the actual sample data and smoothing was applied once. Variogram analysis for porosity was the same as for facies. Variogram types were exponential for the Bar and Upper zones, and spherical for the Middle and Lower zones.

Permeability is usually log-normally distributed. Therefore, two transformations were applied to the permeability sample data: the log-normal distribution transformation and then the normal-score transformation. The same procedure of variogram analysis as for facies and porosity was applied for permeability. All variogram types were exponential except for the Bar which was spherical. Tables 6 and 7 show porosity and permeability variogram parameters.

Table 6: Porosity Variogram

Porosity Variogram				
	Major Range, ft	Minor Range, ft	Vertical Range, ft	Azimuth
Bar	2050	1500	13	75
Upper	2500	2200	7	35
Middle	3200	1700	7	20
Lower	2150	1950	10	305

Table 7: Permeability Variogram

	Permeability Variogram			
	Major Range, ft	Minor Range, ft	Vertical Range, ft	Azimuth
Bar	3650	3050	8	295
Upper	2300	2300	6	0
Middle	2222	1500	10	0
Lower	1900	1000	10	20

Facies Modeling

Facies were modeled for each zone separately using Sequential Indicator Simulation with ordinary kriging.[15] Variogram and vertical proportion curves were taken from the previous step.

Petrophysical Modeling

Porosity and permeability were also modeled in one zone at a time, and they were biased by the facies type. As mentioned before, the shale facies type was assigned a constant value of zero porosity and permeability. Sand facies were distributed with Sequential Gaussian Simulation with ordinary kriging.[15] Variograms and transformations were taken from the previous step. Once porosity was determined, permeability was estimated using a collocated cokriging procedure.

In the end, the fine-scale model had distributed properties of facies, porosity, and permeability. The final facies property model honored the facies vertical probability curve, their spatial relationship, and data at the wells. The permeability model honored the correlation with porosity with the average correlation coefficient of 0.45 for all the zones. Permeability was assumed to be isotropic in all 3 directions. Figures 40-42 show examples of various properties. As clearly shown, the facies distribution has a strong influence on porosity and permeability distributions.

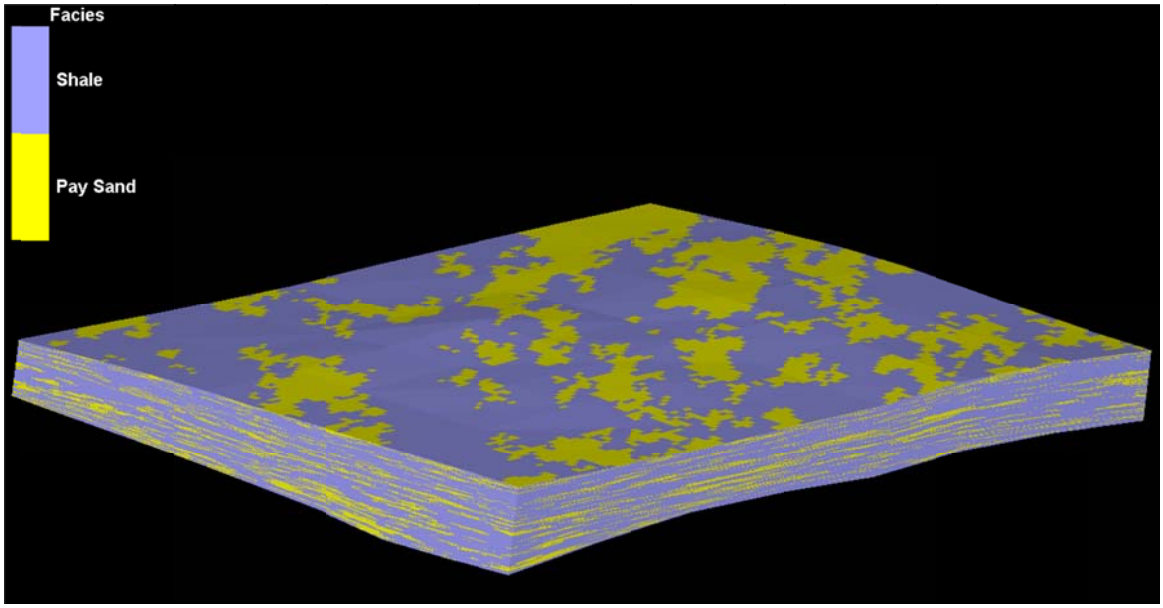

Figure 40: Facies Fine-Scale Property Distribution

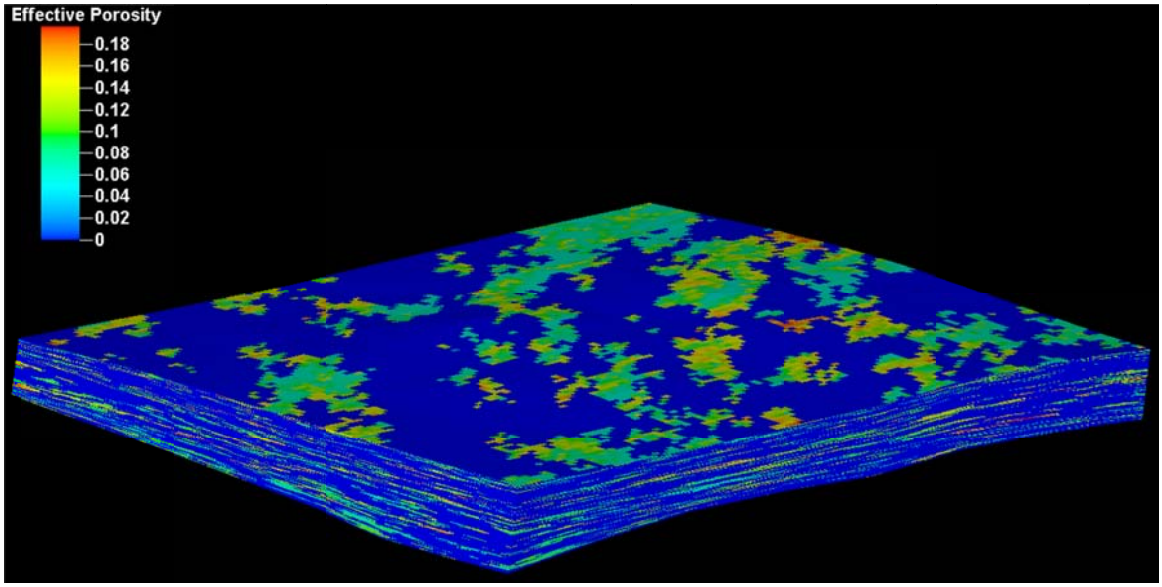

Figure 41: Porosity Fine-Scale Property Distribution

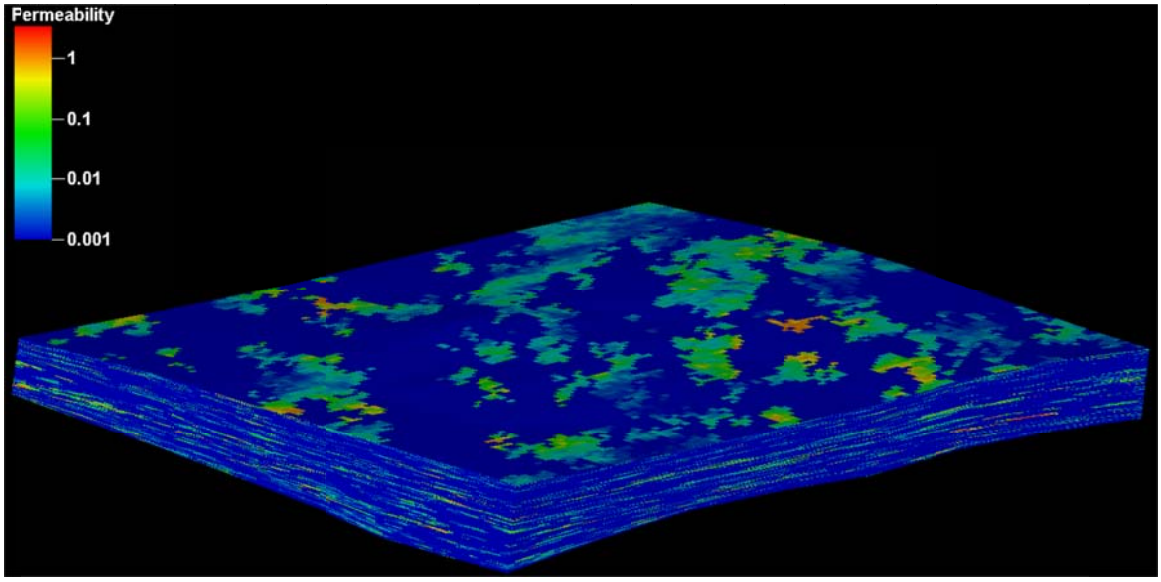

Figure 42: Permeability Fine-Scale Property Distribution

Simulation Model

Upgridding and Upscaling

Simple single-phase simulations were possible to run on the fine-scale model; however, integration of the Local Grid Refinement option was necessary to represent hydraulic fractures in every well, which necessitated reducing the size of the fine-scale model to a reasonable size to run it efficiently.

Key points to be considered when performing upscaling were pore-volume preservation and dynamic connectivity. Preserving fine-scale dynamic connectivity was crucial in this project. The most commonly used design for upgridding is a proportional method. It simply allocates the number of layers in each zone of the fine-scale model to the coarse-scale model such that each coarse-scale layer contains approximately the same number of fine-scale layers. For example, in order to upscale 160 layers of the Upper Almond into 40 layers, the proportional method would combine every four fine-scale layers regardless of the geology and dynamic properties. Therefore, the decision was made to use the pressure-based method proposed by Hosseini and Kelkar.[16] This method calculates a pressure profile for each layer using Darcy's law, so that layers with similar profiles can be combined in upgridding. For every layer design, it gives the design factor and error per layer. The design factor shows the advantage of selecting a given layer combination over that reported when using the proportional method. Error per layer is the total error at a particular iteration divided by the number of layers at that iteration.

The pressure-based method was available through the software package CONNECT with two modules: UpGrid and TransMod.[17] Input data for UpGrid were the fine-scale porosity and permeability. Once the program was finished with calculations, it was possible to choose the number of layers for a coarse model which had a high design factor and very small error per layer. Once the number of layers was chosen to be forty-four, the program showed layer design and fractions. An example is shown in Figure 43.

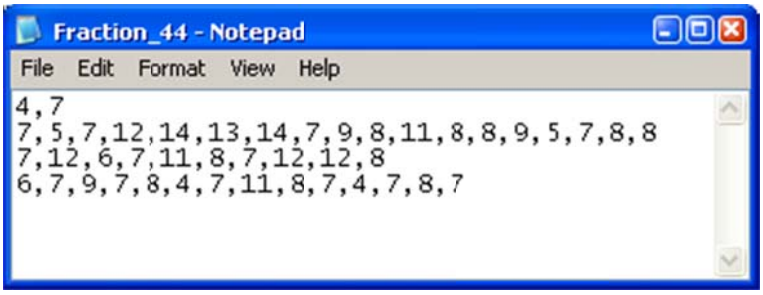

Figure 43: Fractions for Upscaling

Suggested fractions were used to scale up the structure with the method of fractions. Only vertical upgridding was performed. No areal upgridding was done.

Upscaled properties included facies, porosity and permeability in all three directions. A volume-weighted averaging algorithm was used for all the properties. The averaging methods were "most of" for facies, "arithmetic" for porosity and both X and Y permeabilities, and "harmonic" for vertical permeability. The layer design was restricted to the new coarse-scale layers.

In order to maintain the same dynamic connectivity, the TransMod program was used to solve for transmissibility multipliers in all three directions.

Figure 44 illustrates a comparison of three Field Cumulative Production curves: a fine-scale model with 361 layers and two coarse-scale models with 44 layers which were upscaled using the proportional method and the pressure-based method. The match between fine- and coarse-scale models using the pressure-based method was good; therefore, fine-scale details were not lost by upscaling. We decided to use 44 layers in our model.

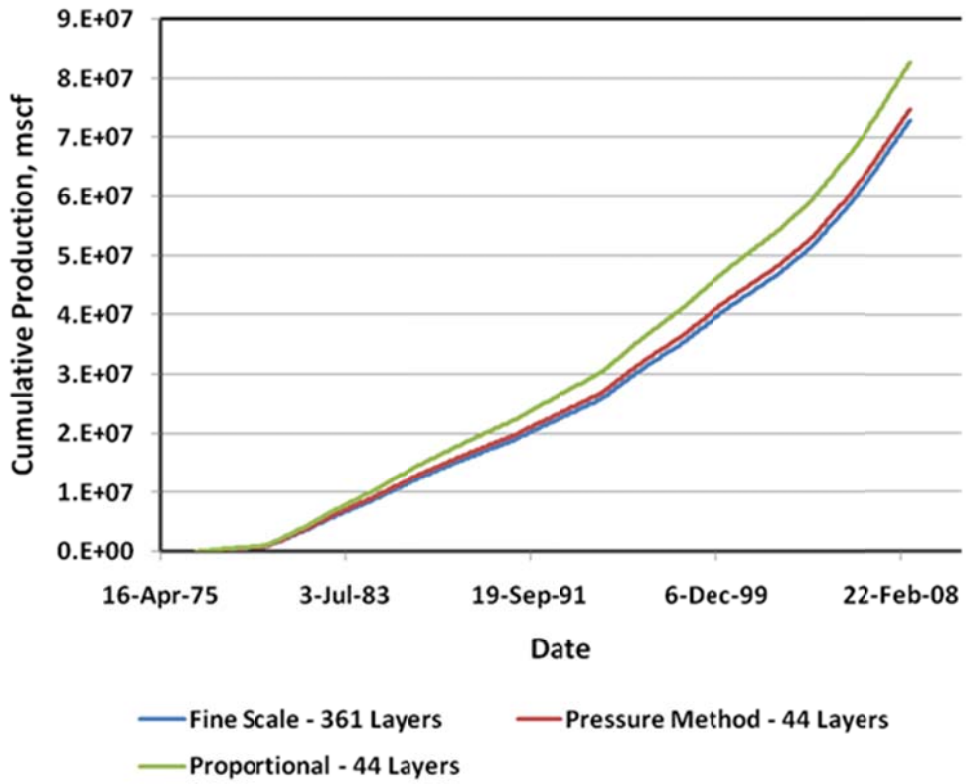

Figure 44: Field Cumulative Production for 361 and 44 Layers (Pressure and Proportional Methods)

Local Grid Refinement

Two ways of modeling hydraulic fractures were considered: PETREL-style hydraulic fracture and Local Grid Refinement (LGR).[18] The first option is available in the Completions Manager window in PETREL. It requires fracture half-length, azimuth, and conductivity as input parameters. It simply creates a box around the well. The box is proportional to the half-length and PETREL modifies transmissibility multipliers in the enclosed grid blocks. That might replicate the stimulation in a shale formation, but it is not likely to be appropriate for tight sandstone.

As a consequence, Local Grid Refinement (LGR) was chosen because it would create linear flow. It increases resolution near wells and allows specifying properties in the near-wellbore region. The smallest possible LGR is built within the grid blocks that are penetrated by the wellbore. An additional influence distance can be assigned, so that LGR can be extended to surrounding cells. A Cartesian refinement method was used with a constant number of cells in X (N_x), Y (N_y) and Z (N_z). Each host cell was subdivided into a number of smaller cells in three directions according to N_x, N_y and N_z.

The fracture was oriented in a north-south direction. Therefore, the grid blocks were refined in "I" direction. Several settings were tried in order to determine the optimum number of local cells. The final settings were $N_x = 25$, $N_y = 1$ and $N_z = 1$. Thus, the grid blocks to show the influence of LGR were divided into twenty five smaller blocks in the "I" direction, and had the original resolution in the "J" and "K" directions.

Since every grid block has a dimension of 250 ft. by 250 ft., the smallest half-length possible was 125 ft. The width of the fracture was assumed to be 10 ft. In fact, most of the wells in the model had a half-length of 125 ft. Consequently, well coordinates used in the simulation were also adjusted because of LGR. Wellheads received new local coordinates; therefore, if the wellhead was positioned at "I" = 5 and "J" = 10 in the global grid then, after performing LGR, it would have a new local "I" coordinate between 1 and 25 but within the same host cell, whose global coordinates were "I" = 5 and "J" = 10.

When permeability in column "I" of the LGR that contains the well was set to a constant number for all layers, then fracture conductivity became ten multiplied by that constant permeability value. The width of the fracture was constant for all wells and it was previously set to 10 ft. For example, if fracture permeability was 1, then the fracture conductivity was (10 x 1 = 10) md-ft.

Evaluation of Production Data to Determine Fracture Properties

During the meeting with Devon,[19] we were advised that the typical effective fracture half-length in the study area was between 100 and 350 feet.

In order to provide initial fracture properties for the model, available production data was analyzed using ECRIN.[20] A single-well model with finite conductivity fracture was applied with the assumption of bilinear flow. The resulting values were independent of the geology of the reservoir (see Table 8).

Table 8: Fracture Properties from ECRIN

Well	Kh, md-ft	X_f, ft	F_{cd}, md-ft	R_e, ft	STGIP, bcf
20894	0.679	450	50	718	5.38
20946	0.561	450	18	676	6.6
20947	4.8	500	1	951	6
21162	0.55	573	40	973	4
21284	1.8	200	1	296	11.8
21338	1.5	300	4.5	986	8
21391	1.66	300	0.7	735	3.5
21435	2	360	0.5	675	2.6
21688	1.4	500	10	1010	3.5
22224	0.28	125	2	387	0.85
22447	4	125	0.7	737	1.7
21366	0.18	380	1	414	1.6

Figures 45 and 46 show typical analysis for wells 21435 and 21391:

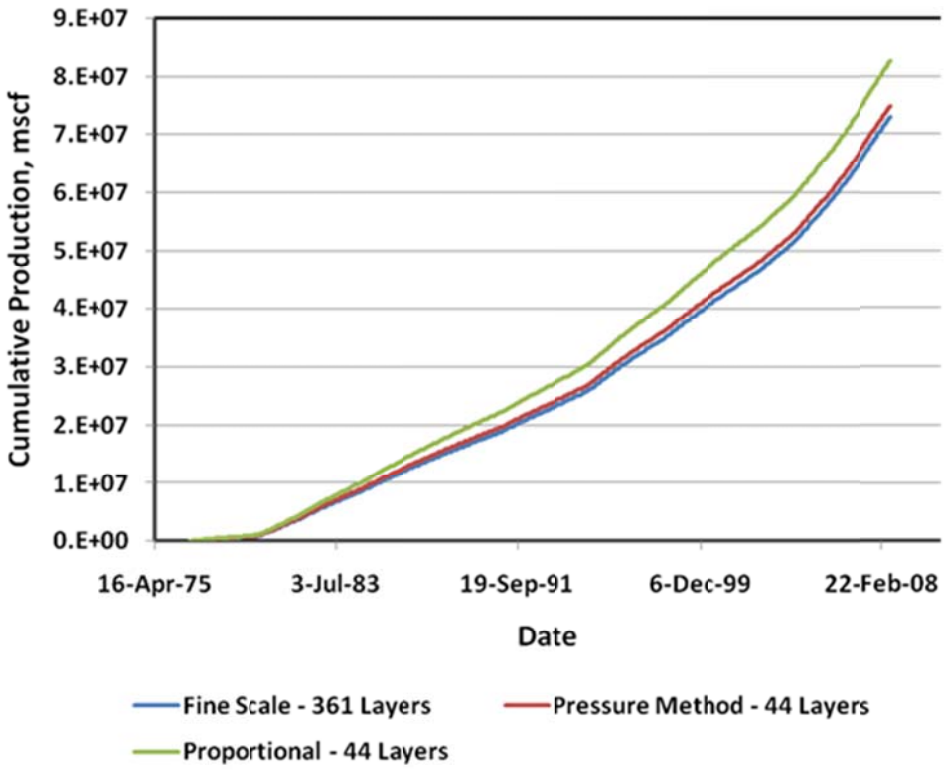

Figure 45: Well 21435 Production Data Analysis in ECRIN

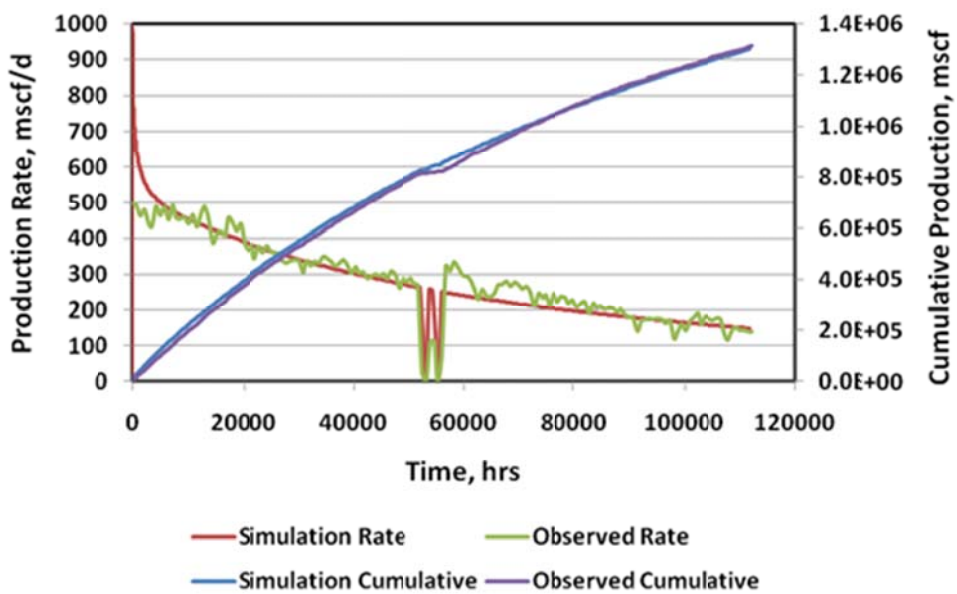

Figure 46: Well 21391 Production Data Analysis in ECRIN

Dynamic Properties

Originally, the simulation deck was built according to the Eclipse Manual instructions. It was comprised of separate text files: the main data file, the "include" file with geometry and

petrophysical properties of the reservoir, the Special Core Analysis (SCAL), and the summary and schedule.[21]

When 64-bit PETREL became available, it became possible to run simulations from PETREL. In other words, all the text data files were being stored and initialized in PETREL, but the actual simulation was run by ECLIPSE. It was more convenient than exporting the static model every time we made changes to it. If the model has to be simulated on any other machine in the future, it can be exported as an ECLIPSE format simulation deck.

No abnormal reservoir pressures and no faults were reported; therefore, the reservoir had only one region segment. The model was initialized with pressure gradient and initial water saturation. Pressure was calculated as 4,590 psi at 8,500 feet. However, PETREL uses sub-sea depth rather vertical depth from the ground. As a result, the reference depth was set to -1,873 ft. for 4,590 psi reservoir pressure. The gas-water contact depth was set at 20,000 ft. because there was no aquifer zone below Almond with pressure support.

Initial water saturation was derived from the cross-plot of Porosity versus Water Saturation. The idea was that higher porosity yields higher gas saturation. The obtained water saturation value was 15%. Figures 47-50 show the cross-plots for four zones.

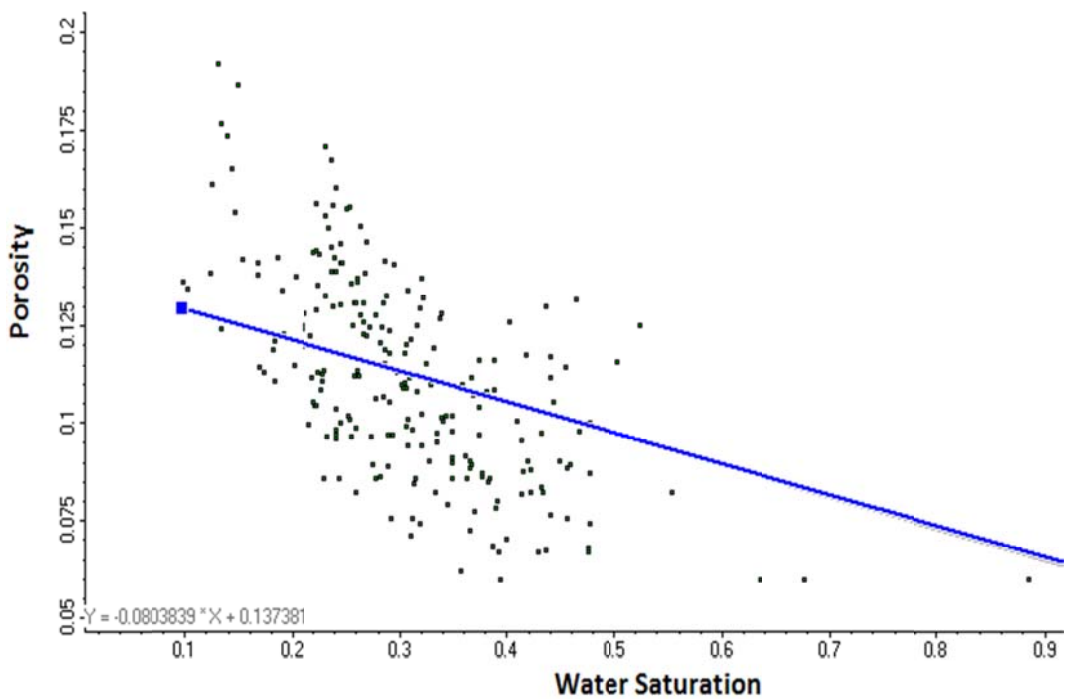

Figure 47: Porosity and Water Saturation Correlation for the Almond Bar

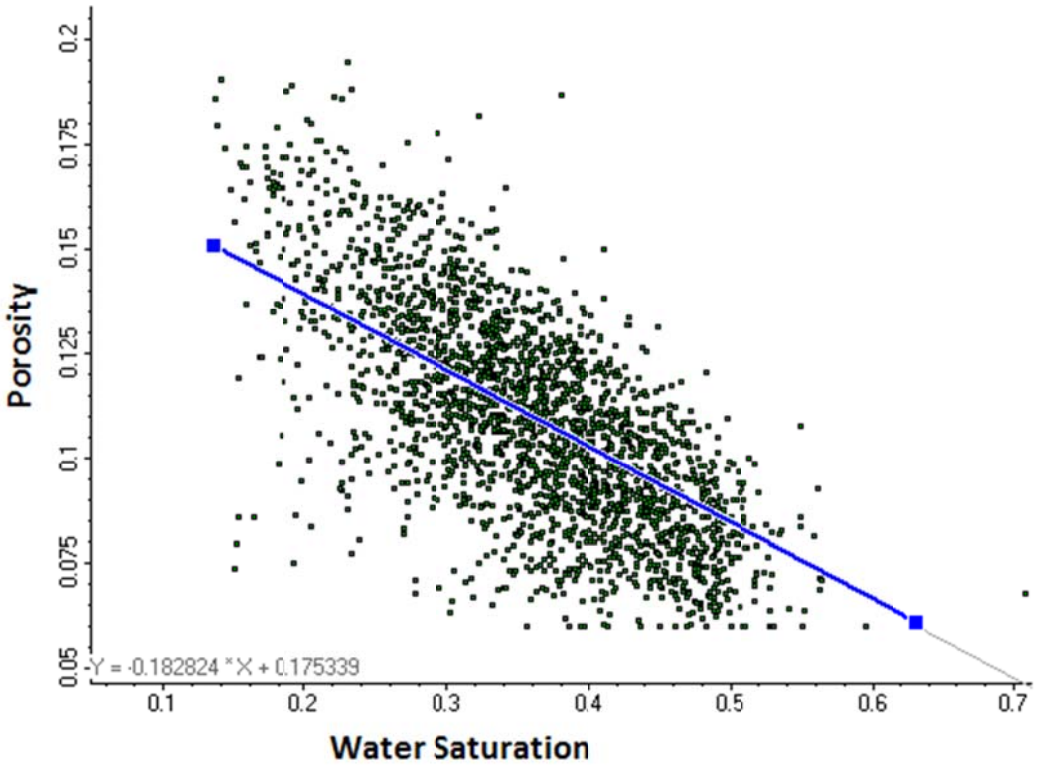

Figure 48: Porosity and Water Saturation Correlation for the Upper Almond

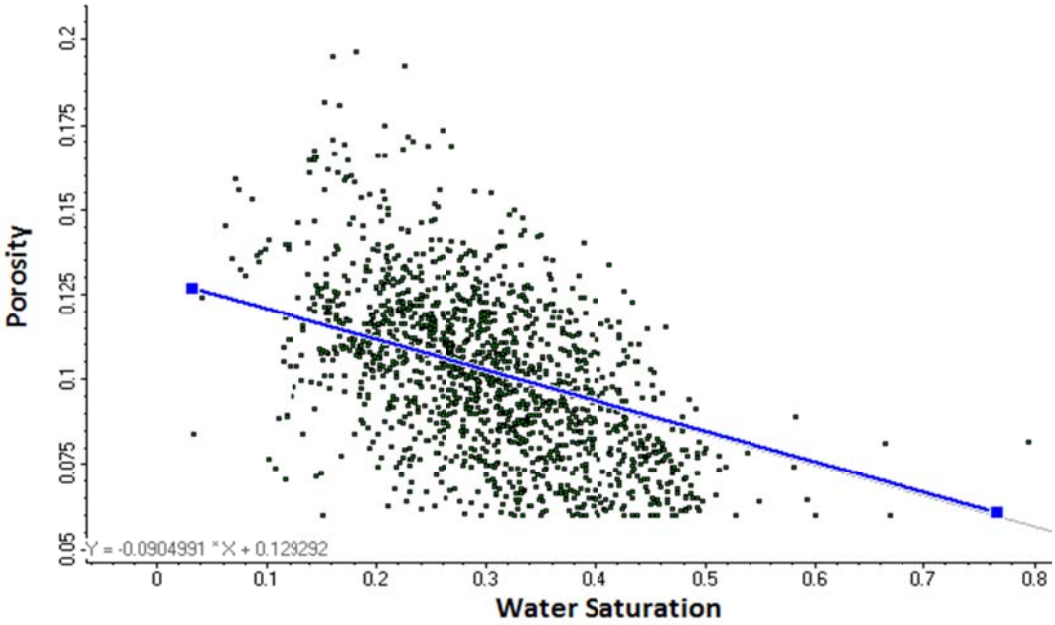

Figure 49: Porosity and Water Saturation Correlation for the Middle Almond

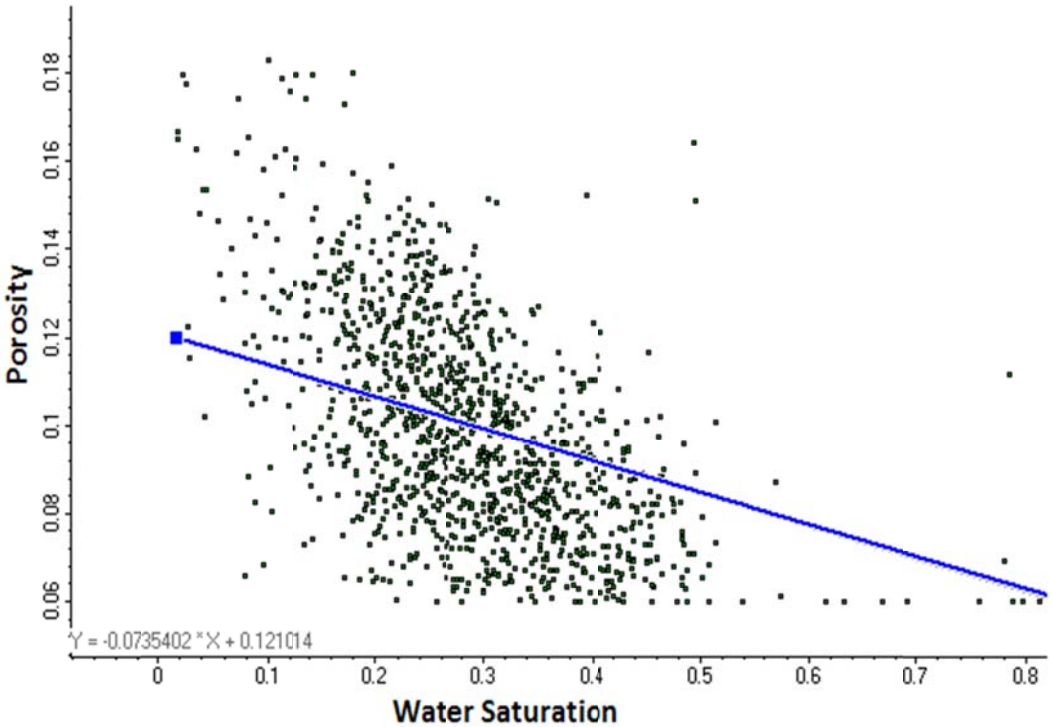

Figure 50: Porosity and Water Saturation Correlation for the Middle Almond

The reservoir does produce water; however, detailed information about relative permeability related to each rock type was not available. Hence, the model was simplified by assuming immobile water. In order to make water immobile, the following relative permeability curves shown in Figure 51 for gas and water were assumed. The change in the productivity of the well due to liquid accumulation near the wellbore was by adjusting the skin factor.

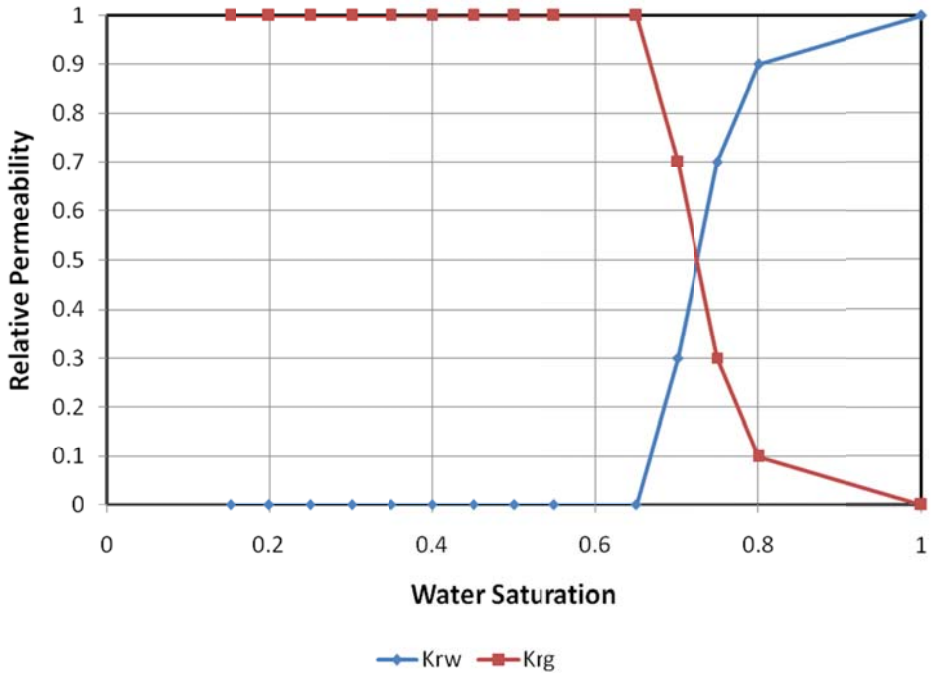

Figure 51: Relative Permeability Curves

The schedule file was created using the Development Strategy feature of PETREL RE. A starting date for every well was set as the first day of the first month of production. Production was reported every month. For instance, if the well started producing in January, its starting date in the model would be January 1 and production was reported on the first day of February.

After 2001, pressure was provided as wellhead readings at tubing and casing. Since prior pressure data was not available, the decision was made to use constant bottom hole pressure as the production constraint. Flowing bottom hole pressures were calculated using Gray's correlation for multiphase flow.[10] The average value of 370 psi was set as a constant bottom hole pressure.

Every well was set to be perforated from the top layer of the Bar to the bottom of the Lower Almond. The effective *kh* values were calculated from the grid data. Skin factor was set to zero. The perforation date for each well was set to the same date production started in the Development Strategy for that well.

Provided completion records indicate that 10 wells were completed and started producing in the 1960's and 70's, but available production history doesn't start until January 1980. When the simulation run was started in 1980, it resulted in much higher production from those earlier wells. Their reservoir pressures were not at the initial level in 1980. So the decision was made to start those wells on their actual starting dates before the reported production; therefore, the simulation model started in July 1963.

We did not include facies property in the coarse model simulation. ECLIPSE identifies inactive grid blocks by zero Net-to-Gross, zero porosity, or a minimum pore volume. Upscaling of facies could combine shale and sand and assign shale as being most of the coarse cell, while porosity might result in a non-zero value. So including upscaled facies property in the simulation reduces number of

cells and reduces the pore volume. On the other hand, shale grid blocks in the model have a zero porosity and ECLIPSE will automatically treat them as inactive blocks.

History Matching

It was necessary to prove the accuracy of the model by matching the simulated and historical productions. The last production date was reported as April 2010; therefore, any further simulation results were considered as predictions. Most of the wells, especially the early ones, had very scattered monthly production rates. Hence, the comparison of cumulative production plots was more representative than comparison of monthly rate plots.

In order to match the history, initial fracture half-length (X_f) and conductivity (F_{cd}) were modified. In the beginning, most of the wells had 125 ft. fracture half-length and conductivity of 1 md-ft. After each run, individual well fracture properties were manually adjusted to match the observed production. The process was repeated until a good match was achieved for the field and for individual wells. Figures 52 and 53 show the cumulative production match and monthly rate match respectively. As shown, the match is good until 2004, but then the two curves diverge as the observed production rapidly decreases.

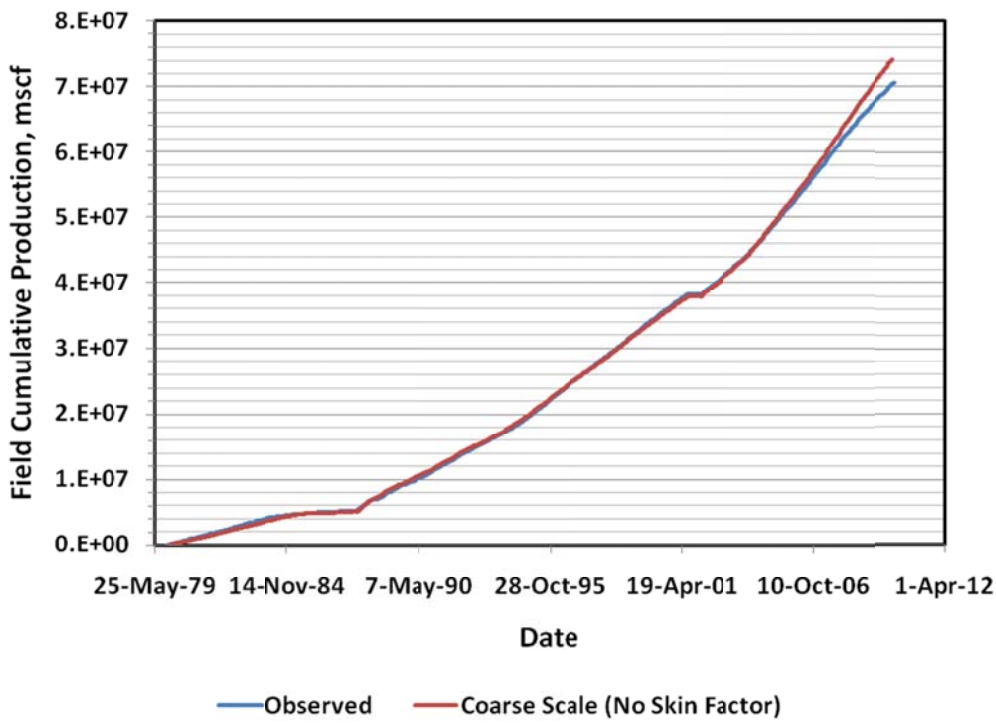

Figure 52: Field Cumulative Production Match

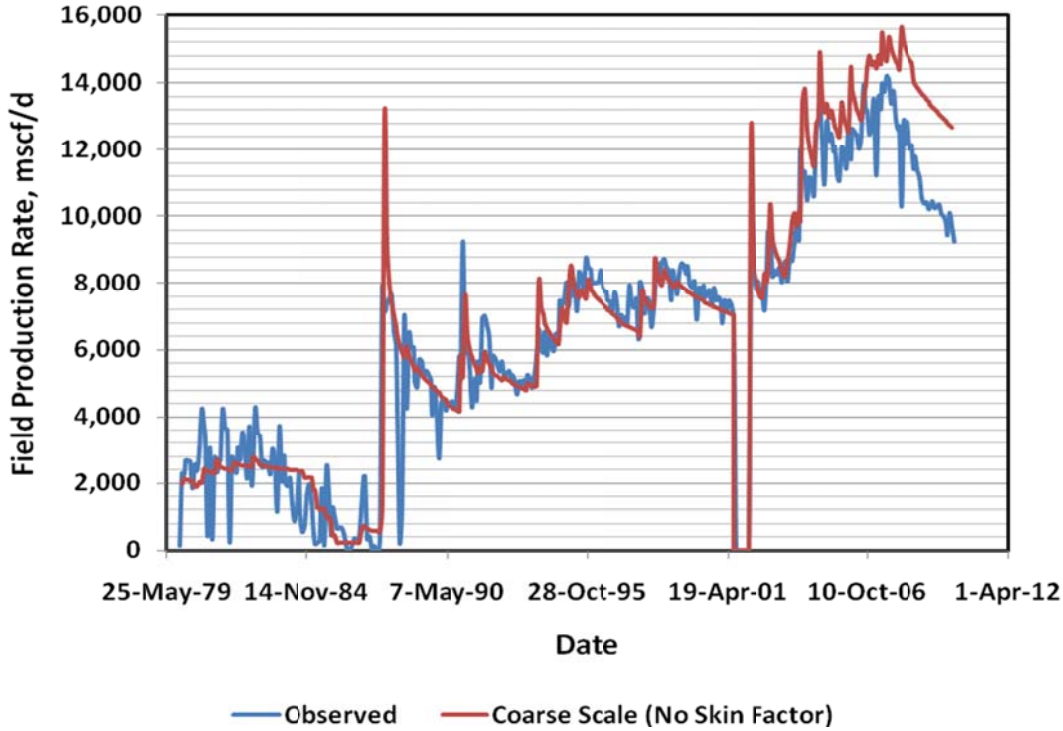

Figure 53: Field Production Rate Match

In order to account for uncertainty, the effect of different variogram ranges was investigated. For instance, the original facies variogram range of the Upper Almond was divided in half, the Middle Almond range was doubled, or the combination of the two was used. Many different combinations of variograms were simulated; however, field production rates could not be matched. Figures 54 and 55 show the global match results for field cumulative and daily productions for the case when the facies variogram in Upper Almond was doubled. This indicates that initial variogram models were very reasonable and provided a reasonable interpretation of spatial relationships.

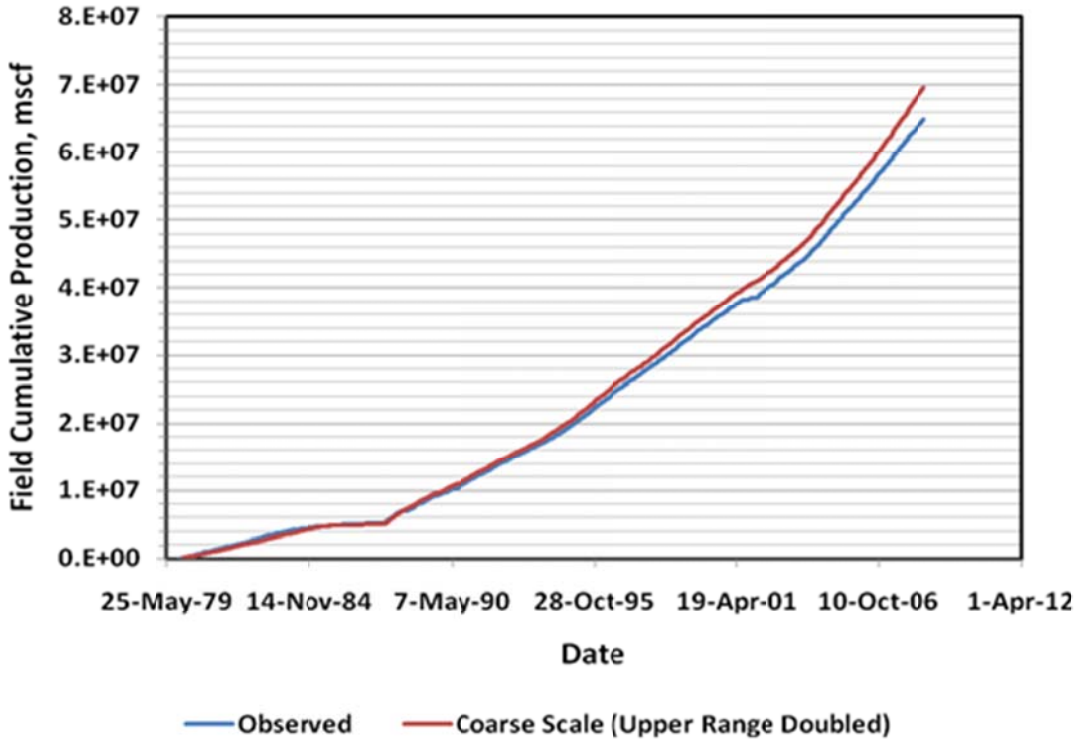

Figure 54: Field Cumulative Production - Upper Almond Range Doubled

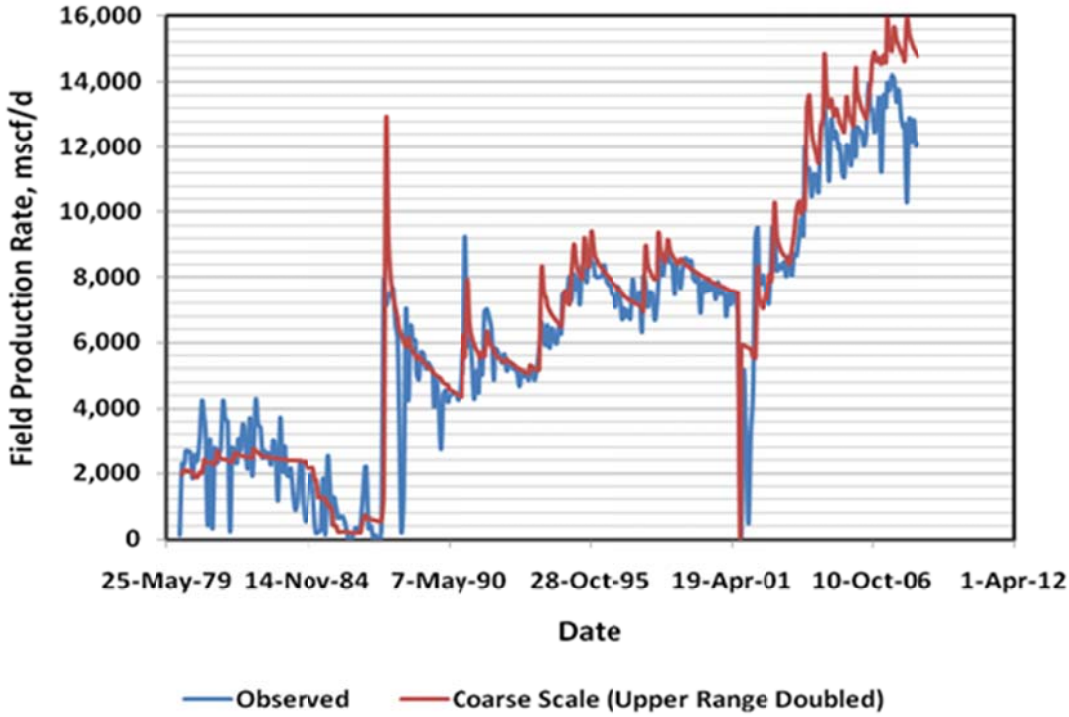

Figure 55: Field Production - Upper Almond Range Doubled

Reported production showed that there were many wells with liquid loading issues. Liquid loading is the process of liquid accumulation at the bottom of the well due to the inability of gas to lift the

associated liquid. It creates a hydrostatic column of liquid reducing permeability to the gas and can potentially kill the well if the liquid is not removed. Several indicators were investigated to check for the existence of liquid loading. These included erratic production and pressure profiles, rapid rate decrease, divergence of casing and tubing head pressures and Turner Velocity.[22, 23] Each well was analyzed for a combination of those factors.

A high degree of scatter in production rates and pressures indicates unstable slug-type flow in the well or unstable operating conditions. A sharp drop in a production rate curve is indicative of liquid loading, since liquid accumulation creates back pressure and damages the formation. A liquid column in the tubing decreases wellhead pressure, while gas is accumulating in the annulus resulting in higher casing pressure readings. Turner, *et al.*[22] introduced critical velocity as a minimum gas velocity required to lift liquid droplets. From the available tubing head pressures and rates, we calculated flowing bottom hole pressure (FBHP) with Gray's correlation for multiphase flow.[10] The Turner critical velocity and flow rates were then calculated at wellhead and bottom hole conditions. Figure 56 shows pressure and flow rate relationships for Turner critical flow rate for three nominal tubing sizes used in the field: 2-7/8", 2-3/8" and 2-1/16".

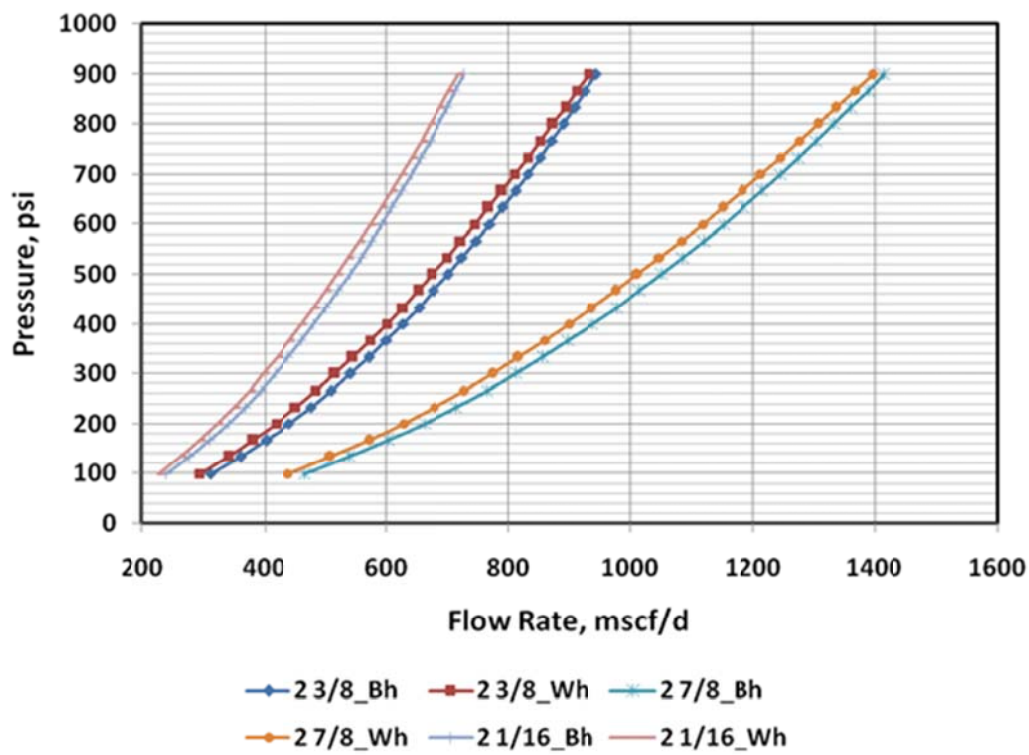

Figure 56: Turner Critical Flow Rate

For the most common tubing size of 2-3/8" and FBHP of 370 psi, Turner's critical velocity was close to 500 mscf/d. Based on input from the operations engineer working for Devon in the Wamsutter field[24], liquid loading starts at approximately 550 mscf/d in the 2-3/8" production tubing string, at which point the field operators initiate plunger lift. Hence, the estimation was reasonably close to the field observation.

Including liquid loading phenomenon into the simulation was necessary because it artificially reduces gas natural flow rate. In other words, the historical production could have been matched to a point where liquid loading started but then the simulation and observed rates would diverge as the observed rate dropped rapidly. Two ways of including liquid loading in the simulation were considered.

The first solution was to increase the flowing bottom hole pressure. A liquid column in the wellbore increases the pressure gradient; however, for tight reservoirs, this does not help reduce the gas rate because the rate is related to (P_r^2-P_{wf}^2). When bottom hole pressure is already low, changing it does not significantly change (P_r^2-P_{wf}^2). This is especially true when $P_r >> P_{wf}$.

The second possible solution was to modify the skin factor. When liquid accumulates in the wellbore, it can imbibe into the formation resulting in skin damage. This can result in reduction in the production rate.

As a result, skin factor was added when liquid loading started. Values differed from well to well were between 1 and 10. The median skin factor was 4.

Figures 57 and 58 show history match results for the field's cumulative production and daily production. The later part of the production, where it is rapidly decreasing, showed a good match compared to the run without consideration of liquid loading. Details of the history matching parameter are provided by Kassenov[25].

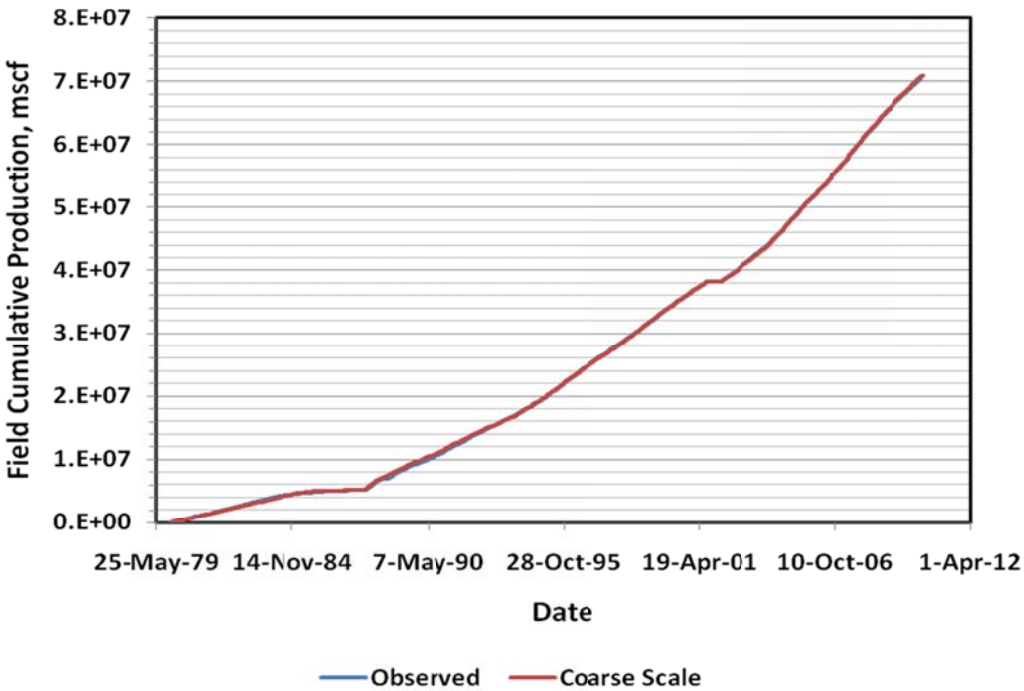

Figure 57: Field Cumulative Production Match

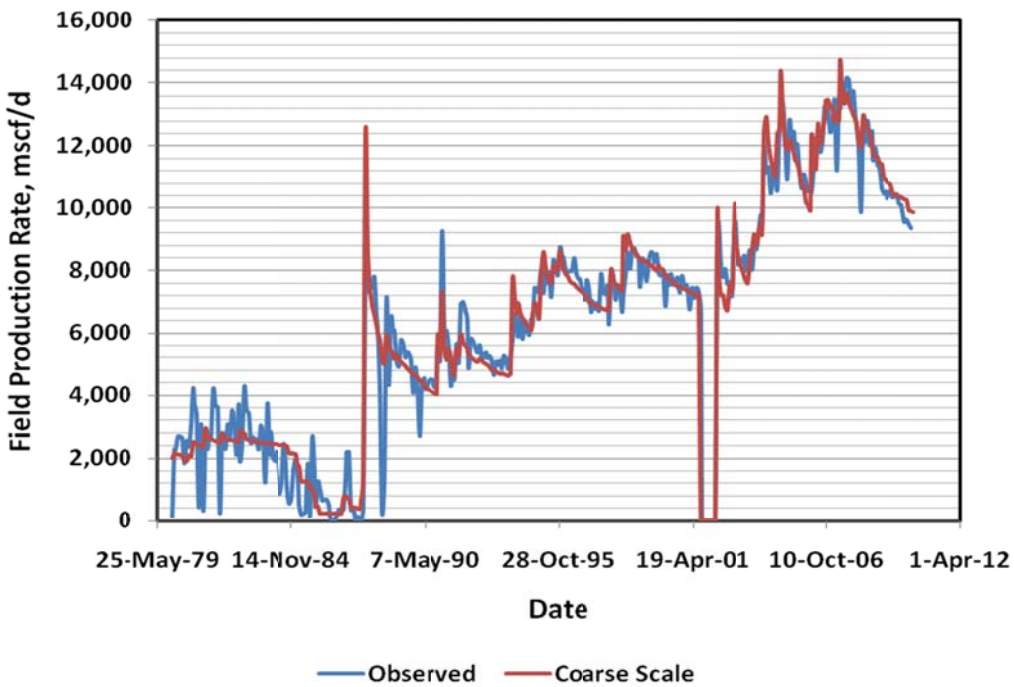

Figure 58: Field Production Rate Match

Wells were also divided into two groups - wells drilled before 2001 and after 2001 - which were named "early wells" and "late wells" respectively. This provided the ability to fine tune the history match. Figures 59 - 62 show history matched field cumulative production and daily production for early and late wells.

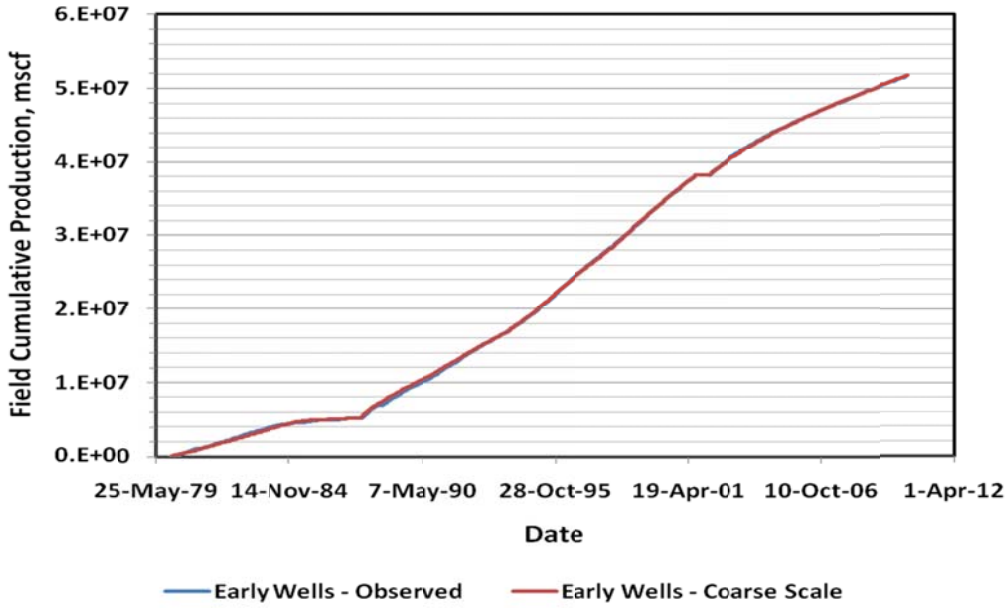

Figure 59: Early Wells – Cumulative Production Match

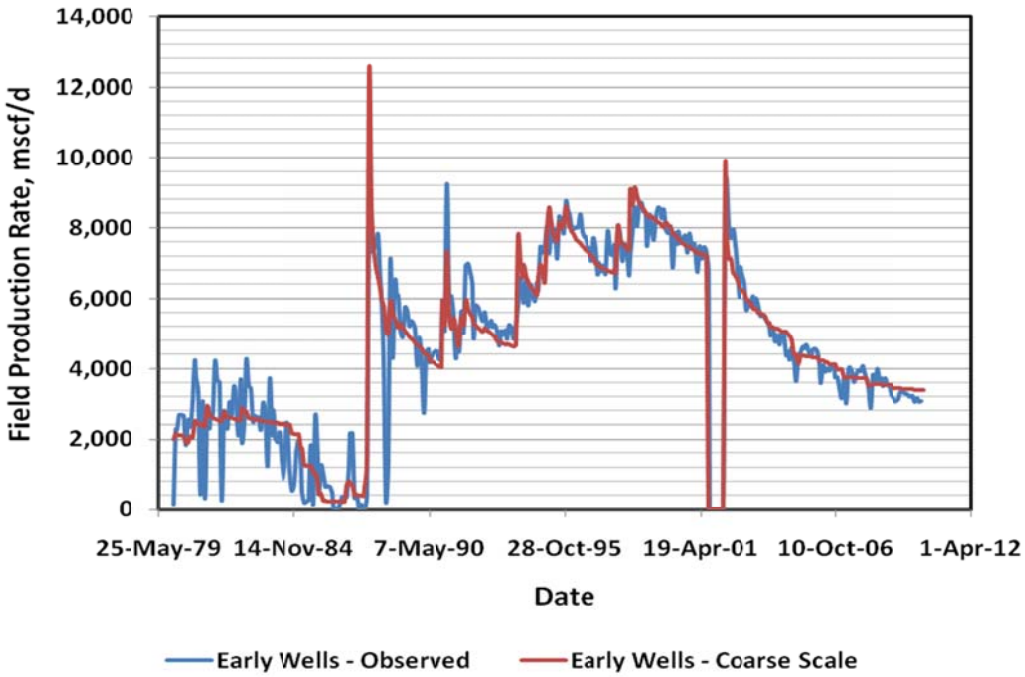

Figure 60: Early Wells – Production Rate Match

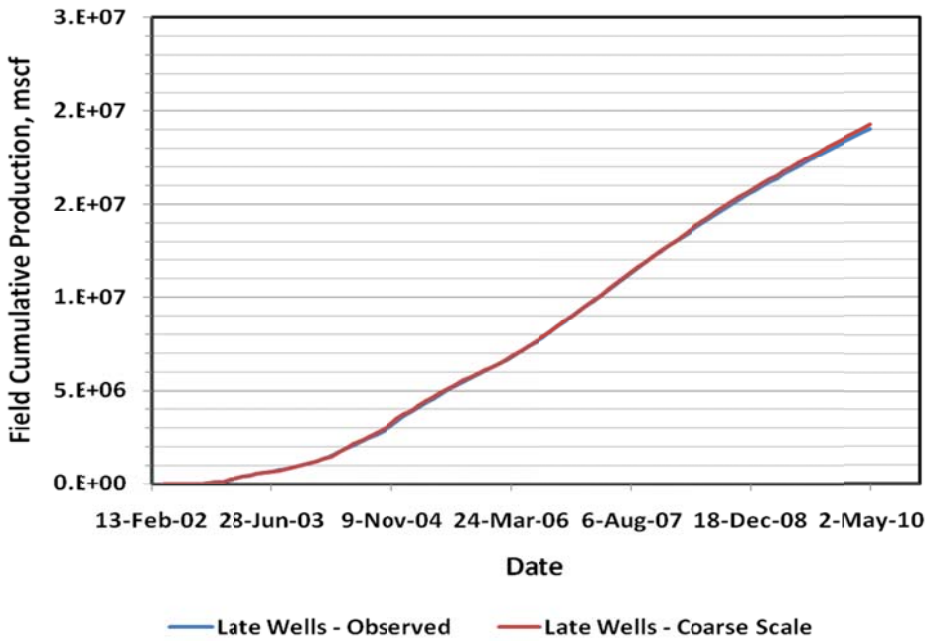

Figure 61: Late Wells – Cumulative Production Match

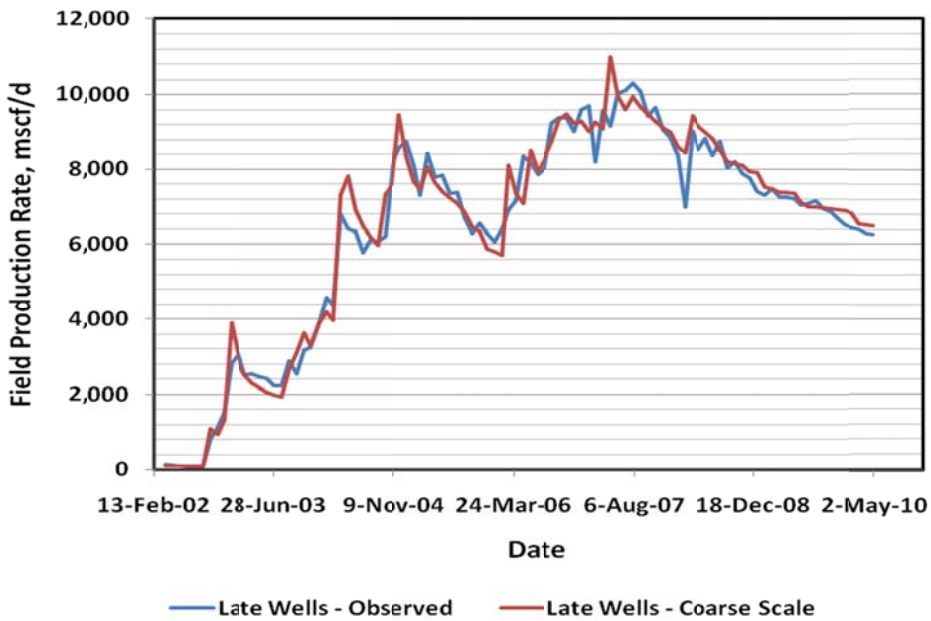

Figure 62: Late Wells – Production Rate Match

Figures 63 and 64 show gas production rate and cumulative production for the well (API number 490072208700). Two other wells where the match is not very good are also included (Figures 65–68).

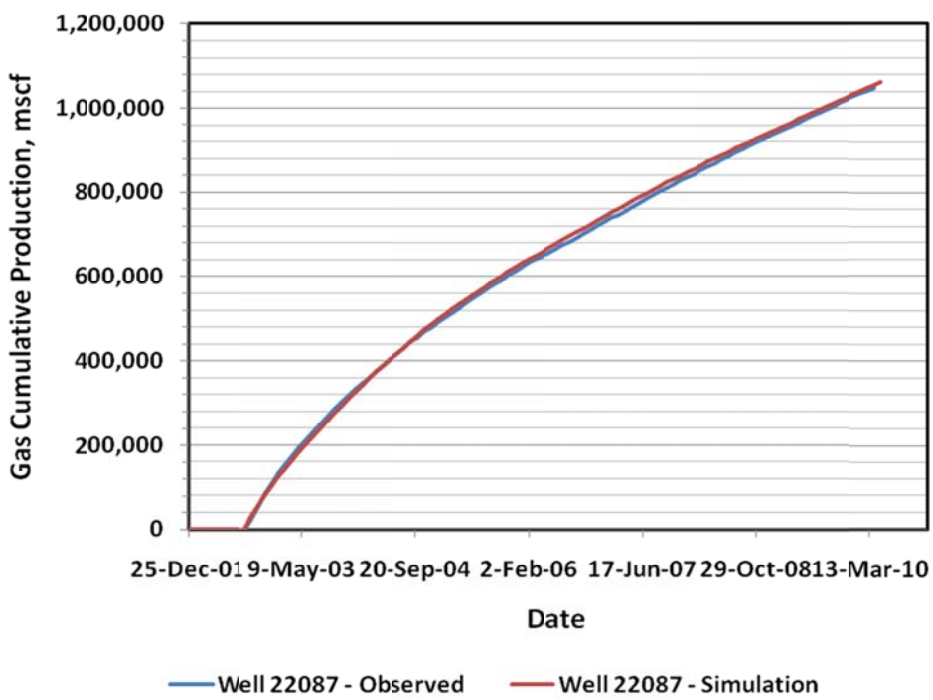

Figure 63: Well 22087 – Cumulative Production Match

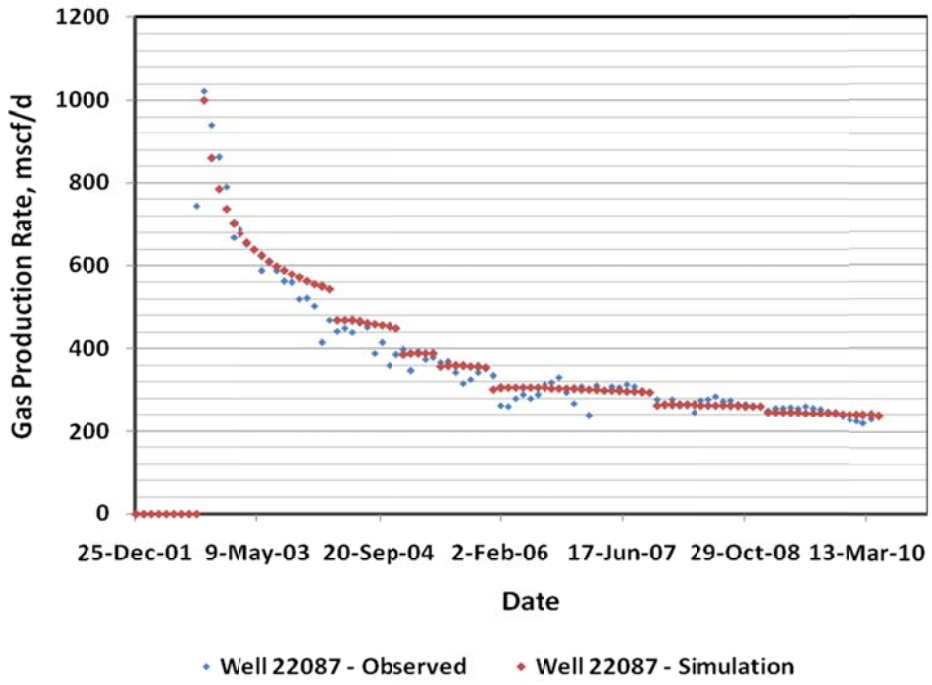

Figure 64: Well 22087 – Production Rate Match

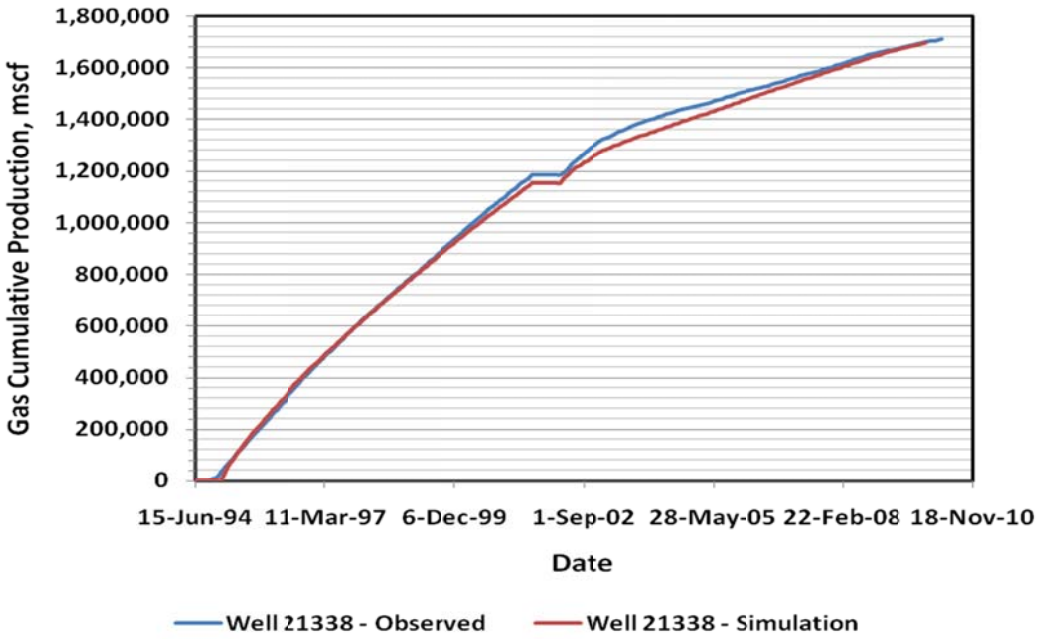

Figure 65: Well 21338 – Cumulative Production Match

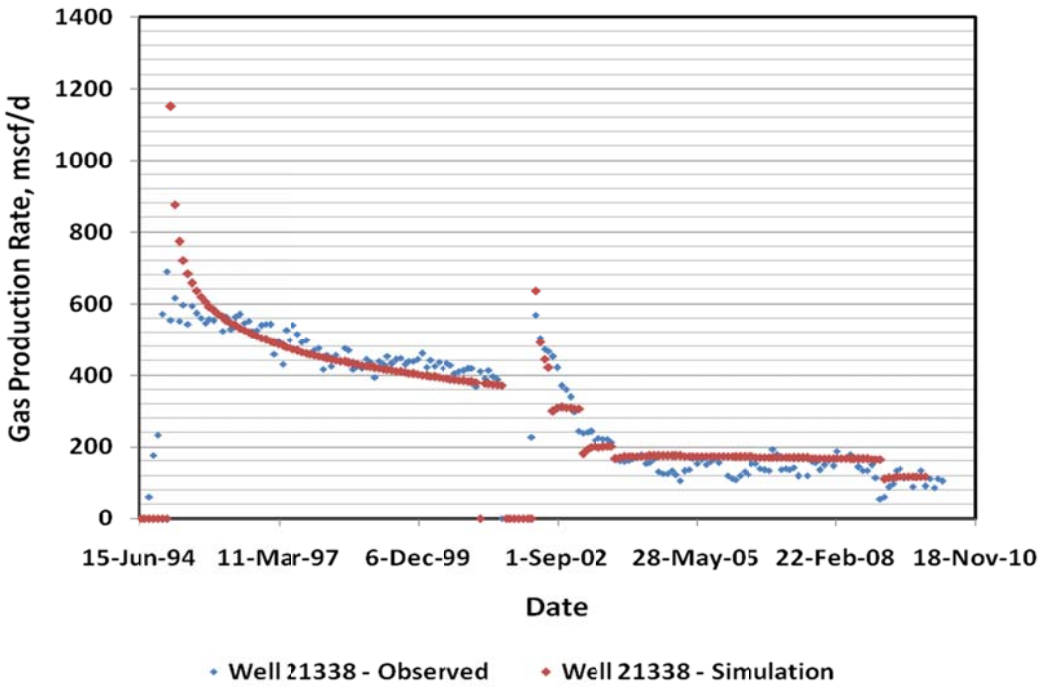

Figure 66: Well 21338 – Production Rate Match

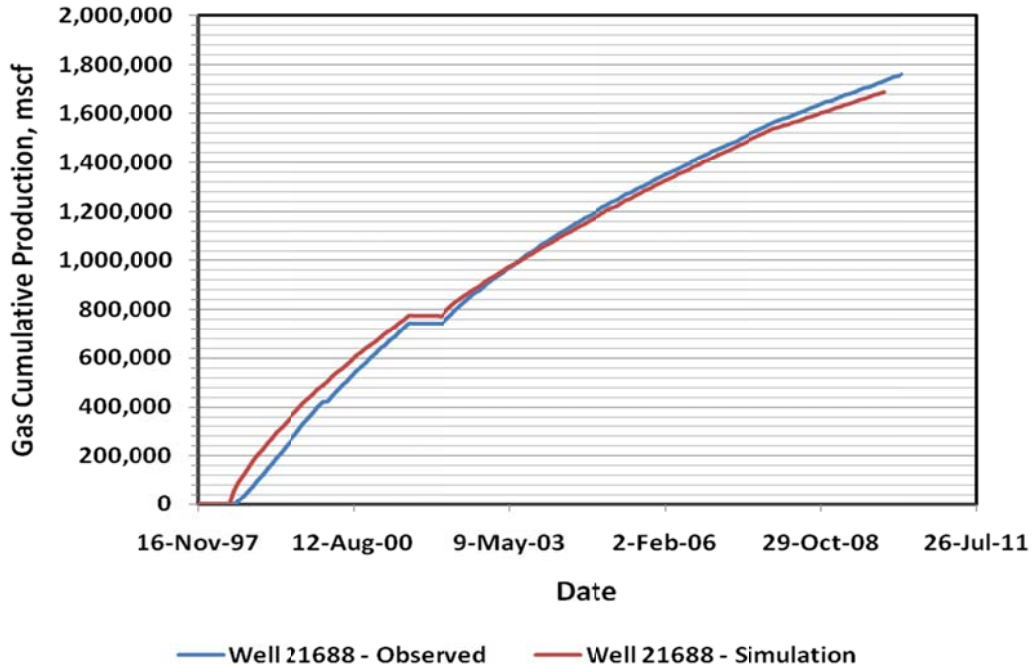

Figure 67: Well 21688 – Cumulative Production Match

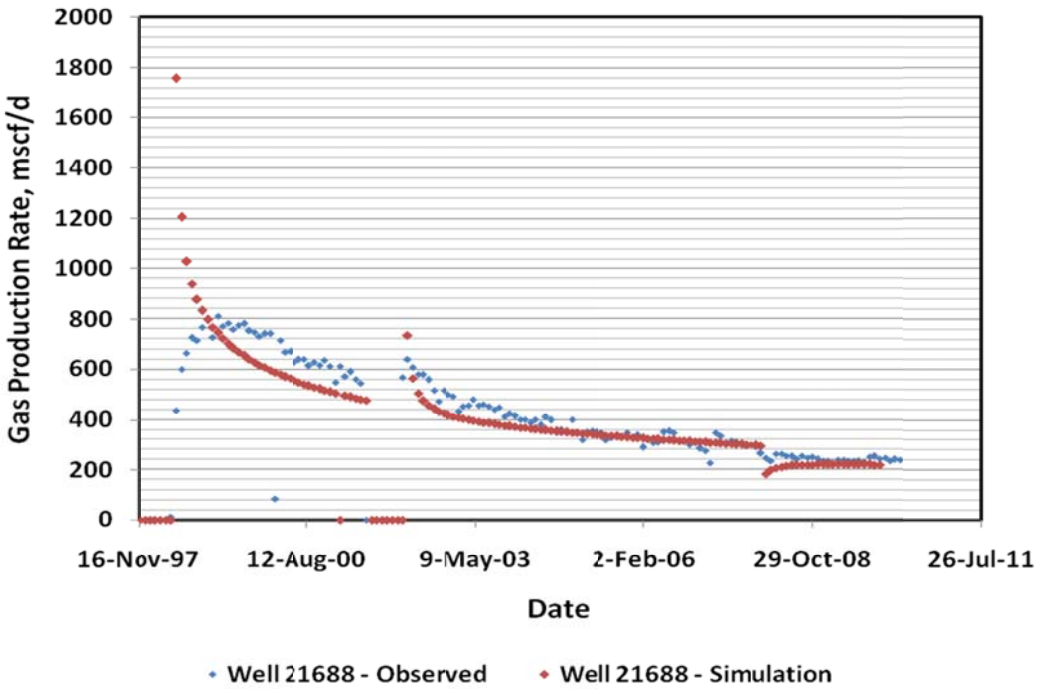

Figure 68: Well 21688 – Production Rate Match

Most wells produce some water. Operators in the study area are dealing with water by installing plunger lift artificial systems. Even though single-phase dry gas production was simulated, high water production indicated that formation water was entering the wellbore. Devon Geologist, Dale Reitz[26], assumes that produced water is a combination of formation water (from the Lower Almond and Ericson in some wells) and water of condensation. However, relative permeability curves from core studies were not available. Figure 69 shows daily wellhead pressures, gas rate, and water-gas-ratio for a typical well.

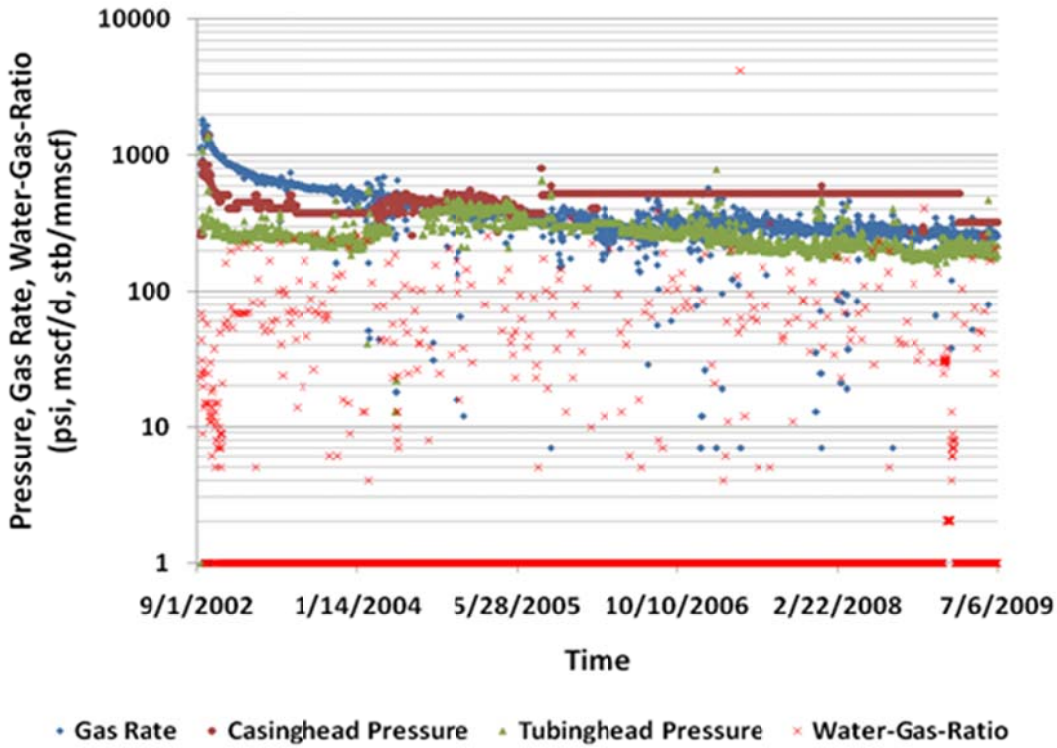

Figure 69: Well 22087 - Daily Wellhead Pressures, Gas Rate and WGR

Once the well is put on plunger lift, the flow becomes discontinuous. The discontinuous production, without detailed knowledge of the plunger cycle, is very difficult to reproduce. As a result, wells in the model were producing continuously and water accumulation in the well was accounted by using skin factor once the liquid started loading.

POST MATCHING ANALYSIS AND PREDICTIONS

Matching parameters were compared with official EUR values provided by Devon Energy. Since both fracture conductivity and half-length have positive relationships with a well's performance, the product of the two values was plotted against EUR. The trend indicates positive relationship (Figure 70).

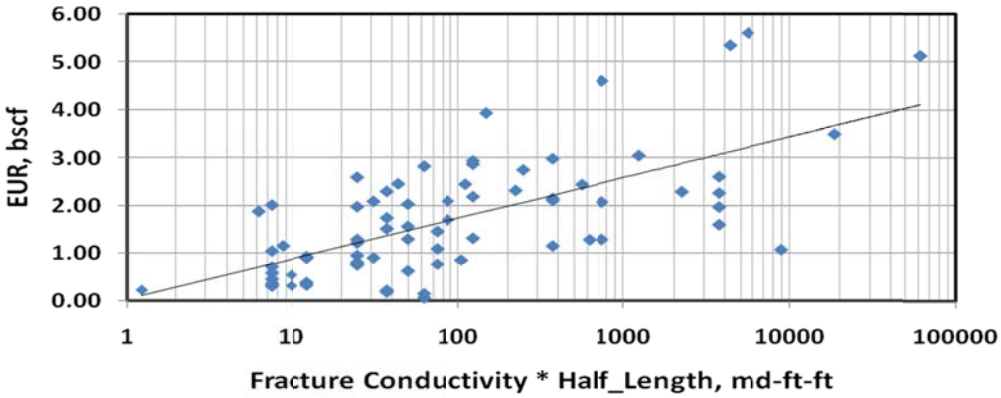

Figure 70: Fracture Conductivity * Half-Length versus EUR

Then, the pore-volume associated with every well within a 725 ft. radius was calculated (Figure 71). The pore-volume for each well was plotted against its EUR. A positive trend was observed.

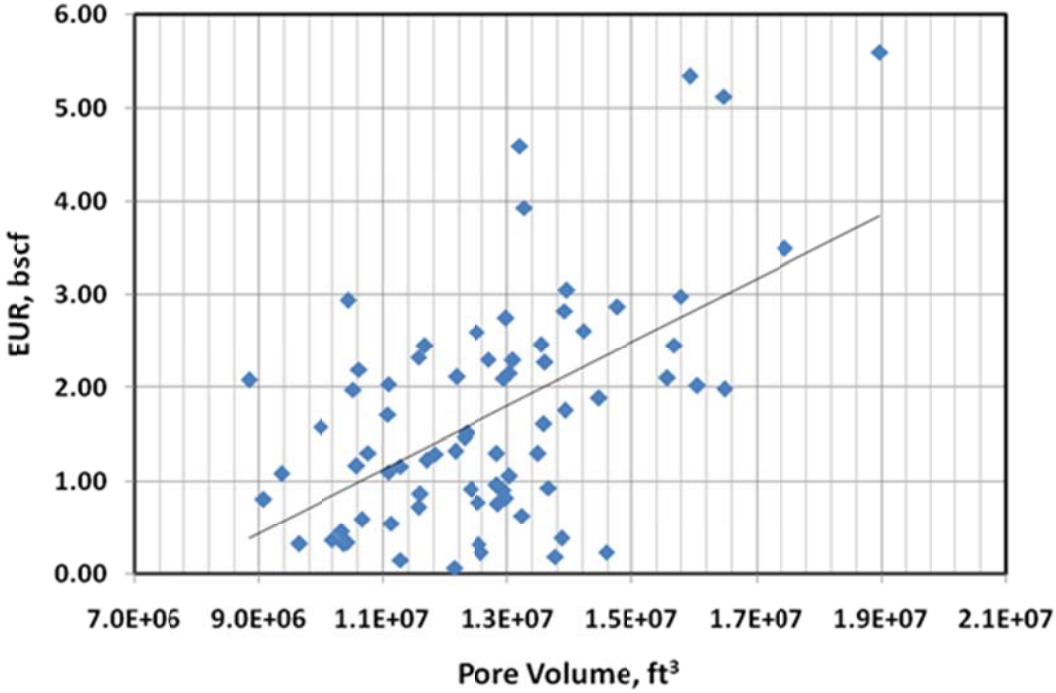

Figure 71: Pore Volume versus EUR

Both graphs show the importance of fracture conductivity and geology on well performance. The wells which produce the best are aided by better fracture and higher gas in-place.

Initial production (IP) was also correlated with ultimate recovery. It was observed that a strong correlation exists between the two (Figure 72). This is typical for tight reservoirs where the connected volume to the wellbore determines both initial production and the ultimate recovery. That is, there is a strong linkage between the connectivity of the fracture to the reservoir and conductivity. The reason for such a strong relationship is the relatively small region which is drained by the fracture in tight reservoirs.

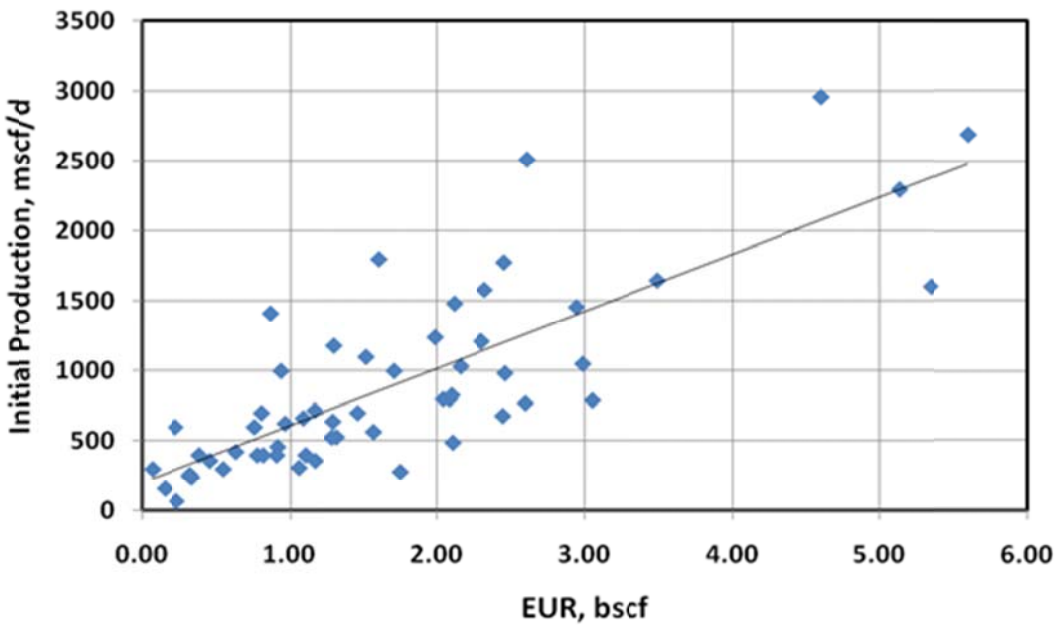

Figure 72: Initial Production versus EUR

As discussed, water production is a big issue in this reservoir. The goal was to determine if the water production rate had an impact on well productivity. Wells were divided according to the WGR (water-gas ratio) and plotted normalized rate (rate/initial rate) against normalized time (all wells start in month one). It was observed that the difference in WGR values has a minimal impact on decline rate (Figure 73). This indicates that even a small amount of water affects the well productivity.

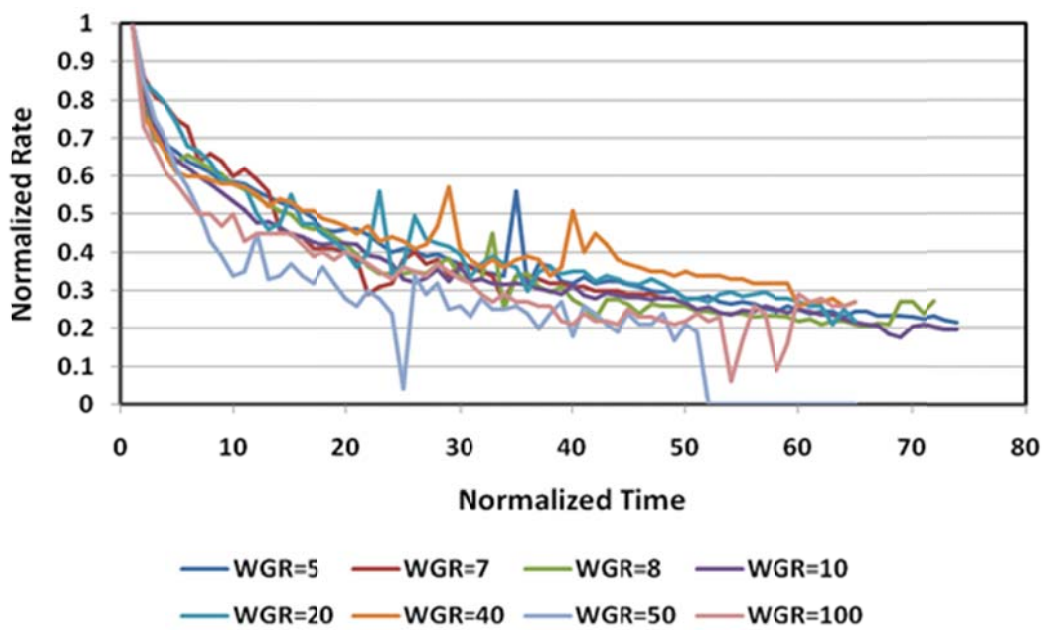

Figure 73: Normalized Rate versus Normalized Time

Another graph was made to compare fracture conductivity and pore-volume with EUR (Figure 74). It does not appear that fracture conductivity is affected by pore-volume which may be an indication of geology. That is, the rock type does not influence the efficiency of the fracture.

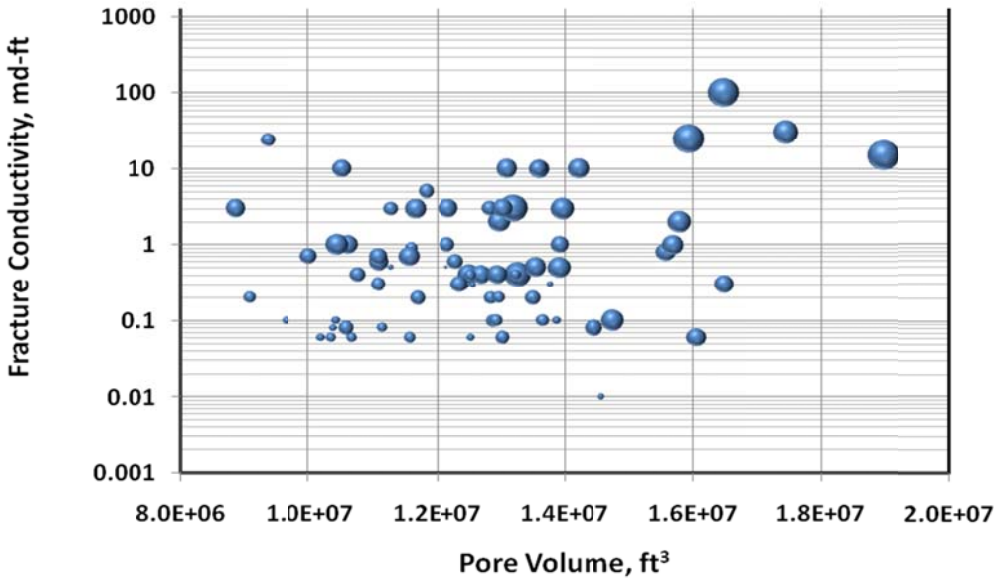

Figure 74: Fracture Conductivity and Pore-Volume versus EUR

As previously mentioned, Devon drilled seven wells from two pads in two sections. The location of the seven wells is shown in Figure 75.

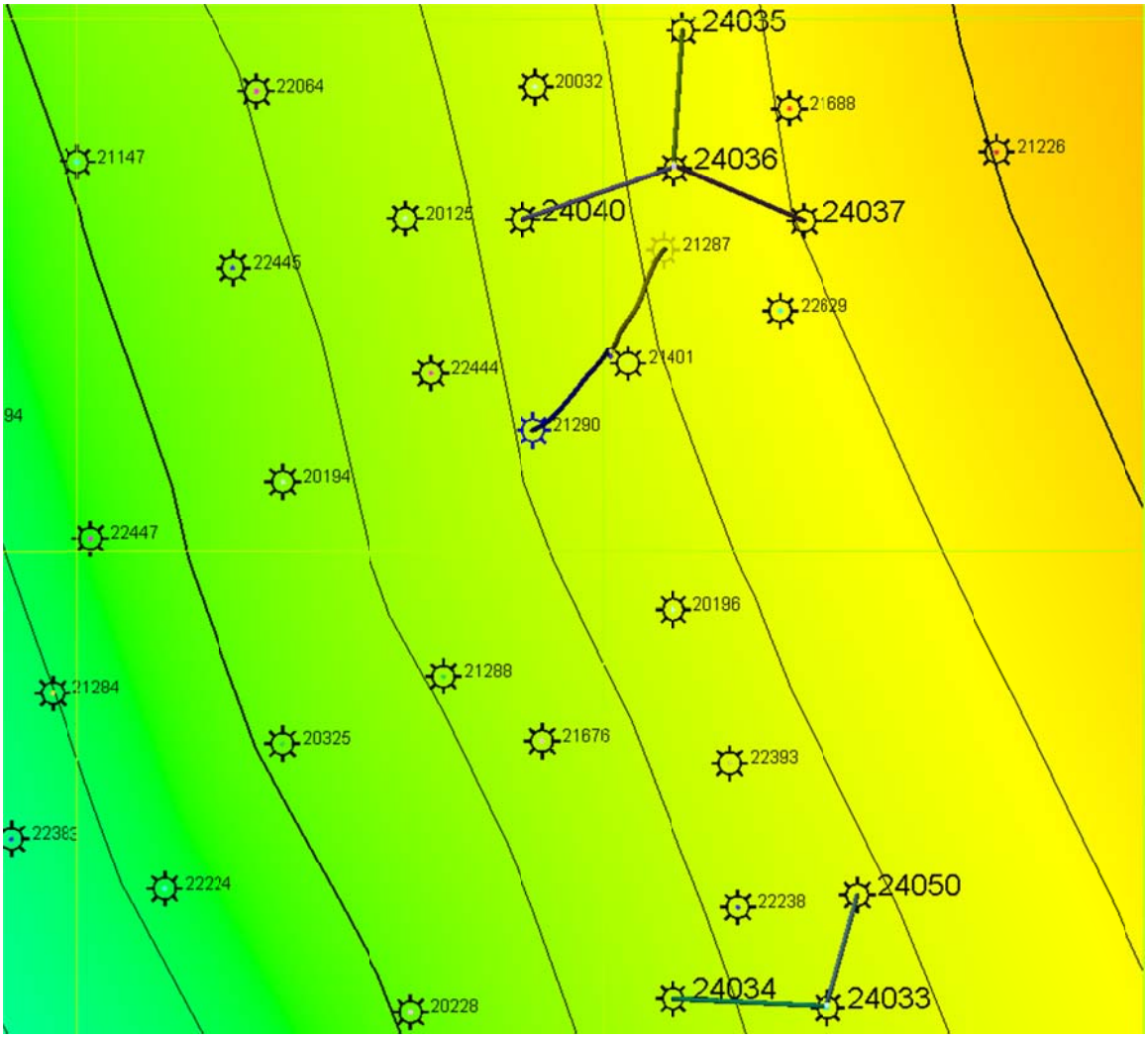

Figure 75: Seven Well Locations

We predicted the performance of these wells by assuming 125 ft. was used for half-length. Conductivity of fractures is a big uncertainty. We assumed values based on the past five years of data.

Net sand thickness was calculated from the fine-scale facies property at the locations of the seven new wells. The units in Table 9 are in feet.

Table 9: Net Sand Thickness in Future Wells

Net Sand Thickness, ft					
Well	Bar Sand	Upper	Middle	Lower	Total
24033	15	54	19	22	110
24034	21	30	39	40	130
24050	2	35	45	34	116
24035	15	37	19	47	118
24036	8	42	31	21	102
24037	7	51	23	42	123
24040	2	40	58	25	125

Figures 76-82 show the predicted future performance of wells with associated uncertainty bounds. The variation in cumulative production is significant.

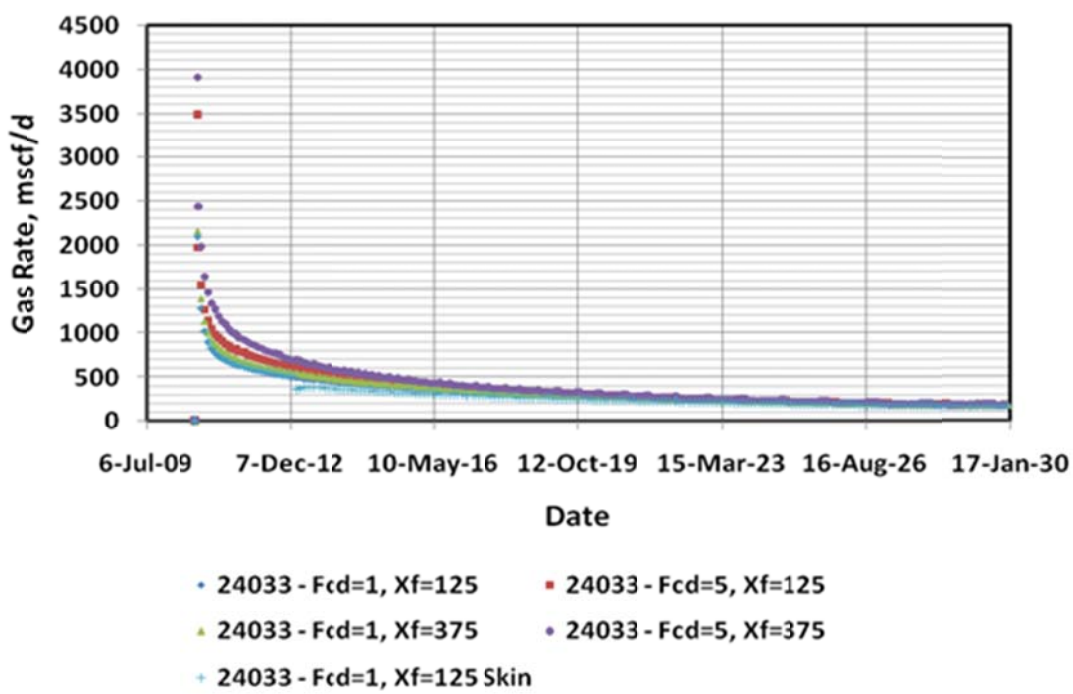

Figure 76: Well 24033 Production Rate

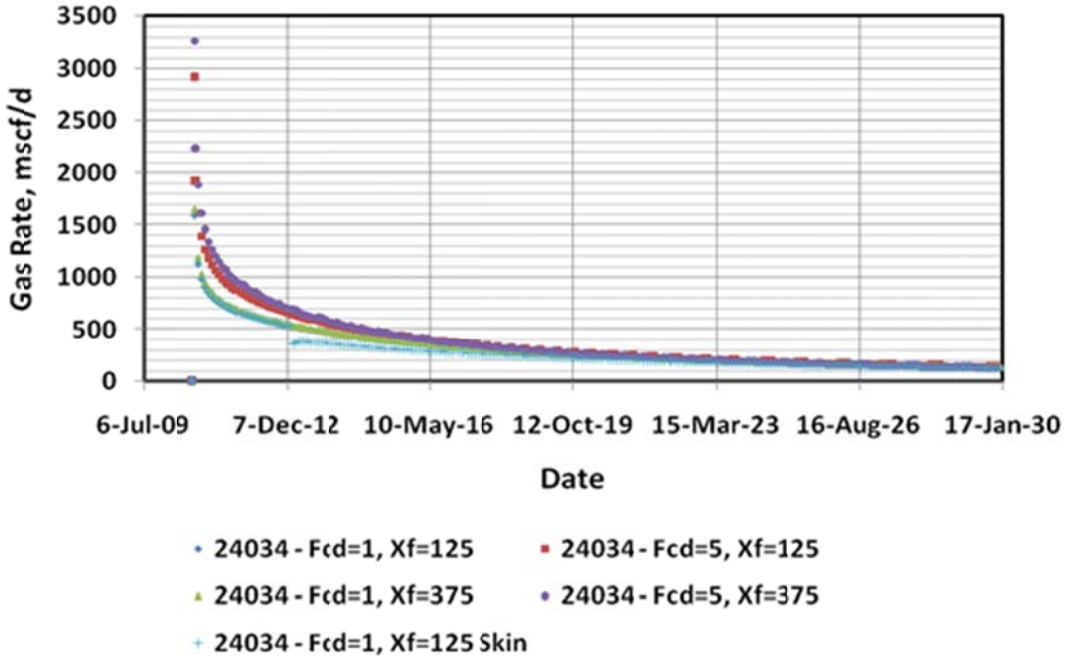

Figure 77: Well 24034 Production Rate

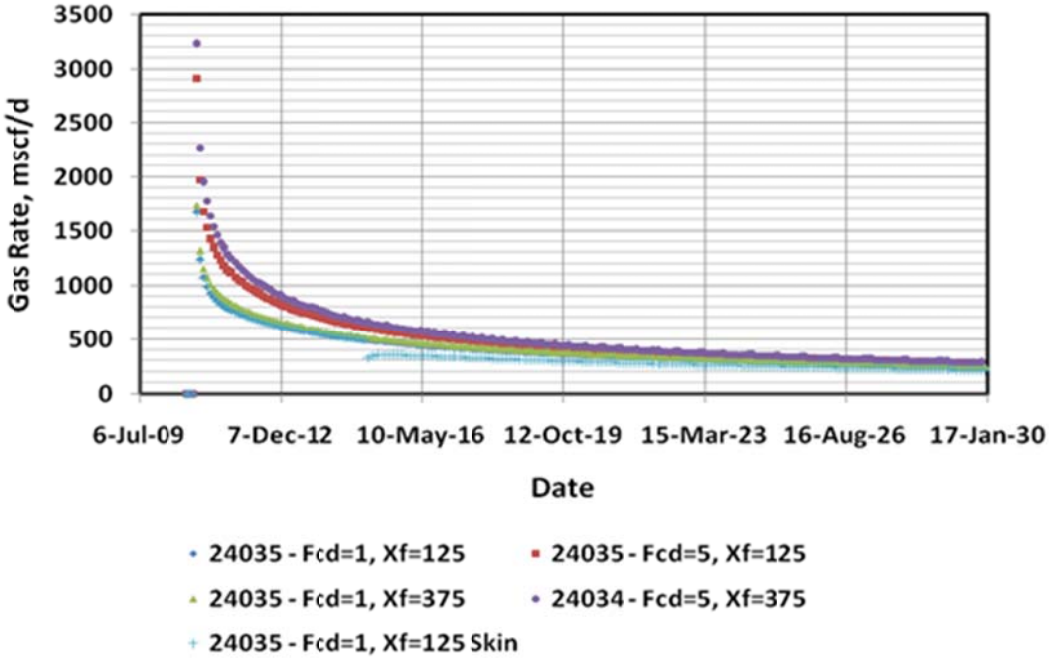

Figure 78: Well 24035 Production Rate

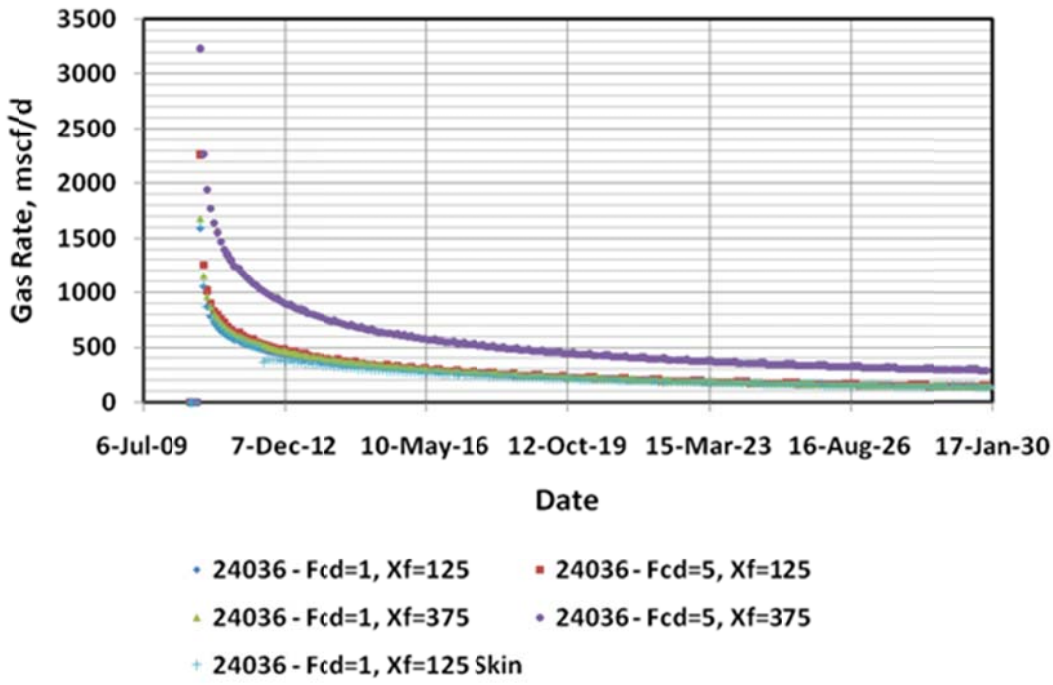

Figure 79: Well 24036 Production Rate

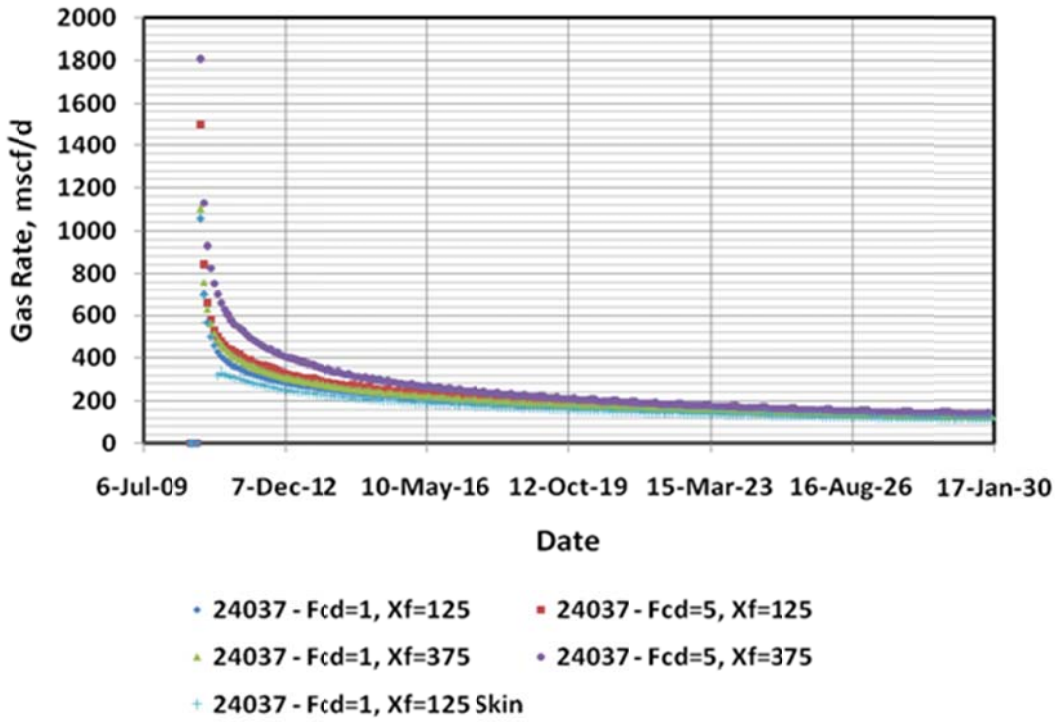

Figure 80: Well 24037 Production Rate

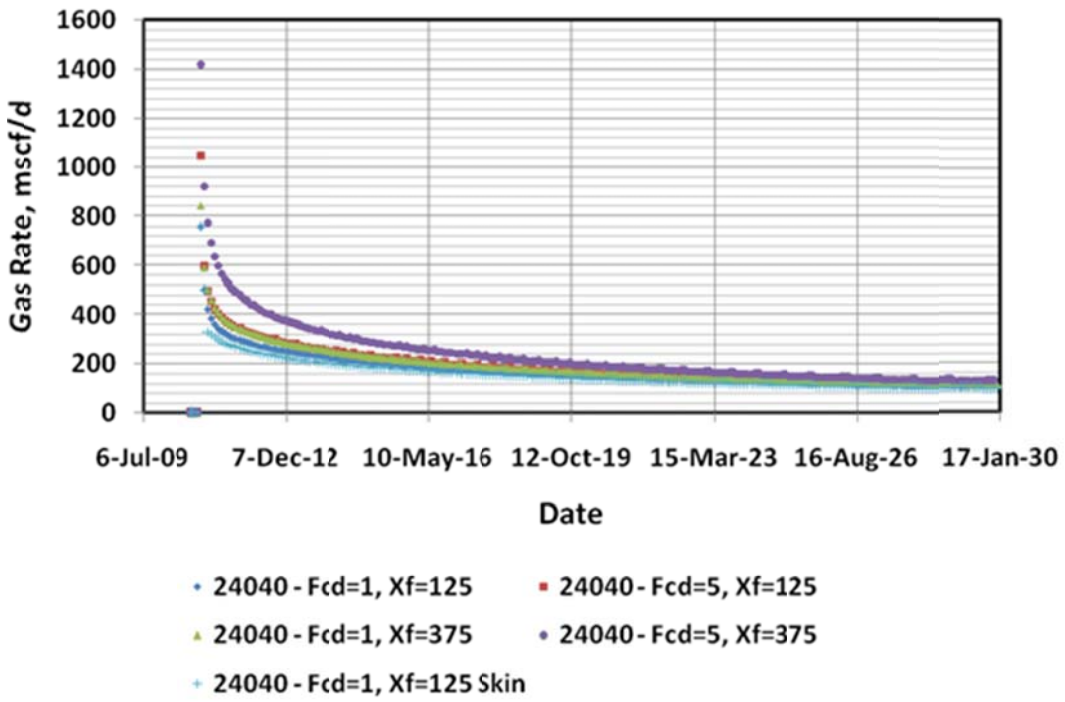

Figure 81: Well 24040 Production Rate

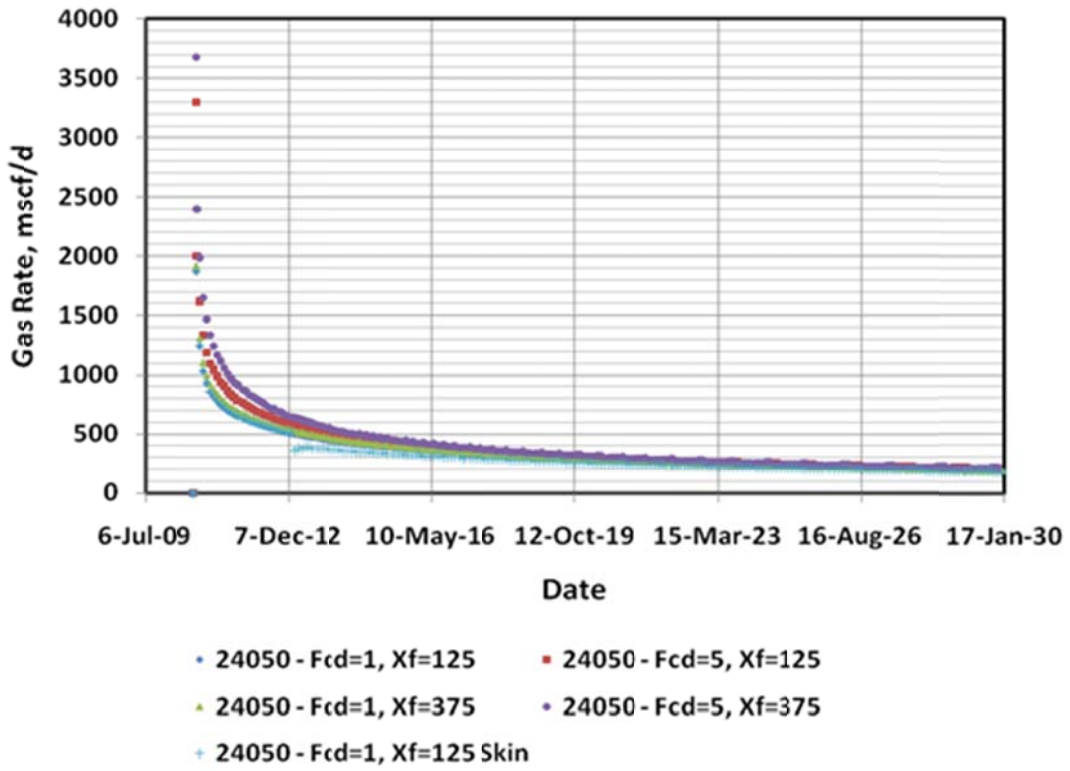

Figure 82: Well 24050 Production Rate

Post-Script

After we made the predictions, we anxiously waited for the results from the seven wells. Devon completed those wells in fall 2010. Of the seven wells, six wells are currently producing. The seventh well is still waiting to be connected to a pipeline. We have some production data, although limited, so that we can compare our results with our predictions. We had to use different values than used in our prediction to match the historical data. Table 10 shows the results.

Table 10: Matched Value of Fracture Conductivity

Well	Xf,ft	Fcd(md-ft)	Skin
#24033	125	0.25	0
#24034	125	0.1	0
#24036	125	0.07	0
#24037	125	0.12	4
#24040	125	0.75	4
#04050	125	0.7	0

The wells are still young and we may need to wait awhile before the final results can be confirmed; however, it is clear that the conductivity is on the low side of what we had originally assumed. We had assumed a value of 1 md-ft. and most wells had values less than that value. Here are some sample matches for wells that were drilled.

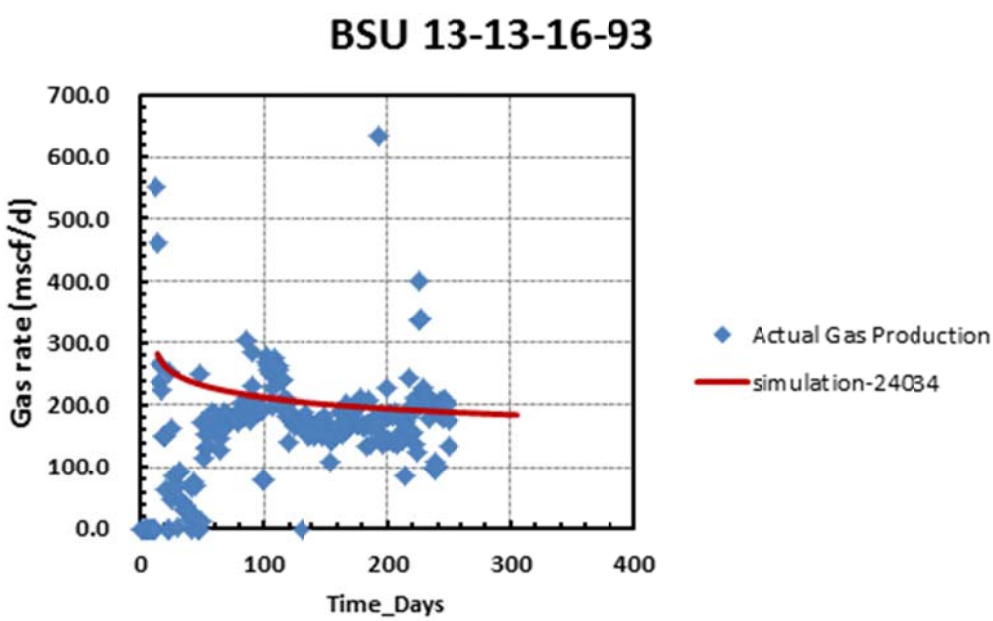

Figure 83: BSU 13-13-16-93 – Match of Historical Data

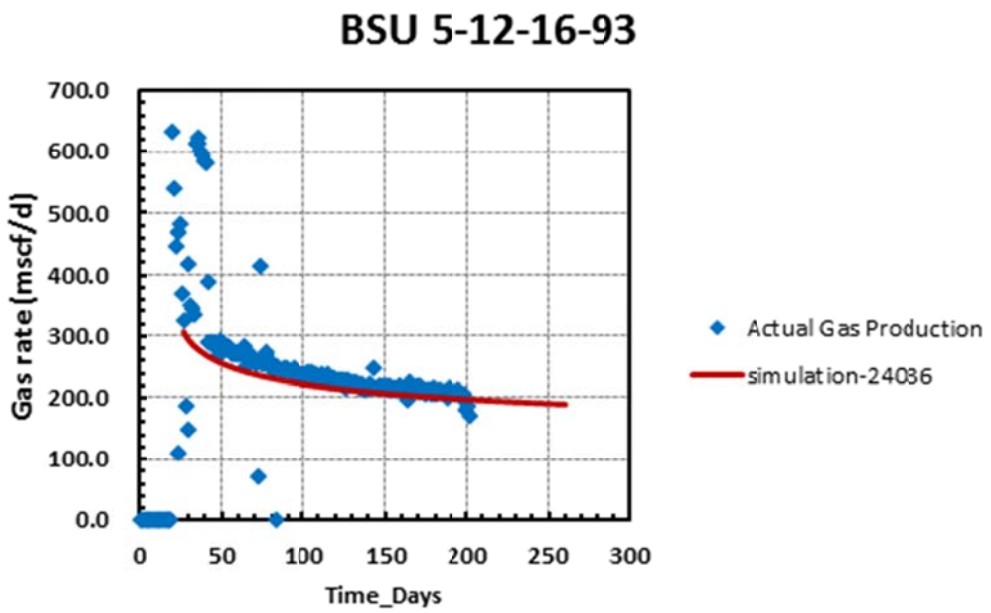

Figure 84: Well BSU 5-12-16-93

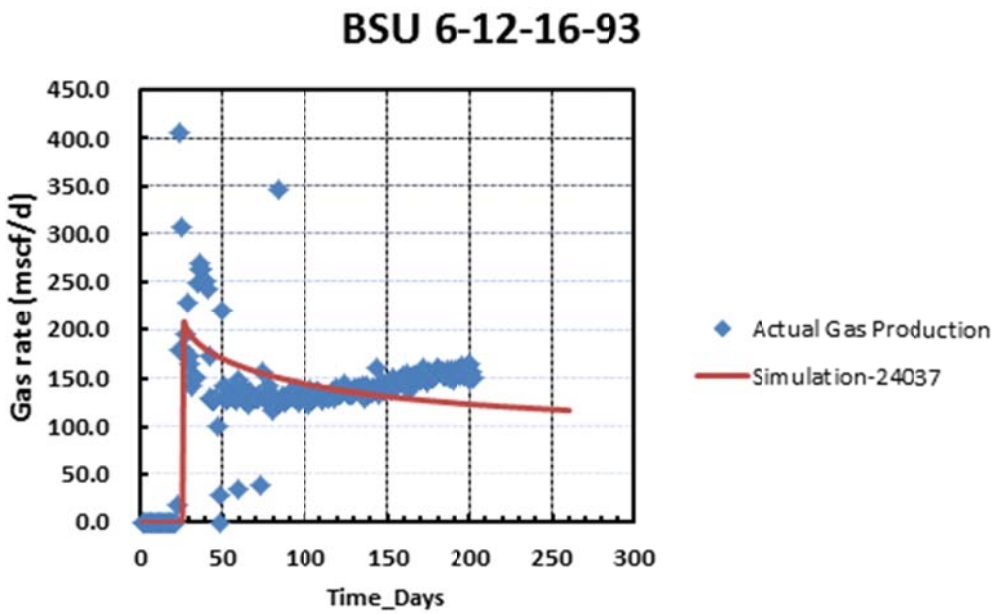

Figure 85: Well BSU-6-12-16-93

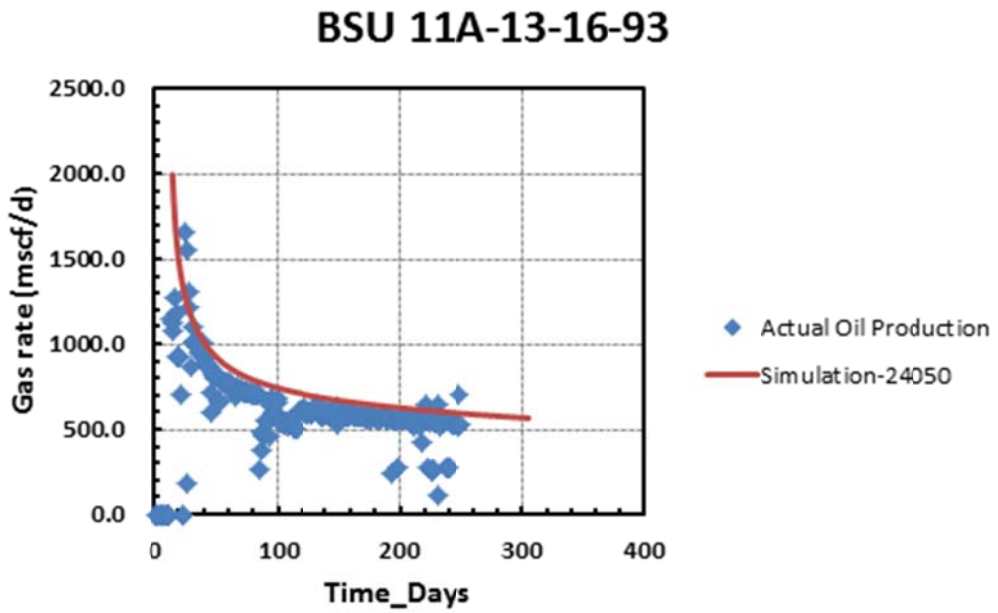

Figure 86: Well BSU 11A-13-16-93

We are told by Devon that some wells are continuing to show improvement in performance; however, in general, the results have been disappointing. We hope that the future performance will continue to improve.

STREAMLINE SIMULATION

By Akhil Datta-Gupta, Texas A & M University

In addition to using conventional – finite difference based – simulation, we also examined streamline based simulation to understand how we can predict the un-contacted reservoir. Streamlines have been very effectively used for computing swept volumes and drainage volumes in oil reservoirs. However, there is an incorrect but commonly held perception that streamlines cannot be used for gas reservoirs. In fact, streamlines exist whenever there is an underlying velocity field – both in compressible and incompressible flow. In this paper, we present one of the first applications of streamlines to tight gas reservoirs for drainage volume calculations of producing wells, optimal placement of infill wells.

Current practice of well placement in tight gas reservoirs generally involves the use of empirical correlations based on reservoir properties and past production histories and/or pressure maps from flow simulation. No rigorous procedure is available to compute well drainage volumes in the presence of heterogeneity and hydraulic fractures, particularly for complex wells. We propose a fast approach for drainage volume calculations based on the streamlines and diffusive time of flight and demonstrate its application to optimize well placement. Our approach relies on a high frequency asymptotic solution of the diffusivity equation and emulates the propagation of a 'pressure front' in the reservoir. This allows us not only to compute rigorously the well drainage volumes as a function of time but also examine the potential impact of infill wells on the drainage volumes of existing producers. Using these results, we present a systematic approach to optimize well placement to maximize the estimated ultimate recoveries (EUR).

We demonstrate the power and utility of our method using both synthetic and field applications. The synthetic example is used to validate our approach by establishing the consistency between the

drainage volume calculations from streamlines and the EUR. The field example is from the Wamsutter gas field. We utilize the streamline-based drainage volumes to identify depleted sands and generate a reservoir quality map to optimize future well placement based on the intact regions. The field application clearly demonstrates a systematic and efficient approach to optimal well placement in tight gas reservoirs.

Introduction

Estimation of the reservoir size and drainage volumes of individual wells is very important key in management and development of oil and gas fields. These properties are directly related to economic problems like planning a new infill well in producing field and adjusting wells schedule to maximize production. For accurate production estimation, various approaches have been proposed and applied to synthetic and field cases. Earlier works of. Anderson[27] proposed a reservoir volume calculation technique, which is based on pressure profile of a field and mapping over reservoir. Authors drew a pressure contour to provide simple analytical scheme that yield a basic understanding of drainage area and suggested its usefulness on infill drilling, well abandonment and water injection. But this approach required too many assumptions such as limited to horizontal, homogeneous, isotropic, two dimensional reservoirs and so on. Nordaas Kulkarni, *et al*.[28] suggested the generalized streamline approach to mimic transient-pressure function by introducing a diffusive time of flight. They showed that 'diffusive' time of flight can be used to define the drainage radius in case of primary recovery or compressible flow under homogeneous and heterogeneous conditions. He, *et al*.[29] tried to match the arrival time of a transient-pressure front and the decline-type curve that was derived from pseudo-steady state flow condition. They mainly focused on reconciling the drainage volume calculations from decline curve analysis and streamline model. They concluded that their proposed approach can be used for inferring the flow barriers and reservoir compartmentalization, which are used for drainage volume estimation.

Da Cruz, *et al*.[30] used 'the quality map' to estimate the production potential of a reservoir. They showed a good correlation between the average value of the uncertainty quality map and the uncertainty of flow response in 2D cases. They suggested that this quality map can be a good estimator in choosing locations for vertical producer wells. Kim, *et al*.[31] presented the exactitude of pressure trajectories and 'diffusive' time of flight. They verified this 'diffusive' time of flight can be used for identifying physical properties of reservoir instead of pressure transient test results and applied this results on an oil reservoir.

Previous studies had been mainly focused on incompressible flow even though this 'diffusive' time of flight can be applied to compressible flow. So, the objective of this study is verifying the applicability of 'diffusive' time of flight in compressible fluid. We propose the diffusivity which can be used for both compressible and incompressible flow for diffusive streamline calculation. This functionality is a very powerful tool in heterogeneous reservoir even for very unconventional cases like 'tight' gas fields.

We also suggest a 'drainage volume calculation' technique which based on 'diffusive' time of flight and its mapping onto grid block. Our drainage volume calculation and visualization outputs are brought together with 'diffusive' time of flight calculation, so it is very handy to conceptualize and quantify the effective drainage area in each production time steps. These calculations can provide a strong tool for optimal infill well drilling and staged fracturing optimization.

Approach

Transient pressure response of fluid movement in porous media is governed by diffusivity equation and asymptotic approaches to inversion have been applied in several other disciplines such as medical, optical and geophysical imaging (Gordon and Herman[32], Iyer and Hirahara[33], Arridge[34]). In this section, we discuss the asymptotic solution for the transient gas flow assuming the real gas pseudo pressure method.

It provides the mathematical foundations with which we can relate the streamlines and ray methods from geophysics (Vasco and Finsterle[35]). It was also applied to tracer tests, transient pressure inversion and two-phase flow data (Vasco and Datta-Gupta[36], Vasco *et al*[37], Vasco and Datta-Gupta[38]). Here, we revisit the asymptotic approach for analysis of transient pressure response in real gas flow in porous media.

The transient pressure response in a heterogeneous medium with constant compressibility is described by the well-known diffusivity equation,

$$\phi(\mathbf{x})\mu c_t \frac{\partial P(\mathbf{x},t)}{\partial t} - \nabla \cdot \left(k(\mathbf{x})\nabla P(\mathbf{x},t)\right) = 0 \tag{11}$$

This equation is already linearized for liquid flow by deletion of terms, assuming that viscosity is independent of pressure and compressibility is small and constant. Obviously these assumptions may not be true for real gas flow in porous media, so we need the real gas pseudo pressure formulation (Al-Hussainy, *et al*.[39]) to linearize the diffusivity equation. After proper transformation, same differential equation as Equation 11 can be obtained based on the pseudo pressure variable. Consequently, all the derivations for compressible flow can be applied for incompressible flow. In pseudo pressure approach, Al-Hussainy, *et al*. linearized the basic flow equation using the following version of the Kirchhoff integral transformation,

$$m(p) = 2\int_{p_b}^{p} \frac{pdp}{\mu z} \tag{12}$$

By using the above transformation, basic diffusivity equation can be linearized for gas flow in porous media as follows,

$$\phi(\mathbf{x})\mu c_t \frac{\partial m_p(\mathbf{x},t)}{\partial t} - \nabla \cdot \left(k(\mathbf{x})\nabla m_p(\mathbf{x},t)\right) = 0 \tag{13}$$

You can see that Equation 13 is equivalent of Equation 11 and the only difference is that the pressure is replaced by pseudo pressure. Now, we can transform Equation 13 into frequency domain using the Fourier transform. We obtain the following equation.

$$\frac{\phi(\mathbf{x})\mu c_t}{k(\mathbf{x})}(-i\omega)\tilde{m}_P(\mathbf{x},\omega) = \nabla^2 \tilde{m}_P(\mathbf{x},\omega) + \frac{\nabla k(\mathbf{x})}{k(\mathbf{x})} \cdot \nabla^2 \tilde{m}_P(\mathbf{x},\omega) \tag{14}$$

The asymptotic solution for a transient pressure response assumes the following form

$$\tilde{m}_P(\mathbf{x},\omega) = e^{-\sqrt{-i\omega}\tau(\mathbf{x})}\sum_{k=0}^{\infty}\frac{A_k(\mathbf{x})}{\left(\sqrt{-i\omega}\right)^k}. \tag{15}$$

The asymptotic solution, Equation 15, is the summation of an infinite number of terms with coefficients $A_n(\mathbf{x})$. High frequency terms (large ω) in the series describe the physical propagation of a 'pressure front' and we only need to consider the first few terms. If we consider the first term only, then

$$\tilde{m}_P(\mathbf{x},\omega) = e^{-\sqrt{-i\omega}\tau(\mathbf{x})}A_0(\mathbf{x}) \tag{16}$$

After inserting Equation 16 into Equation 14 and collecting terms with the highest order of $\sqrt{-i\omega}$, we obtain the equation for the front propagation in an isotropic permeable media,

$$\nabla\tau(\mathbf{x})\cdot\nabla\tau(\mathbf{x}) = \frac{1}{\alpha(\mathbf{x})} \tag{17}$$

Where, $\alpha(\mathbf{x})$ is the diffusivity coefficient given by

$$\alpha(\mathbf{x}) = \frac{k(\mathbf{x})}{\phi(\mathbf{x})\mu c_t} \tag{18}$$

Variety of propagation behavior is explained by Equation 17 which is the well-known Eikonal equation (Kravtsov and Orlov[40]). In particular, it is important to note the close relationship that Equation 17 has with the streamline time of flight equation which describes the propagation of a neutral tracer (Datta-Gupta and King[41]). By analogy with the time of flight formulation, we can define a diffusive time of flight for propagation of a pressure front as follows,

$$\tau(\mathbf{x}) = \int_{\psi}\frac{d\zeta}{\sqrt{\alpha(\mathbf{x})}}, \tag{19}$$

Diffusive time of flight is defined along the trajectory of a 'pressure front' ψ, and these trajectories can be inconsistent with the streamlines. The pressure front trajectories have been compared with streamlines trajectories and it is shown that the diffusive times of flight and pressure front trajectory are invariant with time for a given geological model and boundary conditions, while streamlines will depend on the instantaneous pressure at each location and thus, they are function of time. However, after the very early time, the streamline profile becomes stable quickly and general characteristics of both pressure front trajectories and streamlines are identical. These results indicate that the streamlines can be a reasonable approximation of the pressure front trajectory. This is very important and will let us use available streamline trajectories for diffusive time of flight calculations instead of pressure trajectories.

We can see that we obtain the similar basic equations for real gas pseudo pressure approach as the ones for incompressible flow. We will show that this derivation is valid by comparing our results with the peak arrival time calculated based on the methodology suggested by Jong Uk Kim, *et al*.[31] Also, note that the unit of diffusive time of flight is the square root of time which is consistent with the diffusive flow behavior. For the gas flow applications, we recognized from Equation 18, we need to clearly address the total compressibility term. For compressible flow, we cannot assume a constant or small compressibility value for using Equation 18. So, we calculate the total compressibility for diffusivity with the following

equation. The derivation of formation volume factor with respect to pressure can be calculated from information saved at each time step of simulation run.

$$C_t = \sum_{i=O,W,G} S_i C_i + C_R \quad ; \quad C_i = -\frac{1}{B_i}\frac{dB_i}{dP_i} \tag{20}$$

This will assure that diffusive time of flight is calculated correctly along the streamlines based on the current pressure and saturation of the streamline segment. We examined the behavior of the diffusive flow and diffusive time of flight for compressible flow so far. The physical relationship between the diffusive time of flight and the propagation front of pressure can be obtained by investigation of the time domain solution to the zeroth order asymptotic expansion in Equation 16. So for a 3-D medium, we will obtain the following relationship,

$$\tilde{m}_P(\mathbf{x},t) = A_0(\mathbf{x})\frac{\tau(\mathbf{x})}{2\sqrt{\pi t^3}} e^{-\frac{\tau^2(\mathbf{x})}{4t}} \tag{21}$$

This corresponds to the pressure response for an impulse source or sink. The pressure response will be maximized at a fixed position **x**, when

$$\frac{\partial \tilde{m}_P(t)}{\partial t} = A_0(\mathbf{x})\frac{\tau(\mathbf{x})}{2\sqrt{\pi}} e^{-\frac{\tau^2(\mathbf{x})}{4t}} \left(-\frac{3}{2} t^{-\frac{5}{2}} + t^{-\frac{3}{2}} \frac{\tau^2(\mathbf{x})}{4t^2} \right) = 0 \tag{22}$$

Taking the first derivative from Equation 12 results in the following relationship that,

$$\frac{\partial m(p)}{\partial t} = \frac{2p}{\mu z}\frac{\partial p}{\partial t} \tag{23}$$

Equation 23 shows if derivative of the pseudo pressure is equal to zero, the derivative of the real pressure is also zero. So considering Equation 23, we can see that Equation 22 provides us a relationship between the diffusive time of flight and physical time when the pressure response (drawdown or build up) reaches a maximum at position **x** along the streamline.

$$t_{\max} = \frac{\tau^2(\mathbf{x})}{6} \tag{24}$$

It has been proved (Jong Uk Kim, *et. al.*[31]) that for a 2-D medium above equation will be modified to,

$$t_{\max} = \frac{\tau^2(\mathbf{x})}{4} \tag{25}$$

We have used the idea of 'the peak arrival time' to validate our results for pressure front calculations based on diffusive time of flight. According to the previous researchers, the arrival of the pressure front at a location can be interpreted as the time when the pressure reaches maximum or minimum at that point corresponding to an impulse source or sink. Furthermore, our derivations show that same analogy used for calibration of high-resolution oil reservoir models using transient pressure data can be used for gas reservoirs.

Generally in field applications, we do not have an impulse source or sink. Instead, we have a step change in rate (shut-in or start-up) which can be approximated by a 'Heaviside' function. Noting the fact that the impulse function is the derivative of the Heaviside function, for practical applications we will compute the peak arrival time corresponding to the derivative of the pressure data rather than the pressure data itself. Figure 87 shows a comparison of peak arrival time between numerical results from the finite difference simulation (upper three figures) and from numerical integration described in Equation 19 along the streamlines (lower three figures) for several different times in a homogenous single phase gas reservoir. This model size is 41 by 41 and a well is located at the center of the model. Based on Equation 19, the diffusive time of flight is integration along the pressure front trajectory. However, approximating these trajectories using streamlines also results in a similar profile of peak arrival time. This has been investigated by Jong Uk Kim, *et al*.[31] with direct calculation of pressure front using pressure field of a finite difference simulator and Kulkarni, *et al*.[28] with an analytical solution of drainage area. These results indicate that the streamlines can be a reasonable approximation of the pressure front trajectory. Results in Figure 87 are for a 2-D model so we have used Equation 25 to change the diffusive time flight domain to physical time domain.

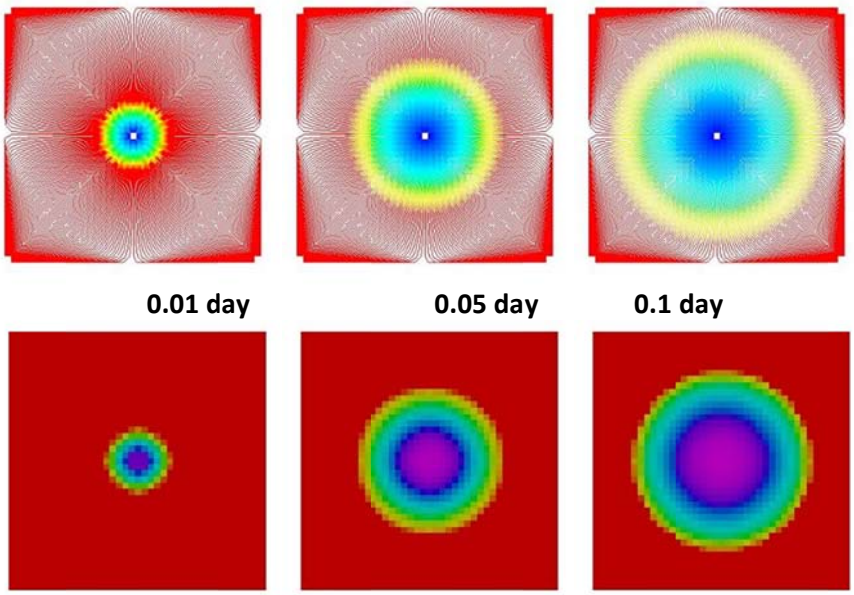

Figure 87: Pressure front arrival time in homogeneous field. Lower three figures are computed from pressure response from finite difference simulation and Upper three figures are computed from diffusive time of flight along streamline

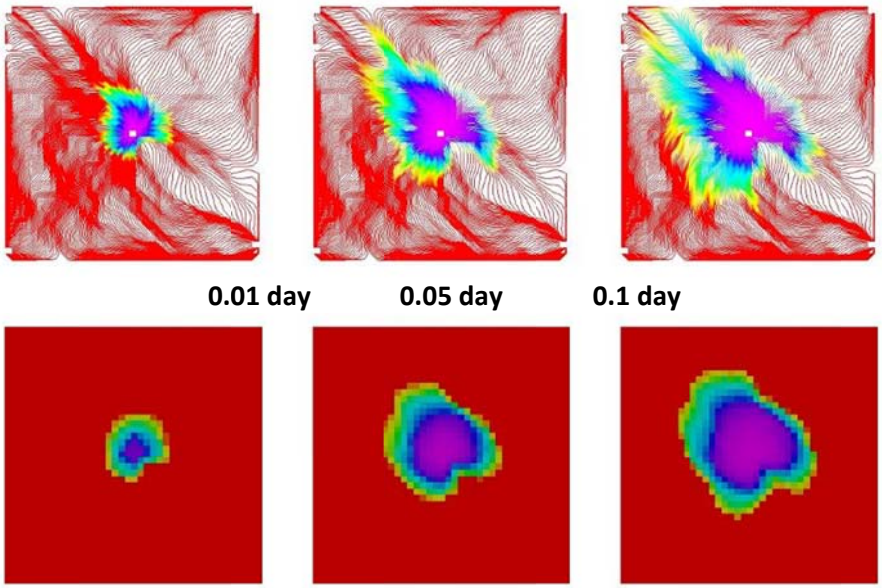

Figure 88: Pressure front arrival time in heterogeneous field. Lower three figures are computed from pressure response from finite difference simulation and Upper three figures are computed from diffusive time of flight along streamline

Figure 88 shows the same comparison for a 2-D heterogeneous model. Same calculations as described for Figure 87 are used for this case too. Again, we can see a reasonable match between numerical results from the finite difference simulation (upper three figures) and those from numerical integration (lower three figures) for several different times. Also we can see that streamlines provide a reasonable resemblance to the real pressure trajectories for single phase gas model.

By looking at the lower figures in Figure 87 and Figure 88 we can immediately visualize the drained parts of the model. This will give us a strong tool to calculate and visualize drainage volumes for any particular producer without any further calculations. We use reverse tracing approach to make sure that each grid block in the reservoir will be assigned a value for diffusive time of flight. Reverse tracing approach is following the same procedure as forward tracing with the difference that we start the streamlines from the cell centers to producers. Benefits of this approach are that each grid will get a single value for diffusive time of flight and we don't need any averaging of the different values for each cell. Also, this will help us to assign to each grid block a specific producer. It may happen that two streamlines passing same grid block, ending to different producers, in this case we consider the streamline that starts from the grid block center to decide on which producer it belongs to. This has been illustrated in Figure 89.

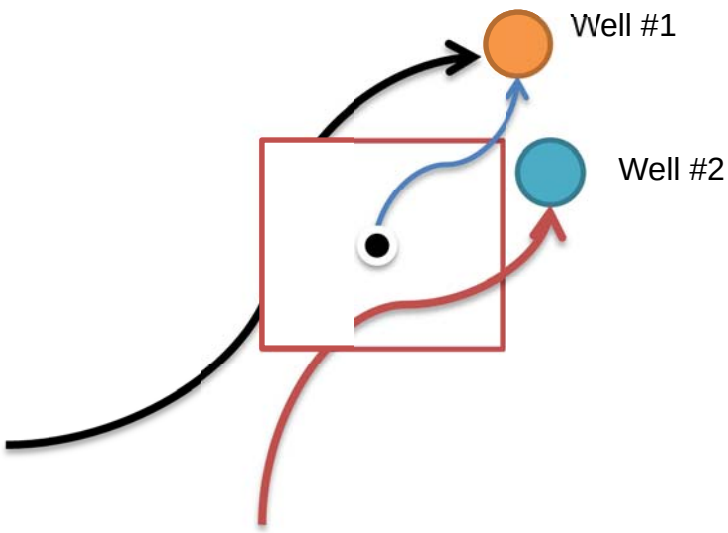

Figure 89: Reverse streamline tracing from cell center

Using reverse tracing and mapping the diffusive time of flights to original grid blocks we can generate the drainage volume map for the model. Such a map is generated for 2-D heterogeneous model in Figure 88 and results are shown in Figure 90. These maps can be used to investigate the interference of the new infill wells. New infill wells can be drilled into the virgin sands that has not been drained yet based on the generated maps. Such a decision can be also made by looking the pressure distribution of the field at any particular time. In next illustrative example we will try to show how new method can generate a clear map while pressure maps has the ambiguity of choosing the right pressure cut off value to decide the correct drainage volume.

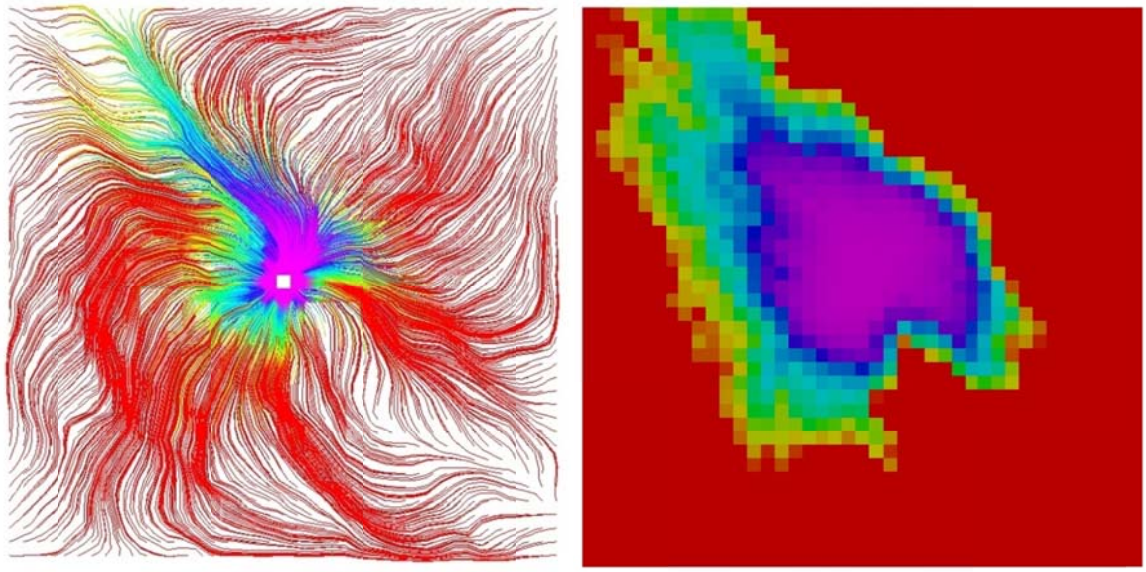

Figure 90: Reverse tracing in heterogeneous case and mapping to original grid blocks to visualize the drainage volume

Assume that we need to know the drainage volume in the heterogeneous 2-D model presented in previous examples at the t = 0.125 days. Top left figure in Figure 91 shows the drainage volume map generated from the diffusive time of flight calculations at the corresponding time. Top right figure in the same figure shows the pressure distribution at the same time. Pressure range in reservoir is from 2,118 psi in producer's grid block and up to 3,000 psi in boundary which is initial reservoir pressure. Bottom figures in Figure 91 also shows the pressure map for the same reservoir at the same time of t = 0.125 days but we have used different cut off values as 2,750, 2,850 and 2,950 psi to find the drainage volume. Using these cut-offs means that we are assuming that those regions of the reservoir which have the pressure equal or less than the cut off value are being drained.

From Figure 91 we can see that new approach can produce a clear map of the drainage volume compared to the pressure depletion map. Pressure distribution profile has a very low resolution and its smoothness makes it difficult to see limits vividly. Also as you can see from bottom pictures in the same figure, choosing the right cut off value is going to be the next question which we cannot easily decide and it can be different depending on initial pressure and geology. Also, drainage volume map, generated from diffusive time of flight approach, gives a unique depletion time to each grid block.

In next section, we will show the application of the diffusive time of flight approach in quantifying the drainage volumes in for Wamsutter field. Furthermore, we will show how this method can help us to detect the interference effect of the new infill wells and could be useful for minimizing these types of interferences and optimization of the new infill wells.

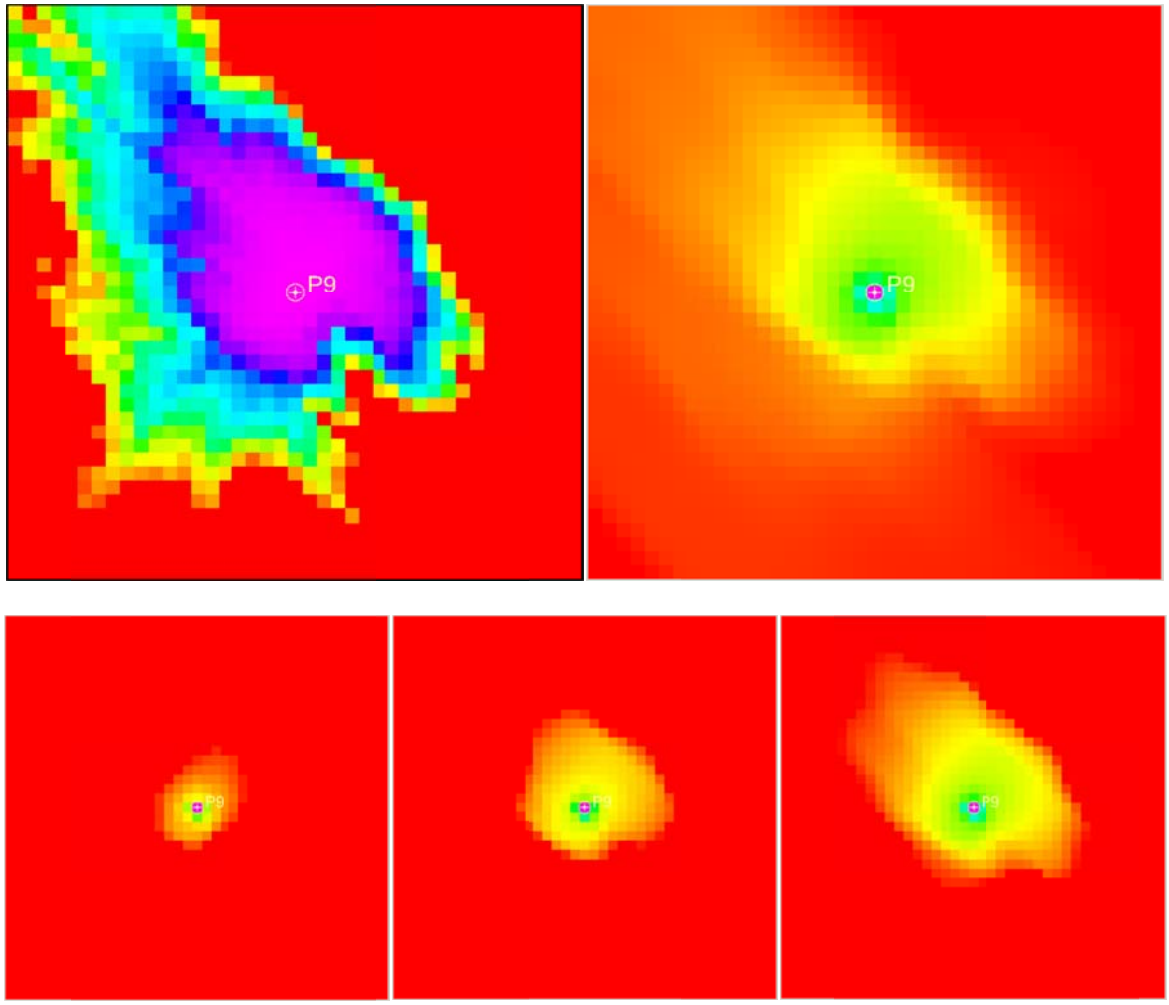

Figure 91: Comparison of drainage volume maps based on the diffusive time of flight (top left) and pressure depletion map (top right). Bottom from left to tight: drainage volume maps based on the pressure maps using cut off values of 2,750, 2,850 and 2,950 psi.

Application

In this section, we discuss application of the drainage volume calculations for two cases; first a section of a tight gas reservoir with two synthetic wells and second for whole reservoir model. The section model is used to show the application of the new method by just looking at two wells. This will make the analysis easy to understand because there is no interference from other wells. In full reservoir model, we apply it to Wamsutter field to show the applicability of our approach to high resolution and geologically complex tight gas field.

Field Section Example

Our Field section model is a three dimensional example and two wells are producing from the field. The original model had 361 layers and it is coarsened to 65 layers using methodology introduced by Hosseini and Kelkar.[16] Second well is an infill well which has been added to the field after three years of production. The geologic model consists of 18×15×65 grids. Figure 92 shows the permeability field

of this model along with the well locations. Figure 93 shows the diffusive time of flight distribution before and after drilling a new infill well. As you can see after drilling a new well, some of the drainage volume of first well is being interfered by second well and flow is diverted to new well. New method is providing an easy and fast way to quantify these effects.

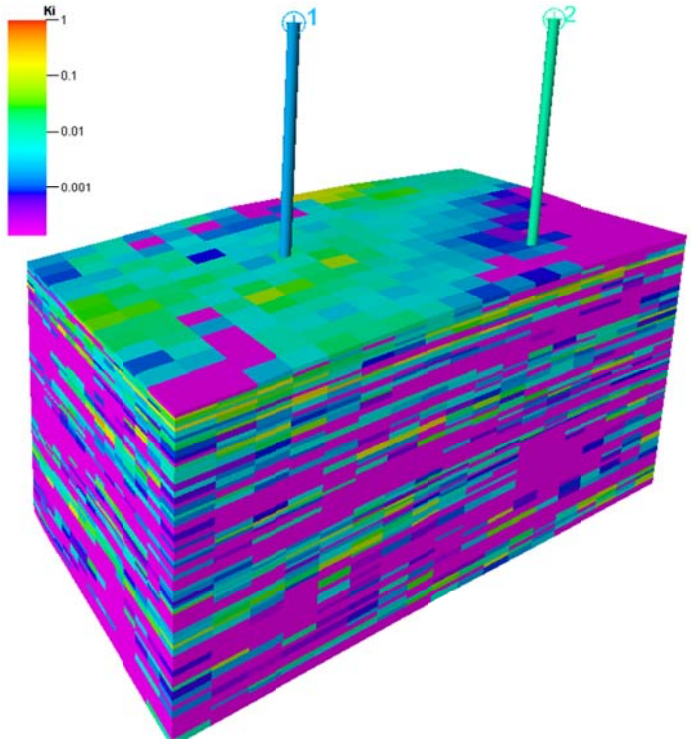

Figure 92: Permeability field of tight gas reservoir (section of model) permeability ranges from 3 to 0.0001 md.

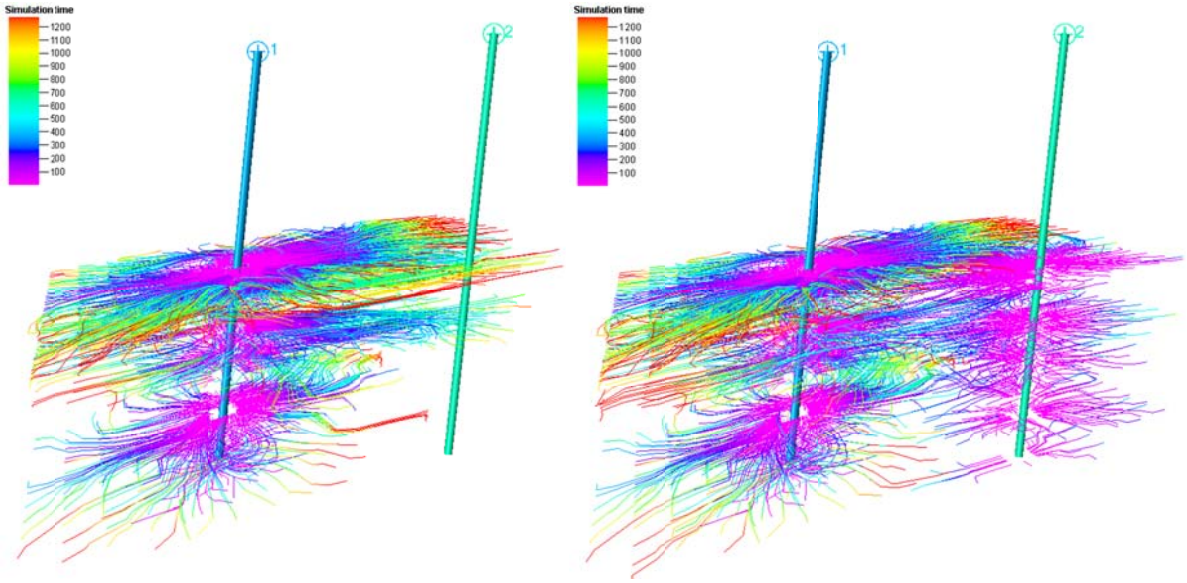

Figure 93: Diffusive time of flight distribution before and after drilling the new infill well.

Figure 94 compares drainage volume calculated with a new approach with the one based on pressure cut off calculations after one year of production. Initial reservoir pressure is about 3,860 psi and lowest pressure in the field after one year is about 2,184 psi at producer location. We used cut off values of 3,600, 3,700 and 3,800 psi to map the drainage volume based on the pressure values. By comparing the maps, one can see that new method generates very clear map of drainage volume and assign a unique physical drainage time while pressure map could vary dramatically depending on the cut off value. Also as we get closer and closer to 3,860 psi (initial reservoir pressure), cut off values will be very sensitive and adding even 5 psi to cut off value can change the drainage volume dramatically. This is because pressure distribution, especially far from the wells, has very low resolution and changes very smoothly. On the other hand, we can see that even if we get the cut off value right, still maps from new method and pressure method look different. As shown in Figure 94, if we compare the drainage volume map calculated from new method (top left) with the map calculated from pressure map for cut off value of 3,800 psi (bottom right), those two figures show that new method has bigger drainage area and even reaches to the second well while pressure based maps show higher and smoother drainage volume.

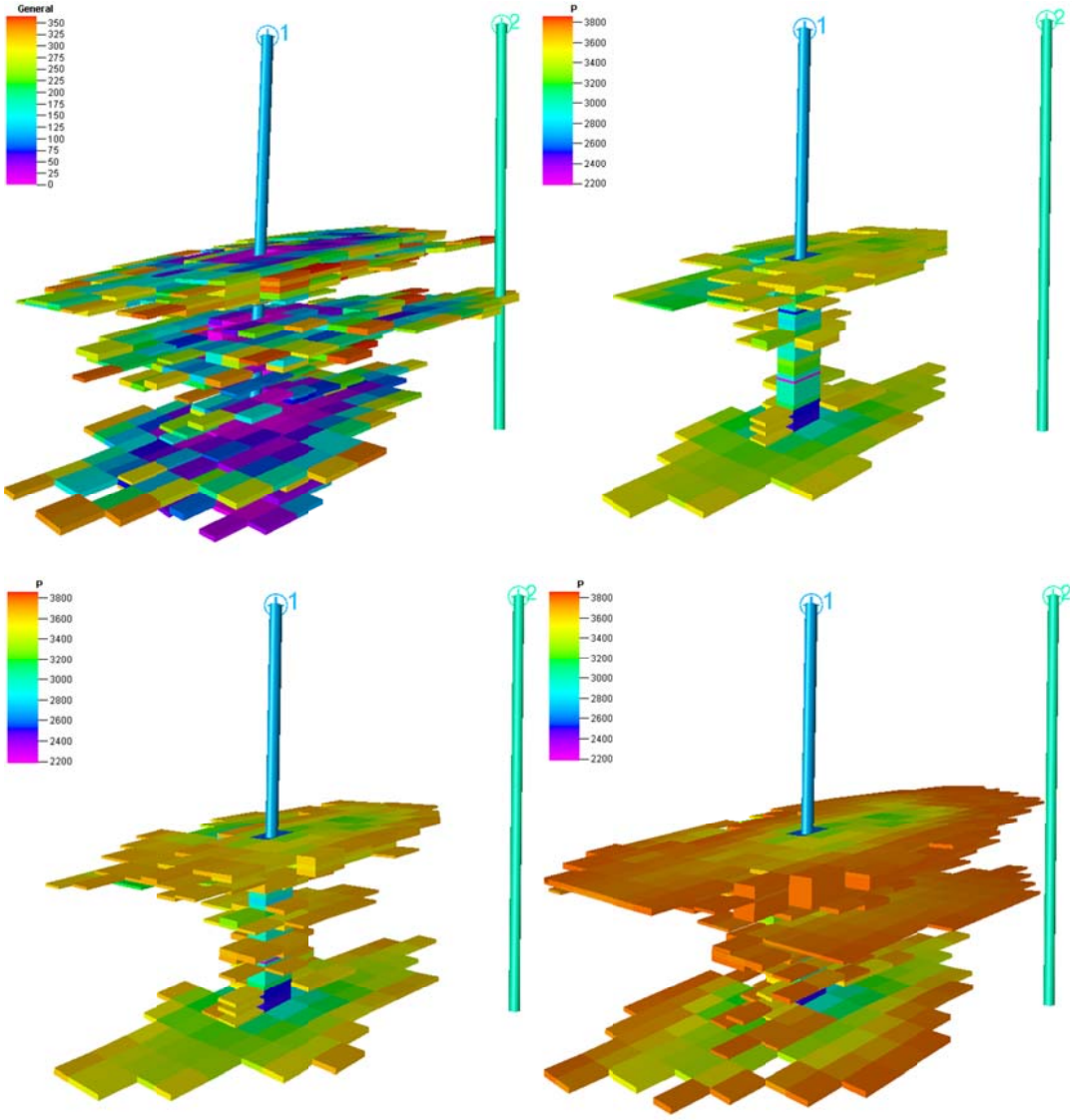

Figure 94: Drainage volume maps. Top left: based on diffusive time of flight. Top right and bottom; using cut off values of 3,600, 3,700 and 3,800 psi for pressure

The capability to map unique drainage volumes at each time step enables us to exactly calculate the drainage volumes with respect to each producer. Figure 95 shows drainage volume calculations for this section model. As soon as the second well is drilled, the drainage volume of the first well is dropped significantly. We have included the scenario that no infill well is being drilled to be able to calculate the incremental production obtained from the drilling of the second well. This information can be used to minimize the drainage volume interferences of the wells. Also this approach could be effectively combined by an NPV maximization procedure to maximize the NPV by using minimization of the drainage volume interferences and considering infill well drilling costs.

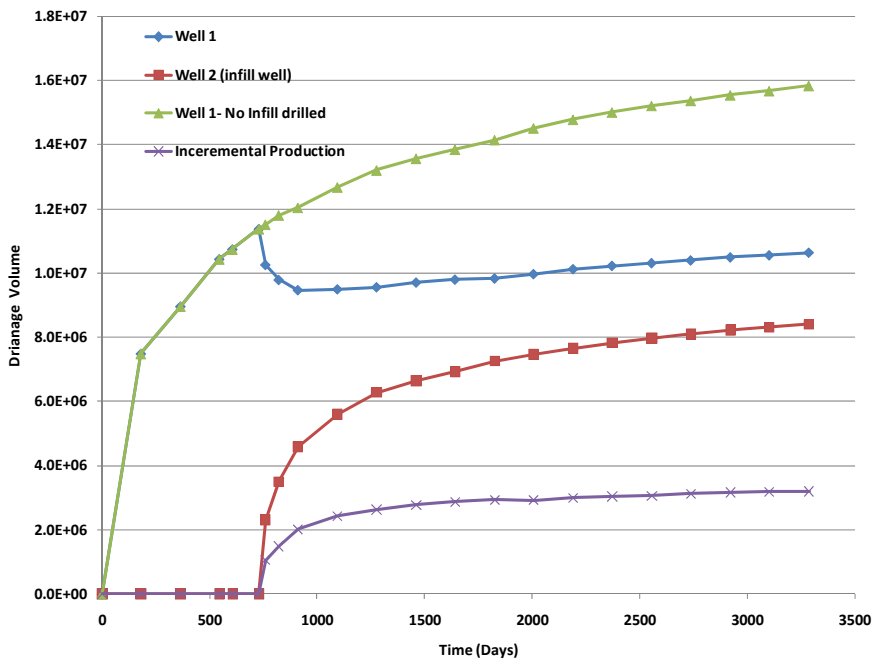

Figure 95 Drainage volume changes due to the drilling of a new infill well.

Wamsutter Application

In this section, we discuss the application of the drainage volume calculations based on the diffusive time of flight for a Wamsutter reservoir with more than 80 wells. Figure 96 shows the drainage volume map calculated based on the diffusive time of flight after 25 years of production for this field. For the first three years there is only one well producing and field is being developed after that time.

In Figure 97, right figure shows the total drainage volume change in the field and field cumulative gas production. Total drainage volume decreases at during some periods because of temporary shut-ins of some wells. Figure on the left shows the drainage volume changes for each individual producer. By taking a closer look we can see that several wells have been interfered by surrounding wells. Three of them are being highlighted in the figure for further examination. To be able to have a closer look at these wells, we have graphed the individual wells and only their surrounding wells in Figure 98.

By examining Figure 98 we can see that how new infill wells as they are being drilled in different times affecting the drainage volume of the selected producer. Also the amount of reduction in drainage volume illustrates the extent of the effect. For example in Figure 98, top right figure shows that the first infill well impact on selected producer is not as big as the impact from the second infill well.

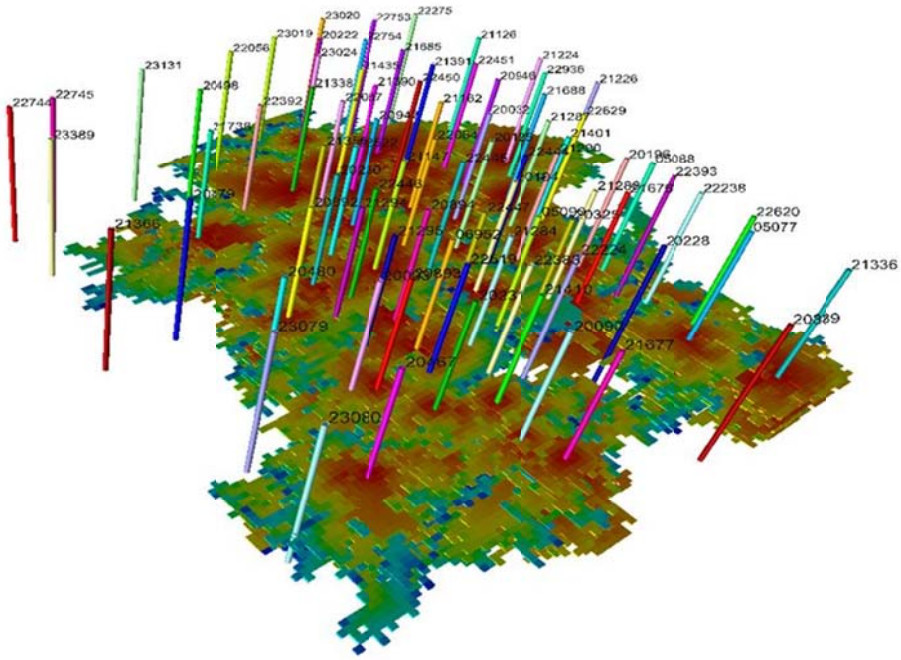

Figure 96: Drainage volume map based on the diffusive time of flight calculations.

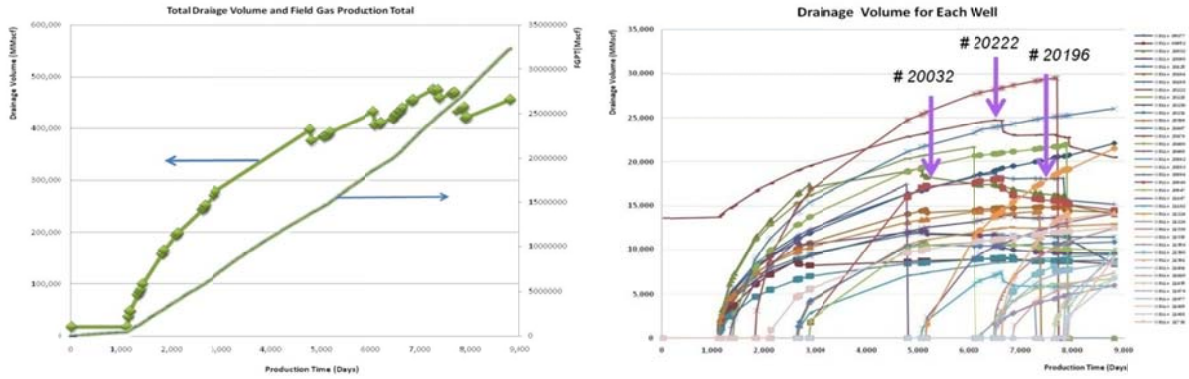

Figure 97: Left: Total drainage volume and cumulative gas production. Right: Drainage volume for each individual well.

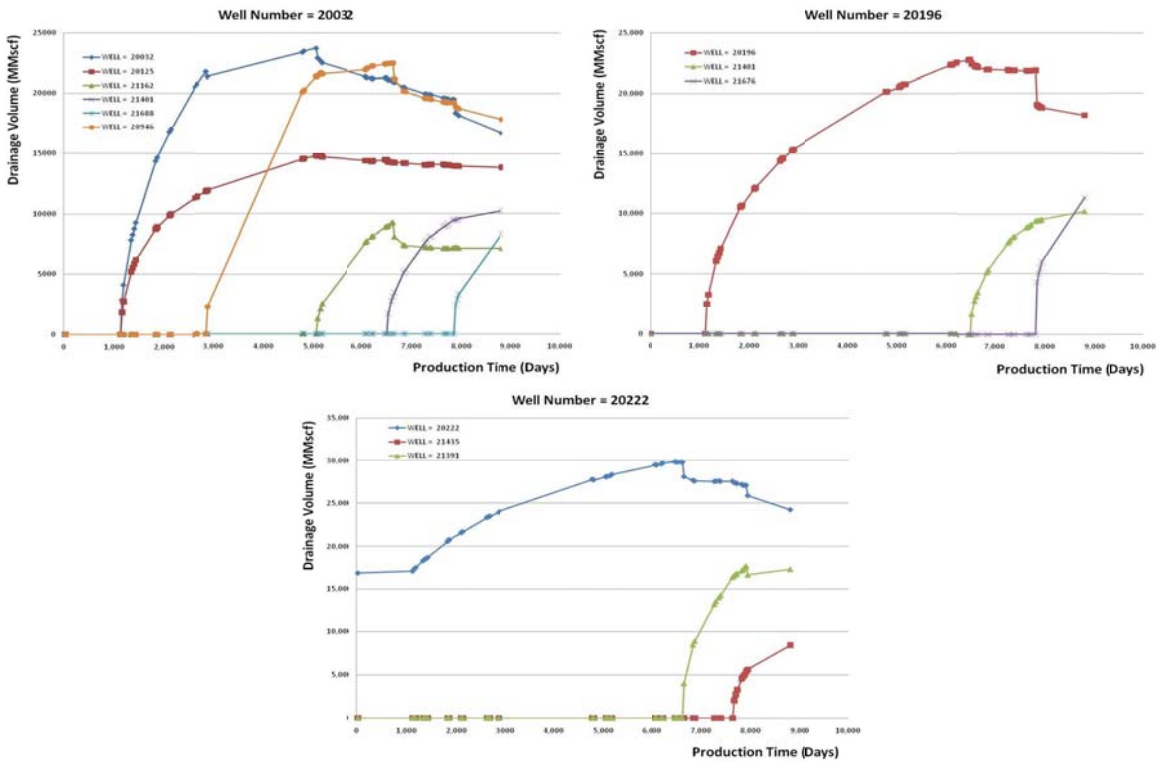

Figure 98: Drainage volume interference on producers from new infill wells.

Quality Map for Well Placement

Assume that we are planning to drill a third well in the reservoir section that we discussed before. Based on the idea that we developed in previous section, now we have a good idea that which parts of the reservoir is being depleted at any time of reservoir life. We will try to generate a quality map that will help to select best regions of the reservoir for infill well drilling without running any extra simulation. From diffusive time of flight calculations, at any given particular time, we know that pressure front has reached to a grid block in the reservoir or not. This is shown in Figure 99 after 9 years of production from well 1 and 2. To assign a production potential for each new location assuming that a vertical well is being planned to be drilled on that location we define the flow capacity term for each undepleted grid block which is based on Darcy's equation and weighted by net rock volume.

$$FlowCapacity = \frac{k(x) \cdot V(x)}{\phi(x)} P(x) \tag{26}$$

For each location, we sum up the flow capacity term in the neighborhood of that location only for grid blocks that pressure front is not reached and we ignore the flow capacity of grid blocks which already are being depleted based on our diffusive time of flight map. This will help us to minimize the interference of the new well on the current producing wells. At the end, we will end up with a map which represents the flow potential around that location (top right of Figure 100). By the method that we just described we can generate a quality map which represents the flow potential of the reservoir at any location. Also we run multiple simulations for every possible drilling location (for a model with size of 15×18×65, we need 270 simulation runs; took around 24 hours in PC) and

generate true EUR map to compare with our quality map. By examining Figure 100, we can see that quality map can provide a reasonable map for next drilling location. Both maps showing that the top right part of the reservoir has the maximum potential for drilling the third well.

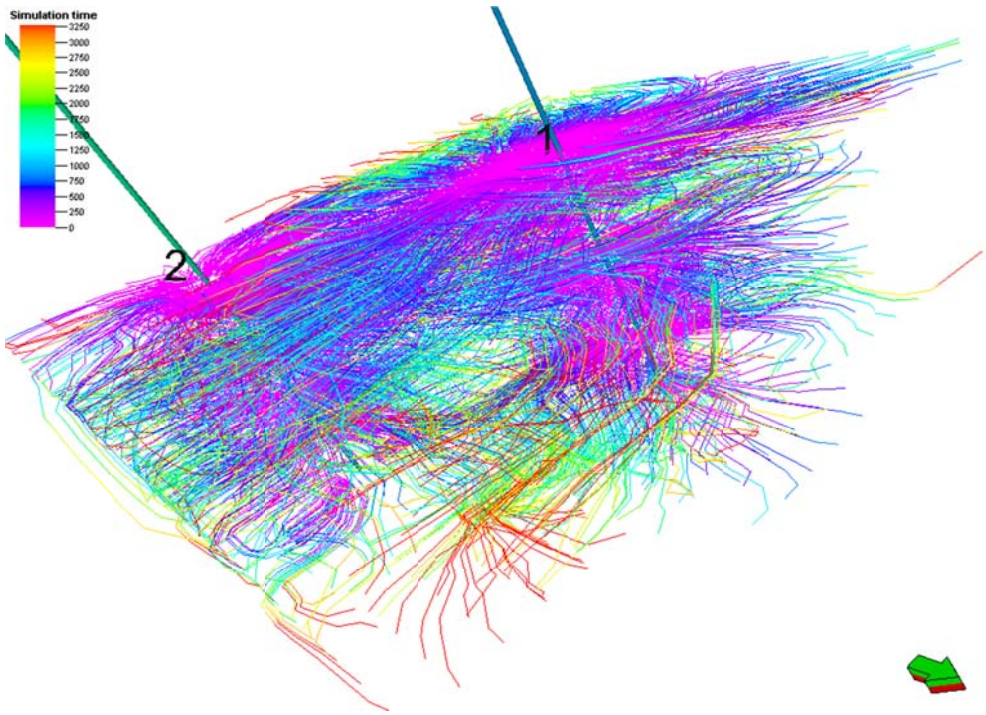

Figure 99: Based on the diffusive time of flight we can see which grid blocks are depleted and find the regions with maximum flow potential for next infill well.

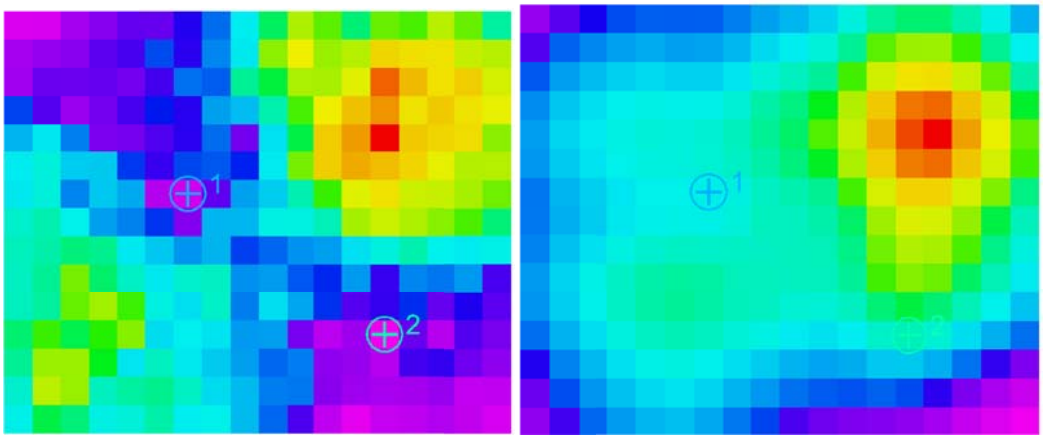

Figure 100: Quality map generated on the right can provide a reasonable match to true EUR map on the left.

This quality map also can be easily generated at real field without additional efforts. Figure 101 can be used for deciding new infill well locations instead of ambiguous pressure map which is usually referred by field engineers for decision. This map is obtained without additional simulation. But for calculating true EUR map, the calculation time is estimated more than 2 months with dual core PC.

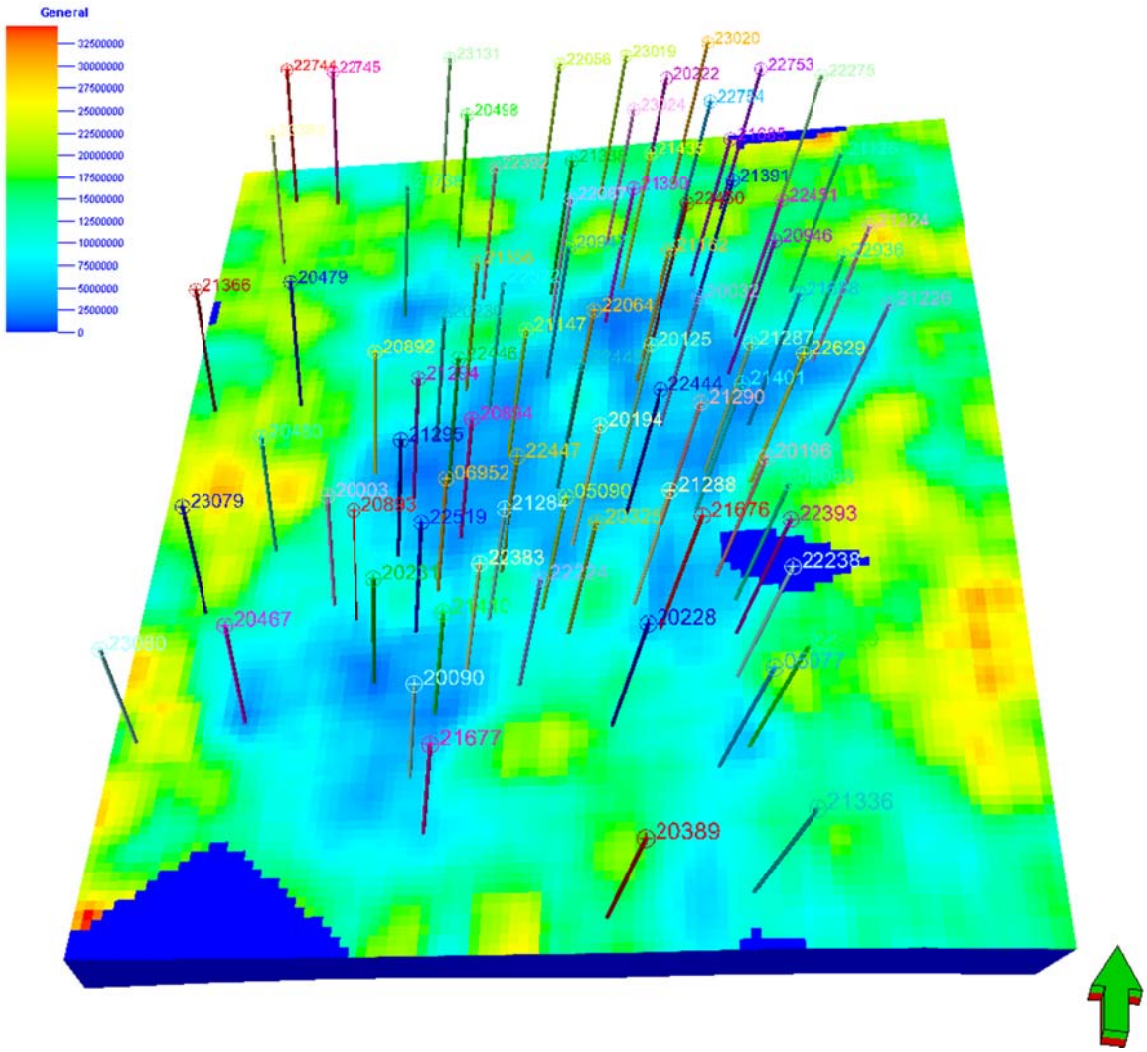

Figure 101: Quality map generated from Wamsutter tight gas field

The quality map in Figure 101 is calculated at the last time step of simulation schedule file. With this quality map information, we can decide the next infill well drilling location. The highest probable regions are shown as red, so for example, we can try to drill between well 21368 and well 23079 or left side of well 22238 for next infill well locations.

CONCLUSIONS

Based on our study, we can derive the following conclusions:

- Production data can be effectively used to understand the contribution due to acceleration versus incremental production for new infill wells.
- Most of the production from tight gas reservoirs can be represented by either linear or bi-linear flow over a long period of time
- As the spacing gets smaller, the overall EUR will decrease, the incremental contribution would become smaller and acceleration component will get larger. Having an area which has large EUR

with relatively large contribution from incremental contribution is the most desired area for additional infill drilling.

- We validated our approach by applying it to Wamsutter field and made recommendations to Devon for drilling new wells.
- We also provided the infill wells by conducting detailed reservoir simulation study. We adjusted the hydraulic fracture conductivity and length to match the performance of the wells and then predicted the performance of the new wells.
- We compared the performance of newly drilled wells with what we had predicted. Although the amount of information we have collected is limited, the performance of the newly drilled wells is worse than what we had predicted. Some wells continue to show improvement in performance but, in general, the results have been disappointing compared to what we had predicted. When we matched the performance of new wells with simulator, we observed lot smaller fracture conductivity compared to existing wells in the field. Devon is currently examining the reasons for unusual performance of these wells.
- We used streamline simulator to predict the infill well locations. Unlike pressure, which is highly diffusive property, diffusive time of flight is much more effective tool for determining un-drained areas.
- We demonstrated the use of diffusive time of flight by applying it first to a synthetic case, and then for Wamsutter field to indicate potential infill well locations.
- We also used quality indicator to supplement the streamline calculations. This quality indicator is a good indicator of what EUR would be expected from a newly drilled infill well.

REFERENCES

1. Personal communication with Dale Reitz, Devon geologist on February 19, 2009.
2. Personal Communication with Ralph Merry, Devon Energy Petrophysicist, on September 25, 2009.
3. Cipolla, C. L. and Wood, M. C.: "A Statistical Approach to Infill-Drilling studies: Case History of the Ozona Canyon Sands," Paper SPE 35628 presented at the 1996 Gas Technology Symposium, Calgary, April 28-May 1.
4. McCain, W. D. Jr., Voneiff, G. W., Hunt, E. R., and Semmelbeck, M. E.: "A Tight Gas Field Study: Carthage (Cotton Valley) Field," Paper SPE 26141 presented at the 1993 SPE Gas Technology Symposium, Calgary, 28-30 June.
5. Guan, L., Mcvay, D. A., Jensen, J. L. and Voneiff, G. W.: "Evaluation of a Statistical infill candidate Selection Technique," Paper SPE 75718 presented at the SPE Gas Technology Symposium held in Calgary, Alberta, Canada, 30 April-2 May 2002.
6. Gao, H., McVay, D. A.: "Gas Infill Well Selection Using Rapid Inversion Methods," Paper SPE 90545 prepared for presentation at the SPE Annual Technical Conference and Exhibition held in Houston, Texas, U.S.A., 26–29 September 2004
7. Al-Hadrami, H. K., Teufel, L. W.: "Influence of Permeability Anisotropy and Reservoir Heterogeneity on Optimization of Infill Drilling in Naturally Fractured Tight-Gas Mesaverde Sandstone Reservoirs, San Juan Basin," Paper SPE 60295 prepared for presentation at the 2000 SPE Rocky Mountain Regional/Low Permeability Reservoirs Symposium held in Denver, CO, 12-15 March 2000
8. Voneiff, G. W., Holditch, S. A.: "A New Approach to Large-Scale Infill Evaluations Applied to the OZONA (Canyon) Gas Sands," Paper SPE 35203 prepared for presentation at the Permian Basin Oil & Gas Recovery Conference held in Midland, Texas, 27-29 March 1996
9. Guppy, K. H., Cinco H. and Ramey, H. J. Jr.: "Transient Flow Behavior of a Vertically Fractured Well Producing at Constant Pressure," Paper SPE 9963.
10. Kelkar, M.2008. *Natural Gas Production Engineering*, Penn Well Corporation, Tulsa, Oklahoma: 216-228
11. Southwest Energy. "2009 Investor presentation". from http://www.swn.com
12. Chesapeake Energy. "2009 Investor presentation". from http://www.chk.com
13. BP America Production Company, 2007, Application for Increased Density. Wyoming O&GCC Hearing Docket No. 239-2007, 12 June 2007
14. Personal Communication with Andrew Stirling, Devon Energy Senior Geologist, on May 21, 2009
15. Kelkar, M. and Perez, G., 2002. Applied Geostatistics for Reservoir Characterization. Society of Petroleum Engineers, Richardson, Texas
16. Hosseini, S. A., Kelkar, M.: "Analytical Upgridding Method to Preserve Dynamic Flow Behavior", paper SPE 116113 presented at the 2008 SPE Annual Technical Conference and Exhibition held in Denver, Colorado, USA, 21-24 September 2008
17. Kelkar and Associates, CONNECT 2.0 program manual
18. Schlumberger. PETREL Reference Manual, 2009
19. Personal Communication with John Graham, Devon Reservoir Engineer on December 16, 2009
20. KAPPA. Ecrin Reference Manual, 2006
21. Schlumberger. ECLIPSE Reference Manual, 2008
22. Lea, J. F., Nickens, H. V., Wells, M. R., 2008. Gas Well Deliquification. Elsevier Inc., Oxford, UK
23. Anderson, D. M., Stotts, G. W. J., Mattar L., Ilk, D., Blasingame, T. A.: "Production Data Analysis – Challenges, Pitfalls, Diagnostics", paper SPE 102048
24. Personal Communication with Justin Lazzari, Devon Energy Operations Engineer, on August 11, 2010

25. Kassenov, B.: "Optimization of Infill Wells in Wamsutter Field, Wyoming," MS Thesis, The University of Tulsa (2010).
26. Personal Communication with Dale Reitz, Devon Energy Geologist, on August 11, 2010
27. Anderson, J. S. 1991. Pressure Mapping as an Aid to Understand Reservoir Drainage. Paper SPE 22962, presented at the SPE Asia-Pacific Conference, Perth, Western Australia, 4-7 November Al-Hussainy, R., Ramey, H.J., Jr. and Crawford, P.B. 1966. The Flow of Real Gases through Porous Media. *J. Pet. Tech*., May: 624-636. Trans. AIME.
28. Kulkarni, K.N., Datta-Gupta, A. and Vasco, D.W. 2001. A Streamline Approach for Integrating Transient Pressure Data into High-Resolution Reservoir Models. *SPEJ* 6 (3): 273-282. SPE 74135-PA.
29. Zhong, H., Harshal, P., Datta-Gupta, A., Jorge, P., Tai, P. 2004. Identifying Reservoir Compartmentalization and Flow Barriers From Primary Production Using Streamline Diffusive Time of Flight. Paper SPE 88802, SPE Reservoir Evaluation & Engineering, June, 238-247.
30. Paulo, S. da C., Roland, N. H., Clayton, V. D. 2004. The Quality Map: A Tool for Reservoir Uncertainty Quantification and Decision Making. Paper SPE 87642, SPE Reservoir Evaluation & Engineering, February, 6-14.
31. Jong, U. K., Datta-Gupta, A., Roald, B., Byron H. 2009. Calibration of High-Resolution Reservoir Models Using Transient Pressure Data. Paper SPE 124834, presented at the SPE Annual Technical Conference and Exhibition, New Orleans, Louisiana, 4-7 October.
32. Gordon, R. and Herman, G. T. 1974. Three Dimensional Reconstruction from Projections: A Review of Algorithms. *Intl. Review of Cytology* 36 (12): 3447-3465.
33. Iyer, H. M. and Hirahara, K. 1993. *Seismic Tomography: Theory and Practice.* Chapman and Hall, New York City.
34. Arridge, S. 1999. Optical tomography in medical imaging. *Inverse Problems* 15 (2): R41-R93.
35. Vasco, D. W. and Finsterle, S. 2004. Numerical Trajectory Calculations for the Efficient Inversion of Transient Flow and Tracer Observations. *Water Resources Research* 40 W01507, DOI:10.1029/2003WR002362
36. Datta-Gupta, A., Yoon, S., Barman, I. and Vasco, D. W. 1998. Streamline-Based Production Data Integration. *JPT* 50 (12): 72-76.
37. Vasco, D. W. and Datta-Gupta, A. 1999. Asymptotic Solutions for solute transport. *Water Resources Research* 35 (1): 1-16.
38. Vasco, D. W. and Datta-Gupta, A. 2001. Asymptotics, Saturation Fronts and High Resolution Reservoir Characterization. *Transport in Porous Media* 42: 315-350.
39. Al-Hussainy, R., Ramey, H. J., Jr. 1966. Application of Real Gas Flow Theory to Well Testing and Deliverability Forecasting. *J. Pet. Tech*., May: 637-642. Trans. AIME.
40. Kravtsov, Y. A. and Orlov, Y. I. 1990. *Geometrical Optics of Inhomogeneous Media.* Springer-Verlag, New York City.
41. Datta-Gupta, A. and King, M. J. 2007. *Streamline Simulation: Theory and Practice.* Textbook Series, SPE, Richardson, Texas.
42. Fatemi, E., Enguist, B. And Osher, S. 1995. Numerical Solution of the High Frequency Asymptotic Expansion of the Scalar Wave Equation. *J. of Computational Physics* 120: 145-155.
43. Hosseini. S. A. and Kelkar, M., 2008. Analytical Upgridding Method to Preserve Dynamic Flow Behavior. Paper SPE 116113, presented at the International Oil & Gas Conference and Exhibition, 21-23 September.
44. Vasco, D. W., Keer, H. and Karasaki, K. 2000. Estimation of Reservoir Properties Using Transient Pressure Data: An Asymptotic Approach. *Water Resources Research* 36 (12): 3447-3465.

APPENDIX A – PROGRAM MANUAL

PURPOSE OF THE PROGRAM

As part of the project, a program was developed using VBA. The program follows the steps given in the report and is used to determine acceleration and incremental potential for infill wells. We will describe each step in this Appendix.

COLLECTION OF DATA

The first two sheets are used for data collection. The first sheet "Basic_Data" will ask the user to input basic data such as API, X and Y coordinates, EUR value, the start date of production and the field corner coordinates. The user will also be asked to input the number of wells in the field, field coordinates and how many sections are included in the N-S and E-W directions. The second sheet, "Production_Data", will ask the user to input monthly production data, along with API and Days on (how many production days in one month).

PROGRAM STRUCTURE

Overview

This VBA program consists of 6 worksheets and 1 field map chart (which can be seen only after plotting the map). When the user starts to use the program, it should be started from the first worksheet "Basic_Data", and the program will advance to the next sheet as the current worksheet is finished.

"Basic_Data" Sheet

In this worksheet, input the basic data that is needed to draw the field map. Please prepare the data mentioned in "Collection of Data" above.

In the "Basic_Data" sheet, you will see three buttons; click on the 'Input Basic Data' button to open an input form as shown in Figure A.1.

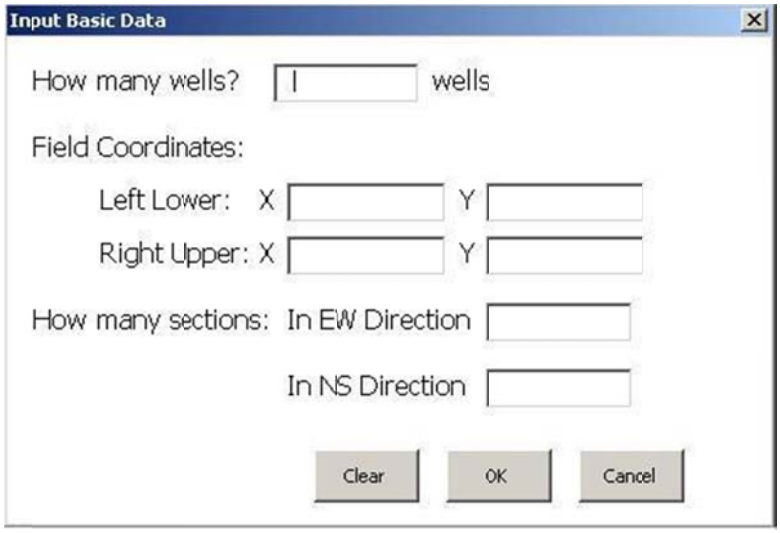

Figure A.1: Basic Data Input

Inputs the number of wells that are in this field, field coordinates (left lower and right upper coordinates), and the number of sections in east-west and north-south directions. You may click "OK" to finish, "Clear" to clear all data, or "Cancel".

Next, you will be asked to input well data. Copy the well data you want to analyze (this data should be prepared in advance) and paste into this sheet accordingly (Figure A.2).

No.	API	X	Y	EUR	Start Date
1	49007050770001	230358.2388	76266.50736	0.933	4/1/2007
2	49007069520000	228010.3034	77894.32224	1.925	1/1/1980
3	49007200320001	229930.2996	79497.29592	2.872	1/1/1980
4	49007201250000	229533.8767	79094.35032	2.266	1/1/1980
5	49007216770000	228056.2368	75816.77496	0.256	7/1/1998
6	49007216760000	229951.727	77493.876	0.408	5/1/1998
7	49007216850000	230241.1346	81324.35856	1.092	8/1/1998
8	49007223830000	228329.7338	77194.62336	0.744	9/1/2003
9	49007217380000	227364.3103	81130.78008	0.807	9/1/1982
10	49007203250001	229155.1627	77485.40256	0.808	1/1/1980
11	49007212840000	228453.9398	77641.30776	1.764	8/1/1993
12	49007220870000	228859.6286	80752.12704	2.525	9/1/2002
13	49007220640000	229076.2805	79483.79328	2.922	9/1/2002
14	49007222380000	230549.6532	76987.17648	2.32	12/1/2002

Input Basic Data

Clear Data

Finish Input

Figure A.2: Well Data Input

You will see the well and field data on this sheet (Figure A.2). Check this data again; if it is correct, click the "Finish Input" button to proceed to the next sheet. If the information is not correct, you may change it in the table.

"Production_Data" Sheet

After you finish inputting basic data in the first sheet (Figure A.2), and select "Finish Input" the program will take you to the "Production_Data" sheet (Figure A.3). You will see three buttons on this sheet (not shown in figure). Click "Input Production Data" and a message box will appear asking you to input API,

production data (Gas) and Days on. Copy production data (prepared in advance by user) as shown in Figure A.3

API	Gas	Days on
49007212870000	1657	7
49007212870000	5269	20
49007212870000	4610	21
49007212870000	5050	20
49007212870000	5625	31
49007212870000	6985	30
49007212870000	8008	31
49007212870000	6059	26
49007212870000	7910	31
49007212870000	6135	22
49007212870000	7411	30

Figure A.3: Production Data Input

Click "Finish Input" and the program will automatically generate the well number in the first column and month data in the third column for production data as shown in Figure A.4. The production data input here should be consistent with the well's input in "Input Basic Data". The program uses the API number to identify the wells. If there are significant production data, the program will take some time to finish processing the data.

No.	API	Month	Gas	Days on
34	49007212870000	1	1657	7
34	49007212870000	2	5269	20
34	49007212870000	3	4610	21
34	49007212870000	4	5050	20
34	49007212870000	5	5625	31
34	49007212870000	6	6985	30
34	49007212870000	7	8008	31
34	49007212870000	8	6059	26
34	49007212870000	9	7910	31
34	49007212870000	10	6135	22
34	49007212870000	11	7411	30
34	49007212870000	12	4875	31
34	49007212870000	13	4696	30
34	49007212870000	14	5302	31

Figure A.4: Production Data Sheet

“Section” Sheet

Now that you have finished inputting the data, you are ready to start the analysis. You should be in the “Section” sheet (if you’re not, go back to the “Production_Data” sheet (Figure A.3) and work back to this step). In this sheet, you will initially see two buttons; a third button, “Analyze Sections”, will appear after the field map is generated. Click “Generate Field Map and Edit Sections” to generate the field map and section information. You should find the field map (Figure A.6) and all the section information in this sheet (Figure A.5).

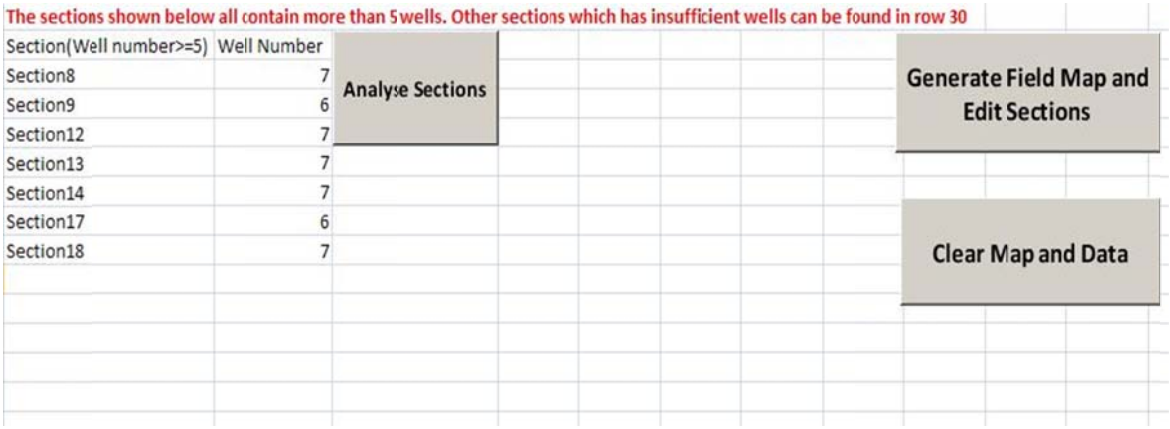

Figure A.5: Section Analysis

The field map (Figure A.6) is a 3D bubble chart with EUR labels on the bubbles. This map is divided into certain sections in both the E-W and the N-S directions based on the section number that was input in the first sheet (Figure A.2). In the Figure A.5, you will see all of the sections and how many wells are contained in each section. By default, only sections that contain more than 5 wells are recommended for analysis. Other sections that have less than 5 wells are also shown in the “Section” screen but are not shown in this figure (Figure A.5). Click “Analyze Sections” to proceed.

You will now see the “Field_Map” sheet and a “Please Select the Section” form will pop-up (Figure A.6).

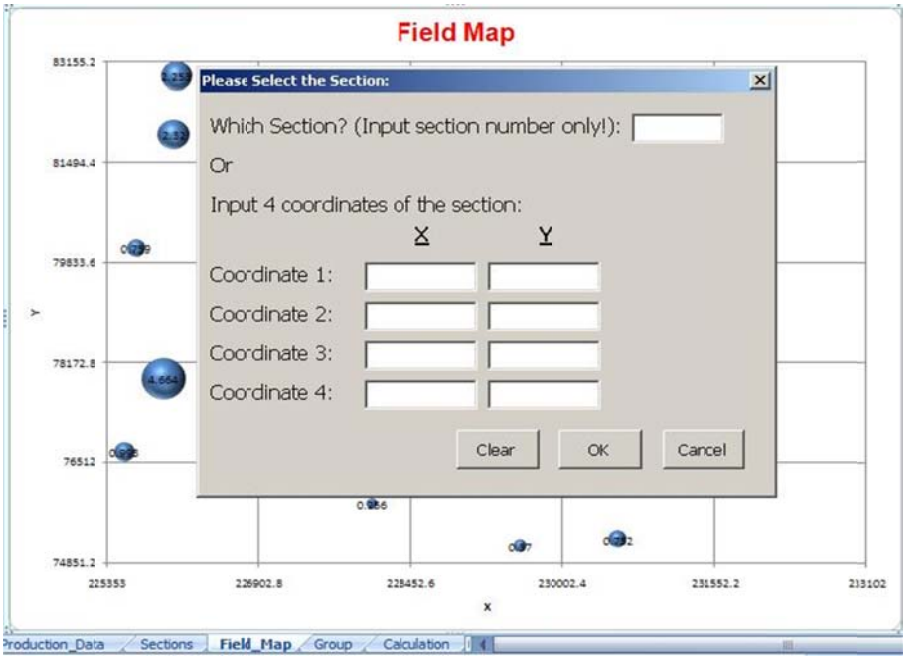

Figure A.6: Field Map and Section Selection

In this form, you can select a single section by inputting a section number in the first box or multiple sections by inputting section coordinates. For example, select section 13 which contains 7 wells. The upper left corner section is section 1, and the section numbers increase as you move to the right. For example, if we have 5 sections in both E-W and N-S directions, the last section in the first row is section 5 and first section in second row is section 6 and so forth. After you input the section number, click "OK" and a "Group Wells" input box will pop up. Input the acreage of the selected section. A red boundary section, which can help the user to locate the area, will appear in the field map and all the wells in that section will show up in a table. This is shown in Figure A.7.

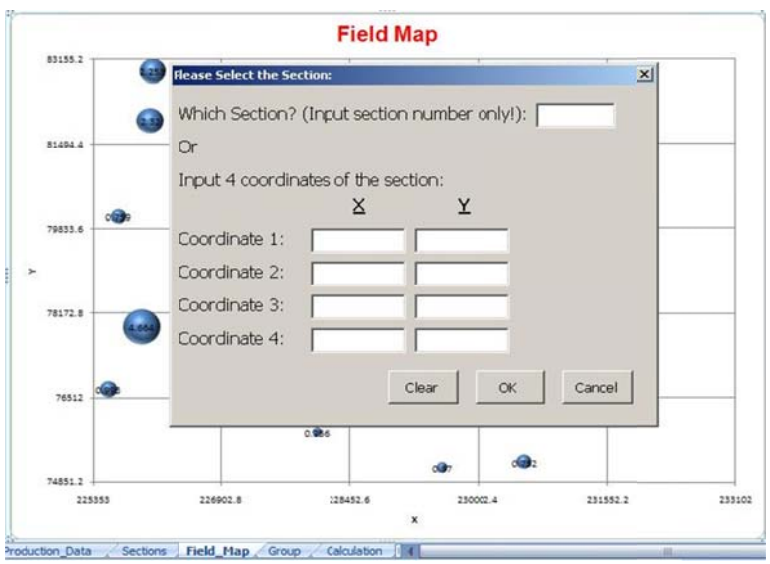

Figure A.7: Selected Section and Wells in the Section

As shown in the graph, in section 13 there are 7 wells. You can verify the well information in the table by comparing it with the map.

You can select multiple sections as long as they have four common corners for the entire area selected. Note that only parallelograms can be selected. When you input 4 coordinates, you must make sure to input the upper-most corner. You will also be asked to input the acreage of the selected area (Figure A.8).

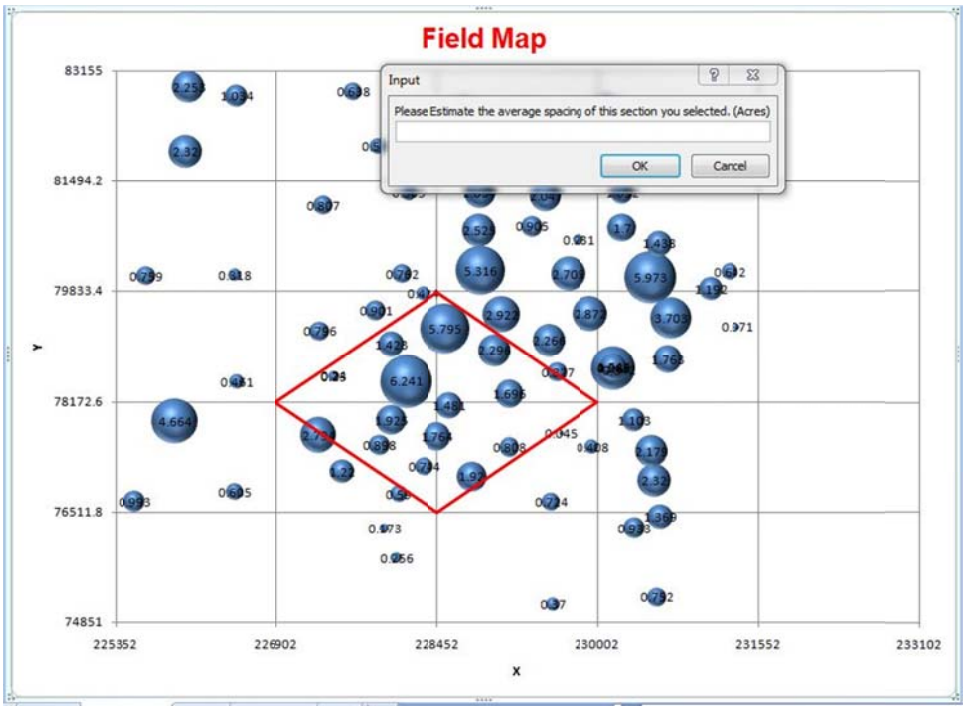

Figure A.8: Multiple Sections Selection

All wells in the selected area will be shown in a table. Click "OK" in the "Group Wells" table (Figure A.7), and the program will go to the "Group" sheet.

"Group" Sheet

In this sheet, the program automatically groups the wells in the area selected. Grouping is very important in this method, so you must look at the group result carefully. You may also regroup the wells if the recommended grouping is not reasonable (Figure A.9).

Recommendation of well groups:			3	groups			
	Well no.	Start Date	API	X	Y	EUR	
Group 1:	2	01/01/1980	490070695	228010.3	77894.32	1.925	Use recommendation
	10	01/01/1980	490072032	229155.2	77485.4	0.808	
	50	01/01/1980	490072019	229156.7	78289.56	1.696	
	41	02/01/1984	490072089	228157.3	78476.73	6.241	Regroup the wells
Group 2:	38	01/01/1991	490072114	228530.6	79269.21	5.795	
	11	08/01/1993	490072128	228453.9	77641.31	1.764	
	30	10/01/1993	490072129	227465.4	78558.39	0.24	
	29	01/01/1994	490072129	227464.7	78549.52	0.23	
Group 3:	15	10/01/2002	490072222	228795	77044.02	1.92	
	8	09/01/2003	490072238	228329.7	77194.62	0.744	
	58	02/01/2004	490072244	229005.9	78944.36	2.296	
	57	03/01/2004	490072244	228571.2	78113.44	1.481	
	59	04/01/2004	490072244	228010.1	79038.33	1.423	
	62	02/01/2005	490072251	227895.5	77512.16	0.898	

Figure A.9: Grouping Recommendation

Inspect the start date of production and decide if you want to use the recommended group or regroup this section. If the recommended grouping is satisfactory, click "Use recommendation" to go to the "Calculation" sheet. If the recommended grouping is not satisfactory, you can regroup by clicking "Regroup the wells", and an "Input" box will pop up (Figure A.10).

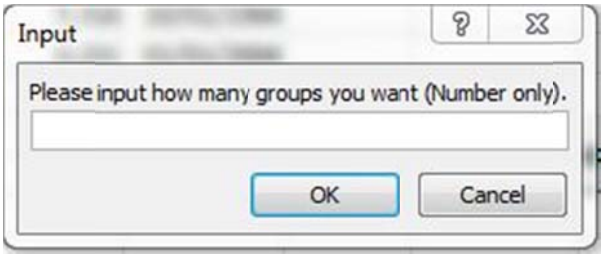

Figure A.10: Regroup Number

Input the number of groups and click "OK" to see the regrouping form (Figure A.11).

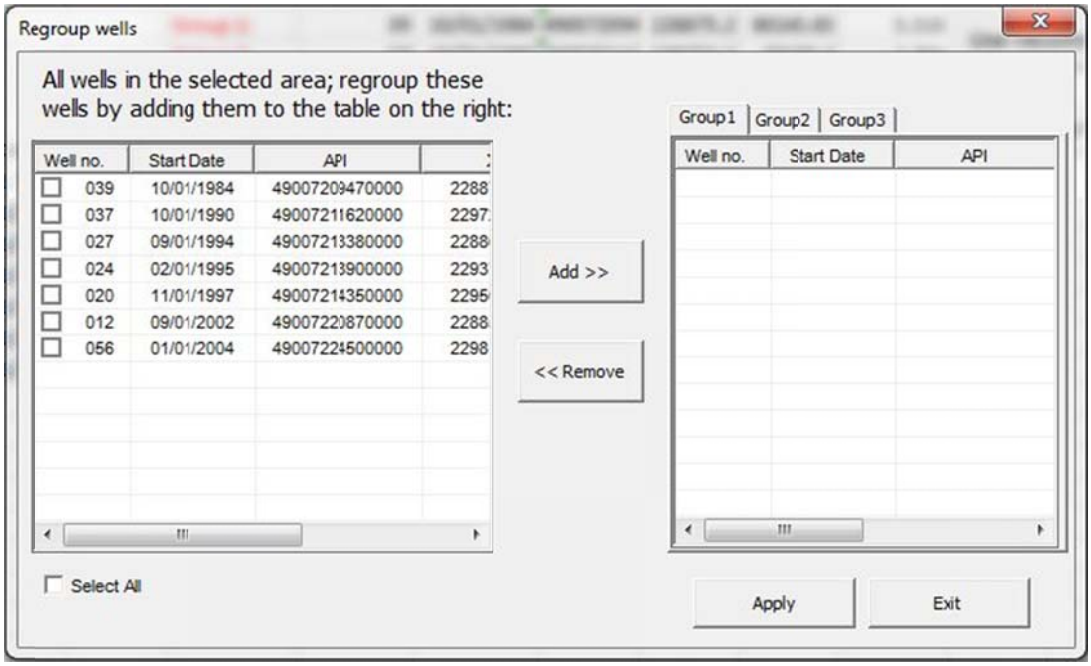

Figure A.11: Regrouping Form

The "Regroup wells" form has two parts. On the left is the well information for this section, which includes well number, start date, API, X and Y coordinates and EUR. On the right are multiple panels depending on the number of groups. The maximum number of groups is set to 10, so if you input more than 10 groups, the program will disregard any input after Group10. In this example, we have 3 groups. You can select a group by clicking on the tab. Note that there are 2 buttons, "Add" and "Remove". First, select the wells in the left table by clicking the check boxes next to each well, then click the "Add" button to include those selected wells in Group1. You may then add wells to your other groups. You may also remove wells by clicking the "Remove" button. Figure A.12 is an example of a completed regrouping of wells.

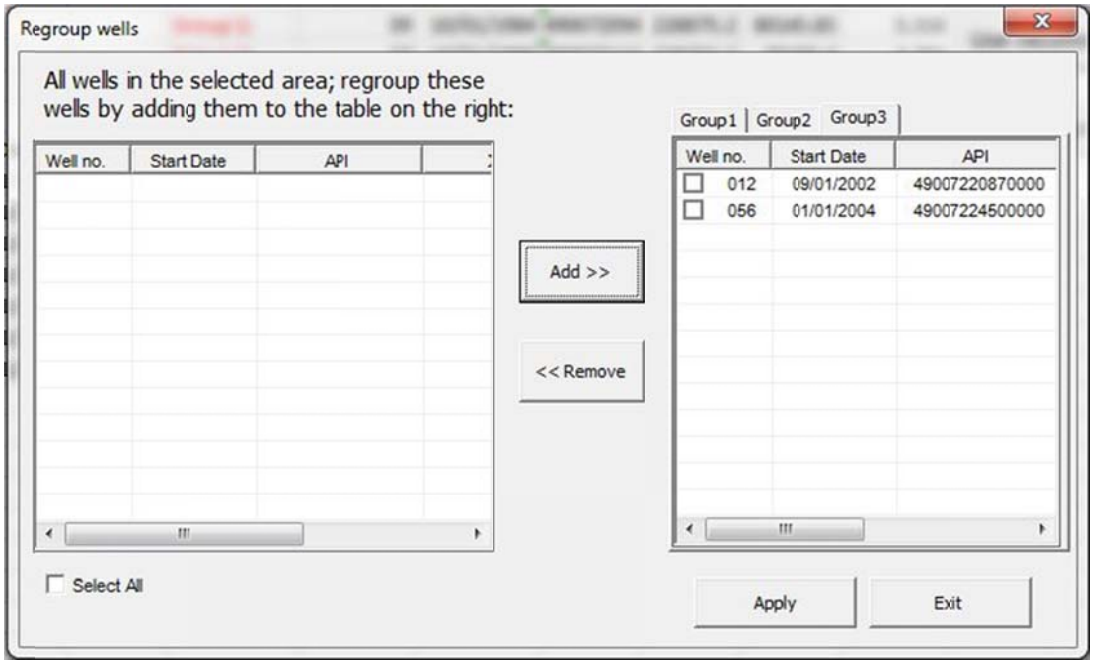

Figure A.12: Regrouping Result in Form

When satisfied with the well grouping, click "Apply" to output the regroup results to the "Group" sheet (Figure A.13).

Regroup results:		3	groups				Use Regroup Result
	Well no.	Start Date	API	X	Y	EUR	
Group 1:	2	1/1/1980	49007069520000	228010.3	77894.322	1.925	
	10	1/1/1980	49007203250001	229155.2	77485.403	0.808	
	50	1/1/1980	49007201940000	229156.7	78289.556	1.696	
	41	2/1/1984	49007208940000	228157.3	78476.734	6.241	
Group 2:	38	1/1/1991	49007211470000	228530.6	79269.214	5.795	
	11	8/1/1993	49007212840000	228453.9	77641.308	1.764	
	30	10/1/1993	49007212940000	227465.4	78558.39	0.24	
	29	1/1/1994	49007212950000	227464.7	78549.52	0.23	
Group 3:	15	10/1/2002	49007222240000	228795	77044.022	1.92	
	8	9/1/2003	49007223830000	228329.7	77194.623	0.744	
	58	2/1/2004	49007224450000	229005.9	78944.358	2.296	
	57	3/1/2004	49007224470000	228571.2	78113.443	1.481	
	59	4/1/2004	49007224460000	228010.1	79038.328	1.423	
	62	2/1/2005	49007225190000	227895.5	77512.164	0.898	

Figure A.13: Regrouping Result in Sheet

Click "Use Regroup Result" and the program will go to the "Calculation" sheet.

"Calculation" Sheet

In this sheet, the wells are divided into groups, recommended group or regroup results depending on your "Group Sheet" selections. The program will calculate the start date for every group in column H. The group start date is the average start date of all wells in the group.

A	B	C	D	E	F	G	H	I	J
Wells in groups:									
	Well no.	Start Date	API	X	Y	EUR	Start Date of groups		
Group 1:	48	11/01/1976	49007202220	229705.1	82251.59	1.781	12/07/1979	Plot and Extrapolation	
	2	01/01/1980	49007069520	228010.3	77894.32	1.925			
	3	01/01/1980	49007200320	229930.3	79497.3	2.872			
	4	01/01/1980	49007201250	229533.9	79094.35	2.266			
	10	01/01/1980	49007203250	229155.2	77485.4	0.808			
	19	01/01/1980	49007202310	227542.2	77123.12	1.22			
	45	01/01/1980	49007203890	229570.3	75119.67	0.37			
	47	01/01/1980	49007202280	229549.6	76666.59	0.724			
	49	01/01/1980	49007201960	230352.4	77896.91	1.103			
	50	01/01/1980	49007201940	229156.7	78289.56	1.696			

Figure A.14: Group Start Date

Click "Plot and Extrapolation" to plot cumulative production versus a certain function of time, using either linear or bilinear production. If the flow is linear, use cumulative production versus $t^{1/2}$; if it is bilinear, use cumulative production versus $t^{3/4}$. The criterion for choosing the appropriate function of time is to decide which function can give us a better linear relationship. When you click "Plot and Extrapolation", an input box will appear. Input the time for EUR estimation (Figure A.15). The time may be changed later. After inputting the time, a "Plot and Extrapolate" form will pop up. Select the well that needs to be plotted (Figure A.16).

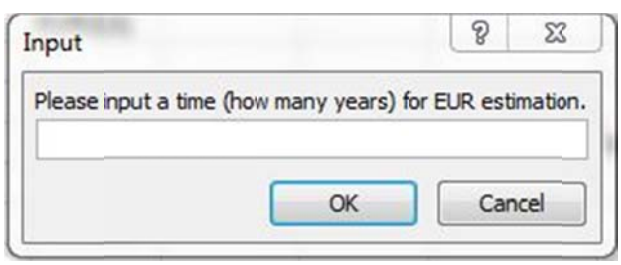

Figure A.15: Input Time for EUR Estimation

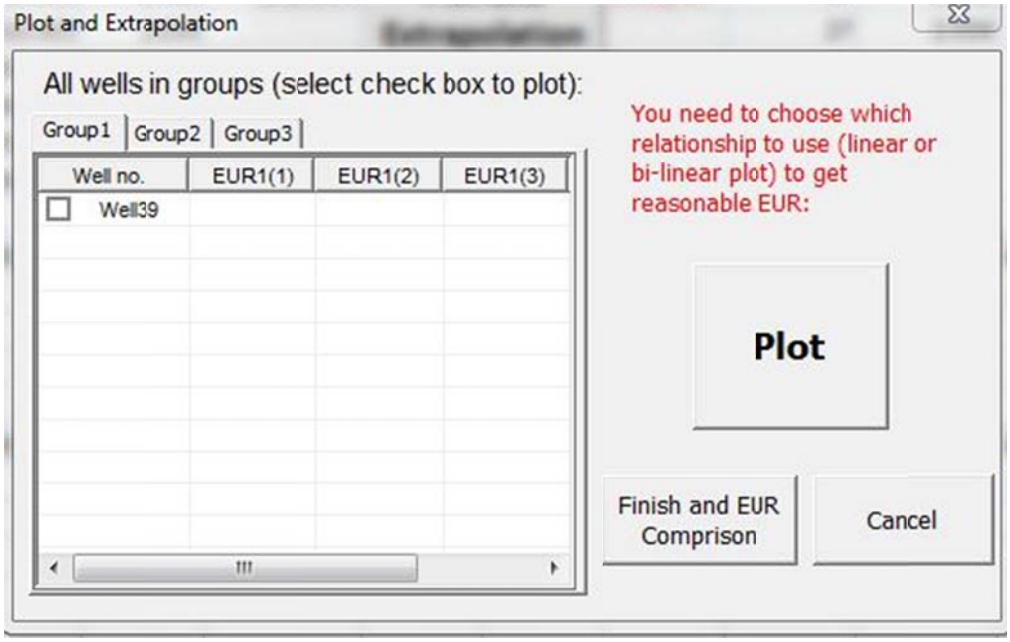

Figure A.16: Plot User Form

In the "Plot and Extrapolation" form, the wells are listed for each group. Check one well and click the "Plot" button to generate a cumulative production versus function of time plot. Note that the program only plots one well at one time, so if you check more than one well, the program will only plot the last well selected. Do not click "Finish and EUR Comparison" until all wells have been plotted. The program will show a warning if there are wells that still need to be plotted. After you select a well and click "Plot", the program will display the "Plot" sheet where you can see the production data of the well and plots of linear and bilinear flow (Figure A.17).

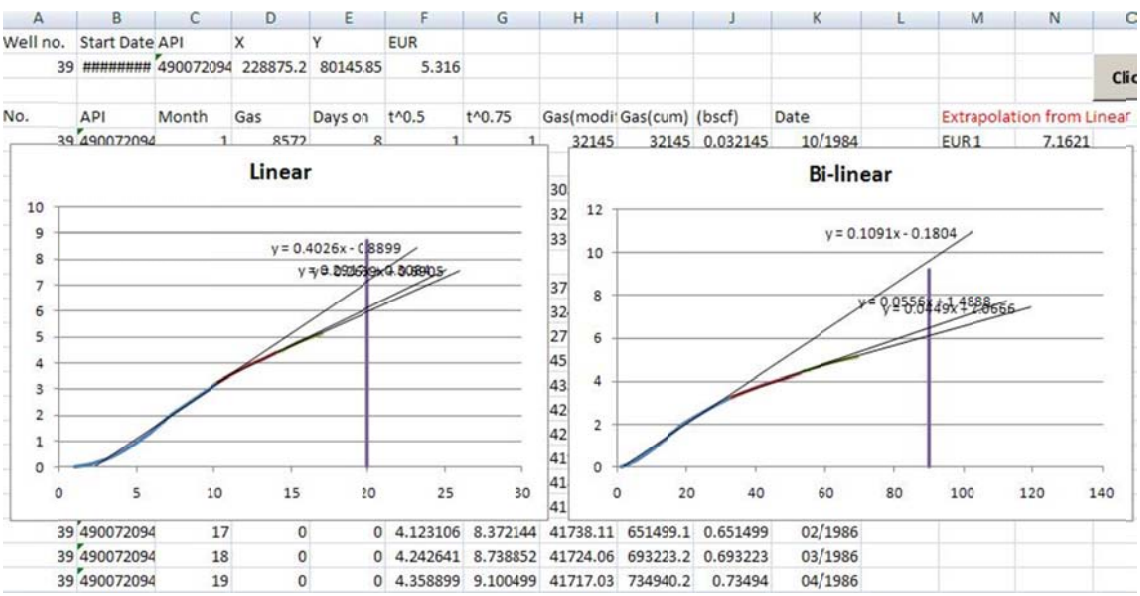

Figure A.17: Linear and Bilinear Plots

You should now decide which plot has a better linear trend and which extrapolated EUR is closer to the reported EUR. In this example, we should choose a linear plot. On the right side of the sheet, there is a

"Click to Choose" button. The calculated EUR is shown below the button for both the linear and bilinear case. If you select "Click to Choose", the program will bring up a table containing the EUR data of linear and bilinear plots (Figure A.18). The linear and bilinear cases are shown. Furthermore, the reported EUR at the top of this table can be compared with the estimated EUR. You decide which EUR to select.

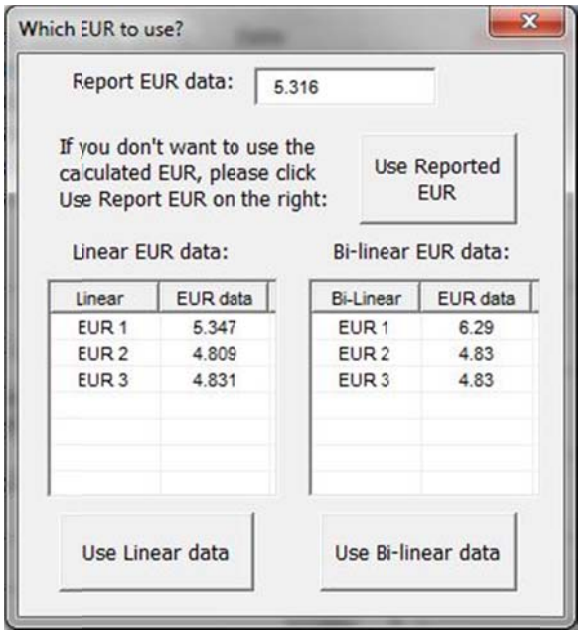

Figure A.18: EUR Data

In this case, you should select "Use Linear Data". The program will go back to the "Plot and Extrapolation" form and ask you to plot other wells. In the "Which EUR to use?" form the user can also compare with the reported EUR. If you do not want to use the extrapolated EUR, you must use the reported EUR by selecting "Use Reported EUR". The user must plot every individual well. When all wells are plotted, click on "Finish and EUR Comparison" (Figure A.16) and the program will go back to the "Calculation" sheet (A.14?).

Now you are able to see the comparison of the reported EUR and estimated EUR to check the validity of the estimation (Figure A.19). Here, you can compare these EURs in the plot and compare the average of EUR. If the discrepancy is too large, you can click on "Pick Another Time for EUR Estimation" to choose another time. It will then calculate the new EUR automatically without going through the linear and bilinear selection process.

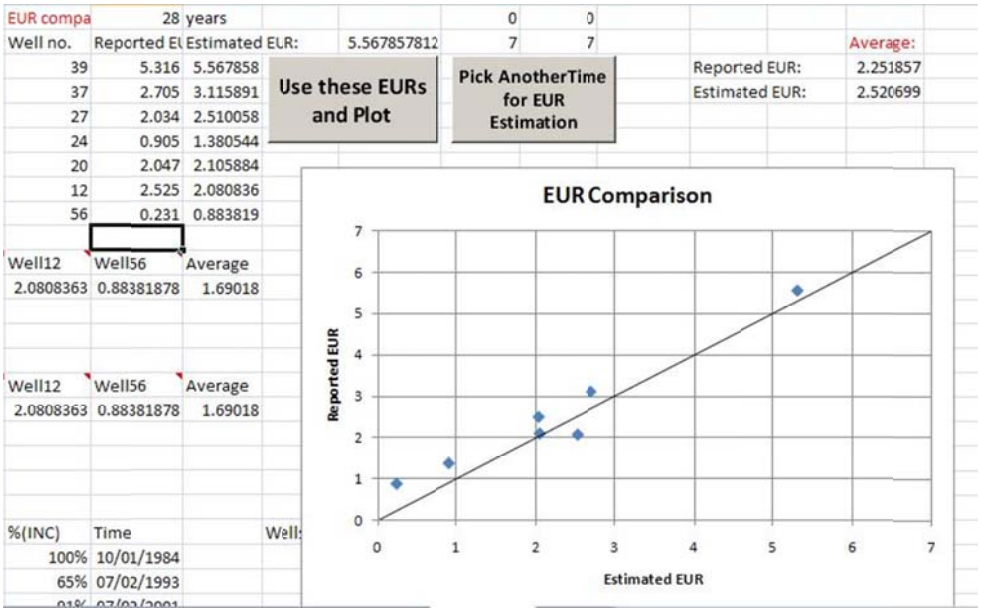

Figure A.19: EUR Comparison

If the EUR is reasonable, you can click on "Use these EURs and Plot" to proceed. The program will automatically calculate the acceleration and incremental production based on the extrapolation results and output in the "Calculation" sheet. You will see two plots: acceleration percentage, incremental percentage and total production as a function of time and spacing (Figure A.20). This plot allows you to observe the trends of the incremental and acceleration production as infill wells are drilled. Click the "Extrapolation" button below the plots to extrapolate the plot at the expected spacing.

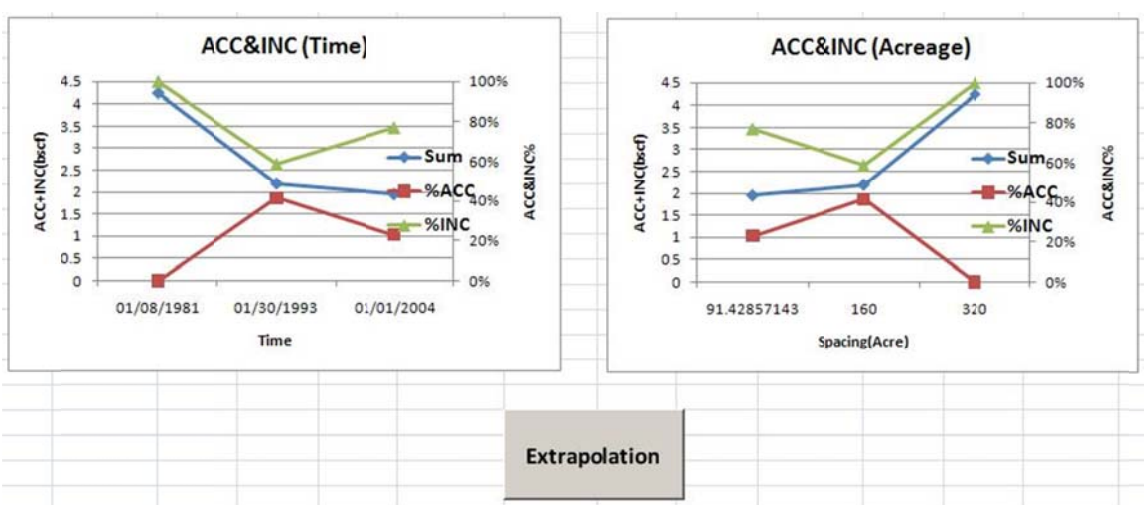

Figure A.20: Acceleration and Incremental Plot

An "Input" box will pop up and you will input the spacing that you want to extrapolate. It will also show the current spacing (Figure A.21).

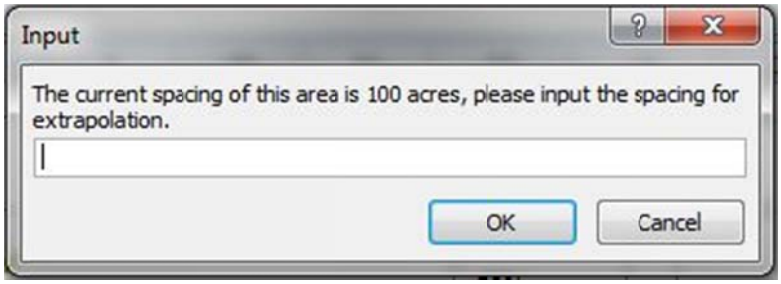

Figure A.21: Spacing Acreage Input

The result of the extrapolation based on certain spacing will output in the Extrapolation Plot sheet as well as in the extrapolation plot. The result includes the acceleration production and incremental production at expected spacing, which are highlighted in red cells. Figure A.22 is extrapolated to 60-acre spacing.

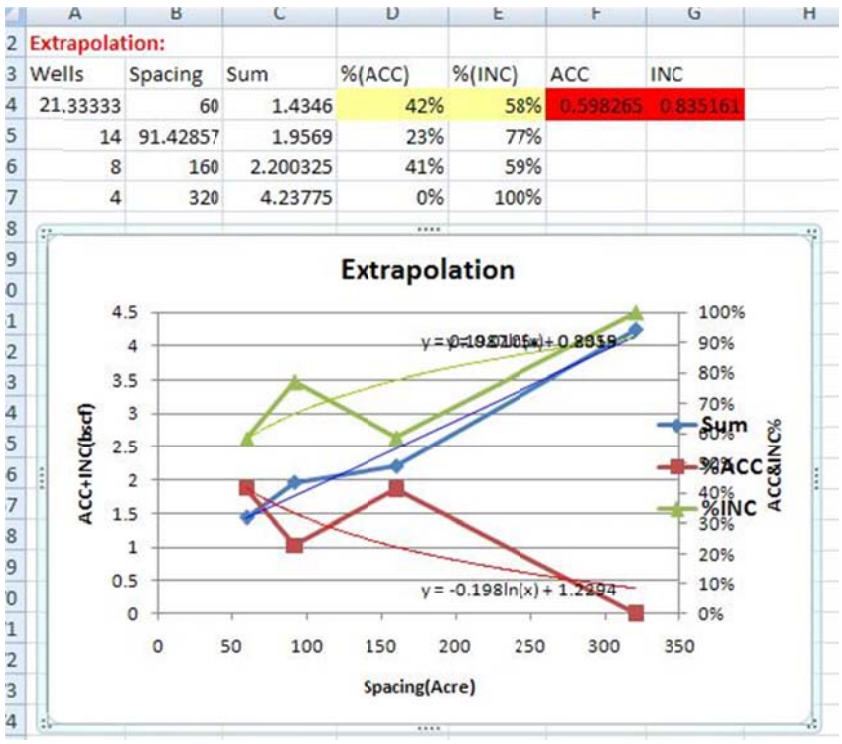

Extrapolation:						
Wells	Spacing	Sum	%(ACC)	%(INC)	ACC	INC
21.33333	60	1.4346	42%	58%	0.598265	0.835161
14	91.42857	1.9569	23%	77%		
8	160	2.200325	41%	59%		
4	320	4.23775	0%	100%		

Figure A.22: Extrapolation Plot

Once the analysis is finished for a selected area, go back to the "Section" sheet and select another section and repeat the procedure to calculate the infill potential for different sections. By comparing the results of infill potential in different sections, you should find which section has the best potential for infill drilling.